

Search for supersymmetry in diphoton final states
with the CMS detector

Matthew Lawrence Joyce

September 22, 2021

CONTENTS

1.	<i>The Standard Model of Particle Physics</i>	14
1.1	The Standard Model	14
1.2	Electroweak Symmetry Breaking	16
1.3	Problems with the SM	26
2.	<i>Supersymmetry</i>	27
3.	<i>The Large Hadron Collider</i>	28
3.1	Introduction	28
3.2	Injection Complex	28
3.3	Tunnel and Magnets	29
3.4	Luminosity	30
4.	<i>Compact Muon Solenoid</i>	36
4.1	Introduction	36
4.2	Coordinate System	38
4.3	Tracker	39
4.3.1	Pixel Detector	40
4.3.2	Strip Detector	42
4.4	Electromagnetic Calorimeter	43

4.4.1	Crystals	43
4.4.2	Barrel and Endcaps	45
4.4.3	Preshower layer	46
4.4.4	Performance	46
4.5	Hadronic Calorimeter	47
4.6	Superconducting Solenoid	49
4.7	Muon System	51
5.	<i>CMS Trigger System</i>	54
5.1	L1 trigger	54
5.1.1	Calorimeter trigger	55
5.1.2	Muon trigger	56
5.1.3	Global Trigger	56
5.2	High Level Trigger	57
5.3	Trigger efficiency	58
6.	<i>CMS Particle and Event Reconstruction</i>	59
6.1	Tracks	59
6.2	Calorimeter clusters	60
6.3	Object identification	61
6.3.1	Muons	61
6.3.2	Electrons	62
6.3.3	Photons	63
6.3.4	Jets	65
6.4	Missing transverse momentum	67
6.5	Pileup mitigation	68

7.	<i>Data Analysis</i>	73
7.1	Overview	73
7.2	Data	74
7.3	Monte Carlo samples	75
7.4	Object definitions	75
7.4.1	Photons	76
7.4.2	Electrons	78
7.4.3	Muons	79
7.4.4	Jets	81
7.5	Event selection	81
7.6	Backgrounds	82
7.6.1	Instrumental background	83
7.6.2	Electroweak background	94
7.6.3	Irreducible background	95
7.7	Signal and control regions	96
8.	<i>Results and Interpretations</i>	112
8.1	Observation vs Predicted	112
8.2	Simplified models	112
8.3	Statistical analysis	113
8.4	Limits for T5gg and T6gg	116
9.	<i>Future Improvements: MIP Timing Detector (MTD)</i>	119
9.1	Introduction	119
9.2	Barrel Timing Layer	121
9.2.1	LYSO:Ce crystals	126

9.2.2	SiPMs	131
9.2.3	Glue qualification	131
9.2.4	Performance at test beam	135

LIST OF FIGURES

1.1	Illustration of the Higgs potential for $\mu^2 < 0$	22
1.2	Summary of content of the SM.	25
3.1	LHC interaction points	32
3.2	Layout of LHC accelerator complex [24].	33
3.3	Proton bunch capture onto RF bucket [9].	34
3.4	Cross section of LHC dipole [14]	34
3.5	Integrated luminosity delivered by the LHC to the CMS experiment each year from 2010-2018.	35
4.1	Schematic of CMS detector [36]	37
4.2	Transverse slice of the CMS detector[10]	38
4.3	Cross section (side) of CMS tracker prior to the Phase 1 upgrade during the year-end technical stop of 2016/2017. Each line represents a detector module while double lines indicate back-to-back strip modules. Surrounding the pixel tracker (PIXEL) is the strip detector, which is divided into the Tracker Inner Barrel (TIB), Tracker Outer Barrel (TOB), Tracker Inner Disks (TID), and Tracker Endcaps (TEC). Reprinted from Reference [19].	40

4.4	Cross section (side) of pixel detector. The lower half , labeled "Current", shows the design prior to 2017 while the upper half, labeled "Upgrade", shows the design after the upgrade. Reprinted from Resource [18]	41
4.5	PbWO ₄ crystals. Left: EB crystal with APD. Right: EE crystal with VPT. Reprinted from [20]	44
4.6	Schematic of ECAL. Reprint from [20]	47
4.7	Longitudinal view of HCAL [2]	49
4.8	Longitudinal slice of CMS detector while operating at 3.8-T central magnetic field. The right-hand side of the figure shows a mapping of the magnetic field lines while the left-hand side shows a mapping of the field strength. Reprint from [16]	50
4.9	Cross-section of one quadrant of the CMS detector. The DTs are labeled as "MB" (Muon Barrel) and the CSCs are labelled as "ME" (Muon Endcap). The RPCs are "RB" for those in the barrel and "RE" for those in the endcap. Reprint from [39].	52
5.1	L1 trigger system. Reprint from [3]	55
6.1	The Bremsstrahlung photons continue along a straight trajectory while the electron path is bent by the magnetic field. This results in energy deposited in the calorimeter for such electrons to be spread out along the ϕ -direction.	63

6.2	Comparison of the k_T , Cambridge/Aachen, and anti- k_T jet clustering algorithms with the distance parameter set to $R = 1$. This is a sample parton-level event upon which each algorithm was applied. Of the three, the anti- k_T algorithm gives the most regularly shaped jets. Reprint from [12]	70
6.3	Pileup distribution for 2016.	71
6.4	Pileup distribution for 2017	71
6.5	Pileup distribution for 2018	72
7.1	Two examples of GGM supersymmetry breaking processes resulting in final states containing two photons and missing transverse momentum. The T5gg model (left) shows gluinos produced from $p - p$ collisions which subsequently result in two neutralinos, each decaying to a photon and a gravitino. The T6gg model (right) shows squarks produced from $p - p$ collisions following a similar decay chain.	73
7.2	Scale factors for 2016 loose photon ID.	78
7.3	Scale factors for 2017 loose photon ID.	79
7.4	Scale factors for 2018 loose photon ID.	80
7.5	Mismeasurement of Jet3 results in an imbalance in the events transverse momentum.	83
7.6	Summary of the steps for the Rebalance and Smear method. .	85
7.7	Jet energy response for leading jets in QCD MC before and after rebalancing.	86

7.8	Leading photon p_T distributions for di-photon QCD MC events before and after Rebalance and Smear implementation.	87
7.9	Next-to-leading photon p_T distributions for di-photon QCD MC events before and after Rebalance and Smear implementation.	88
7.10	Schematic view of a decision tree.	90
7.11	The 95% confidence level upper limits on the pair production cross sections for gluinos (7.11a) and squarks (7.11b) as a function of gluino/squark and neutralino masses as reported in [38]. The shaded vertical bands show the mass bands used in the BDT training.	97
7.12	BDT input variables 1	98
7.13	BDT input variables 2	99
7.14	BDT input variables 3	100
7.15	Overtraining check for background samples in Phase 0 BDT.	101
7.16	Overtraining check for signal samples in Phase 0 BDT.	102
7.17	Overtraining check for background samples in Phase 1 BDT.	103
7.18	Overtraining check for signal samples in Phase 1 BDT.	104
7.19	Phase 0 BDT response for signal and background	105
7.20	Phase 1 BDT response for signal and background	106
7.21	BDT cut values on T5gg models resulting in 90% signal acceptance.	107
7.22	BDT cut values on T6gg models resulting in 90% signal acceptance.	108

7.23 BDT response to Rebalance and Smear events in 2016 GJets MC	109
7.24 BDT response to Rebalance and Smear events in 2017 GJets MC	109
7.25 BDT response to Rebalance and Smear events in 2018 GJets MC	110
7.26 Comparison of ZGGToLLGG MC to data	111
8.1 Theoretical cross section gluino pair production as a function of gluino mass	113
8.2 Theoretical cross section for squark pair production as a func- tion of squark mass	114
8.3 Cross section limits for T5gg simplified model.	117
8.4 Cross section upper limits for T6gg simplified model.	118
9.1 Timeline for LHC	120
9.2 Vertices from a simulated 200 pileup event with MTD timing resolution of \sim 30 ps. The red dots represent the simulated vertices while the yellow lines indicate vertices reconstructed without the use of timing information. The black crosses and blue open circles represent tracks and vertices reconstructed using time information from the MTD. Reprint from	121
9.3 Schematic view of MTD	122
9.4 LYSO:Ce crystal slant thickness in the BTL.	125
9.5 Overview of the BTL	126
9.6 Readout unit for the BTL.	127

9.7	Evolution of time resolution for the BTL.	128
9.8	Transmission curve for LYSO:Ce before and after being irradiated to a fluence of $2 \times 10^{13} \text{ cm}^{-2}$ with 24 GeV protons. . .	129
9.9	Time resolution measurements of LYSO:Ce before and after irradiation.	130
9.10	Energy spectrum for Cs ¹³⁷	132
9.11	Left: This is a teflon mold used to produce glue samples. Right: The glue samples after being removed from the mold. These samples were then placed in the irradiator for radiation exposure.	133
9.12	Preliminary radiation tolerance studies of the top five glue candidates show that only NOA-61 and RTV-3145 are viable. Epotek, Polytec, and BC-600 all show substantial optical degradation after just a fraction of 50 kGy target. . . .	136
9.13	Figure 9.13a shows an example a glue sample ready for transmission measurements. Figure 9.13b shows how the measurement is taken with the sample placed inside the photoparameter.	137
9.14	Transmission curves for both NOA-61 (Figure 9.14a and RTV-3145 (Figure 9.14b). Figure 9.14c shows the transmission at 420 nm, the peak of the LYSO:Ce emission spectrum, with increasing ionizing doses. While NOA-61 starts with a higher transmission, RTV-3145 is more radiation tolerant and has a higher transmission after the full ionizing dose.	138

LIST OF TABLES

1.1	Boson fields in the SM	16
1.2	Fermions in the SM. The first two numbers listed in the third column give the supermultiplet representation under $SU(3)_C$ and $SU(2)_L$ respectively. A 1 means that it is not charged under that group and therefore will not couple to the associated force. A 3 as the first number means that it has color charge and couples to the strong force. A 2 for the second number means that it has weak isospin and couples to the weak force. The third number gives the value of the weak isospin. Adjoint representation is specified by the presence of a bar over the number.	17
4.1	Summary of signals expected for each particle type in each sub-detector.	37
5.1	Primary HLT	57
7.1	Data Samples	74
7.2	Table of MC samples used.	75
7.3	Summary of loose ID photons cuts	77
7.4	List of MC samples used for training and testing BDT	92

7.5	Summary of $Z\gamma\gamma \rightarrow \nu\nu\gamma\gamma$ model validation	96
9.1	Predicted radiation doses and fluences at different location of the BTL after an integrated luminosity of 3000 fb^{-1} . The two far right columns include a safety margin of 1.5.	123
9.2	Summary of crystal and slant thicknesses in different η regions.	124

¹ 1. THE STANDARD MODEL OF PARTICLE PHYSICS

² 1.1 *The Standard Model*

The Standard Model (SM) of particle physics is a Lorentz-invariant quantum field theory (QFT) that describes the dynamics of elementary particles. Three critical developments leading to the formation of the SM, as described by Steven Weinberg[41], were the quark model proposed by Gell-Mann[26] and Zweig[44] in 1964, the idea of gauge symmetry by Yang and Mills[43] in 1954, and the notion of spontaneous symmetry breaking proposed by Goldstone[28] in 1961. This ultimately led to the SM in its current form as a non-Abelian gauge theory with the symmetry group

$$G_{SM} = SU(3)_C \otimes SU(2)_L \otimes U(1)_Y \quad (1.1)$$

³ where $SU(3)_C$ is responsible for strong interactions and $SU(2)_L \otimes U(1)_Y$ is
⁴ responsible for unified electromagnetic and weak interactions, also known as
⁵ electroweak interactions.

⁶ Associated with each of these symmetry groups is a set of massless spin-1
⁷ vector fields called gauge bosons. These are listed in Table 1.1 along with the
⁸ associated charge or generator for that group. There are eight such gauge
⁹ bosons in $SU(3)_C$ called gluons $G_\mu^{1,\dots,8}$. There are three gauge bosons $W_\mu^{1,2,3}$

in $SU(2)_L$ and one gauge boson B_μ in $U(1)_Y$. The gauge bosons mediate the interactions between spin-1/2 fields ψ called fermions. At this point it's worth noting that the W and B gauge fields are not observable bosons, but are mixed by electroweak symmetry breaking to produce observable bosons. The details of this will be covered in Section 1.2.

There are twelve fermion fields which can be split into six lepton fields and six quark fields. Both quarks and leptons are comprised of three generations. For quarks there are three "up-type" quarks (up u , charm c , and top t) and three "down-type" quarks (down d , strange s , and bottom b). The lepton fields are electron e , muon μ , tau τ , and three neutrino fields ν_e , ν_μ , and ν_τ . The fermion fields and their representations under G_{SM} are listed in Table 1.2. Each fermion field can be expressed in terms of left and right chirality fields, which are represented by a doublets ψ_L in the left-handed case and singlets ψ_R in the right-handed case with

$$\psi = \psi_R + \psi_L \quad (1.2)$$

$$\psi_R = \frac{1}{2}(1 + \gamma^5)\psi \quad (1.3)$$

$$\psi_L = \frac{1}{2}(1 - \gamma^5)\psi \quad (1.4)$$

The SM also contains a complex scalar doublet field ϕ called the Higgs field in honor of Peter Higgs, who was among one of the physicists who proposed its existence in 1964 [30].

The strong interaction is described by the theory of quantum chromodynamics (QCD). The Lagrangian for the QCD interaction can be written

Tab. 1.1: Boson fields in the SM

Symbol	Associated Charge	Symmetry group
B_μ	weak hypercharge Y	$U(1)_Y$
$G_\mu^{1,\dots,8}$	color $C = (r, g, b)$	$SU(3)_C$
$W_\mu^{1,2,3}$	weak isospin T_3	$SU(2)_L$

as

$$\mathcal{L}_{QCD} = \bar{\psi}(i\gamma^\mu D_\mu - m)\psi - \frac{1}{2}TrG_{\mu\nu}G^{\mu\nu} \quad (1.5)$$

27 where

$$G_{\mu\nu} = \partial_\mu G_\nu - \partial_\nu G_\mu - ig_s[G_\mu, G_\nu] \quad (1.6)$$

$$D_\mu = \partial_\mu - ig_s G_\mu \quad (1.7)$$

28 g_s is related to the strong coupling constant, and m is the fermion mass,
 29 which in this case must be a quark since they are the only fermions with
 30 color charge.

31 *1.2 Electroweak Symmetry Breaking*

A crucial feature of the SM is electroweak symmetry breaking. The electroweak interaction, first proposed by Glashow, Weinberg, and Salam in the 60's, is the unified description of electromagnetic and weak interactions under the $SU(2)_L \otimes U(1)_Y$ symmetry. The electromagnetic interaction is described by quantum electrodynamics (QED), which is an Abelian gauge theory under the $U(1)_{EM}$ symmetry group. The gauge boson in QED is the

Tab. 1.2: Fermions in the SM. The first two numbers listed in the third column give the supermultiplet representation under $SU(3)_C$ and $SU(2)_L$ respectively. A **1** means that it is not charged under that group and therefore will not couple to the associated force. A **3** as the first number means that it has color charge and couples to the strong force. A **2** for the second number means that it has weak isospin and couples to the weak force. The third number gives the value of the weak isospin. Adjoint representation is specified by the presence of a bar over the number.

Name	Notation	Representation under $SU(3)_C \otimes SU(2)_L \otimes U(1)_Y$
Left-handed quark doublet	$\begin{pmatrix} u_L \\ d_L \end{pmatrix}, \begin{pmatrix} c_L \\ s_L \end{pmatrix}, \begin{pmatrix} t_L \\ b_L \end{pmatrix}$	(3, 2, $\frac{1}{6}$)
Right-handed up-type quark singlet	$u_R^\dagger, c_R^\dagger, b_R^\dagger$	($\bar{3}$, 1, $-\frac{2}{3}$)
Right-handed down-type quark singlet	$d_R^\dagger, s_R^\dagger, t_R^\dagger$	($\bar{3}$, 1, $\frac{1}{3}$)
Left-handed lepton doublet	$\begin{pmatrix} \nu_{eL} \\ e_L \end{pmatrix}, \begin{pmatrix} \nu_{\mu L} \\ \mu_L \end{pmatrix}, \begin{pmatrix} \nu_{\tau L} \\ \tau_L \end{pmatrix}$	(1, 2, $-\frac{1}{2}$)
Right-handed charged lepton singlet	$e_R^\dagger, \mu_R^\dagger, \tau_R^\dagger$	($\bar{1}$, 1, 1)

photon and couples to electric charge Q . The QED Lagrangian is given by

$$\mathcal{L}_{QED} = \bar{\psi}(i\gamma^\mu D_\mu - m)\psi - \frac{1}{4}F_{\mu\nu}F^{\mu\nu} \quad (1.8)$$

³² where

$$F_{\mu\nu} = \partial_\mu A_\nu - \partial_\nu A_\mu \quad (1.9)$$

$$D_\mu = \partial_\mu + ieQA_\mu \quad (1.10)$$

³³ and A_μ is the electromagnetic or photon field.

The Lagrangian for the unbroken $SU(2)_L \otimes U(1)_Y$ symmetry is given by

$$\mathcal{L}_{EW} = \bar{\psi}i\gamma^\mu D_\mu\psi - Tr\frac{1}{8}W_{\mu\nu}W^{\mu\nu} - \frac{1}{4}B_{\mu\nu}B^{\mu\nu} \quad (1.11)$$

³⁴ where

$$W_{\mu\nu} = \partial_\mu W_\nu - \partial_\nu W_\mu - ig_w[W_\mu, W_\nu] \quad (1.12)$$

$$B_{\mu\nu} = \partial_\mu B_\nu - \partial_\nu B_\mu \quad (1.13)$$

with a separate fermion term for each field ψ_R and ψ_L . The covariant derivative D_μ is given by

$$D_\mu = \partial_\mu + ig_wT_iW_\mu^i + ig_Y\frac{Y}{2}B_\mu \quad (1.14)$$

³⁵ with W_μ^i and T_i written in terms of raising and lowering operators

$$W_\mu^\pm = \frac{1}{\sqrt{2}}(W_\mu^1 \mp W_\mu^2) \quad (1.15)$$

$$T^\pm = \frac{1}{\sqrt{2}}(T_1 \pm T_2) \quad (1.16)$$

$$W_\mu^0 = W_\mu^3 \quad (1.17)$$

$$T^0 = T_3 \quad (1.18)$$

The neutral portion of the covariant derivative $ig_w T_3 W_\mu^3 + ig_Y \frac{Y}{2} B_\mu$ must contain the electromagnetic term $ieA_\mu Q$ for the electromagnetic interaction to be unified with the weak interaction, so the W_μ^3 and B_μ fields need to linear combinations of the photon field A_μ and another field Z_μ . This relationship can be written in terms of the electroweak mixing angle θ_w , also known as the Weinberg angle, as

$$\begin{pmatrix} A_\mu \\ Z_\mu \end{pmatrix} = \begin{pmatrix} \cos \theta_w & \sin \theta_w \\ -\sin \theta_w & \cos \theta_w \end{pmatrix} \begin{pmatrix} B_\mu \\ W_\mu^3 \end{pmatrix} \quad (1.19)$$

The weak isospin T_3 and weak hypercharge Y can be related to the electric charge Q with the Gell-Mann-Nishijima formula

$$Y = 2(Q - T_3) \quad (1.20)$$

³⁶ and the coupling constants g_w , g_Y , and e are related to the mixing angle by

$$e = g_w \cos \theta_W = g_Y \sin \theta_W \quad (1.21)$$

$$\sin \theta_W = \frac{g_Y}{\sqrt{g_w^2 + g_Y^2}} \quad (1.22)$$

$$\cos \theta_W = \frac{g_w}{\sqrt{g_w^2 + g_Y^2}} \quad (1.23)$$

At this point the $W_\mu^{1,2,3}$ and B_μ fields have been mixed to produce the observable fields W_μ^+ , W_μ^- , A_μ , and Z_μ , but this is still inconsistent with experimental observations as these bosons and all of the fermions are still massless in this model. In order to generate the masses while maintaining the renormalizability of the gauge theory the symmetry needs to be spontaneously broken. This is done by the introduction of a complex scalar doublet field called the Higgs field which is expressed as

$$\phi = \begin{pmatrix} \phi^+ \\ \phi^0 \end{pmatrix} = \frac{1}{\sqrt{2}} \begin{pmatrix} \phi_1 + i\phi_2 \\ \phi_3 + i\phi_4 \end{pmatrix} \quad (1.24)$$

where the fields ϕ_i are real scalar fields. The Lagrangian for the Higgs field is

$$\mathcal{L}_{Higgs} = (D_\nu \phi)^\dagger (D^\nu \phi) - V(\phi^\dagger \phi) \quad (1.25)$$

with the potential $V(\phi^\dagger \phi)$ being given by

$$V(\phi^\dagger \phi) = \mu^2 \phi^\dagger \phi + |\lambda| (\phi^\dagger \phi)^2 \quad (1.26)$$

and the covariant derivative

$$D_\nu = \partial_\nu - \frac{i}{2}g_w W_\nu^i \sigma_i - \frac{i}{2}g_Y B_\nu \quad (1.27)$$

Since $\mu^2 < 0$, this potential has the shape of a sombrero as is shown in Figure 1.1. The scalar fields have some positive vacuum expectation value (VEV) satisfying

$$\phi^\dagger \phi = v = \sqrt{-\frac{\mu^2}{\lambda}} \quad (1.28)$$

at the minimum which allows us to write the ground state as

$$\phi_{ground} = \langle 0 | \phi | 0 \rangle = \frac{1}{\sqrt{2}} \begin{pmatrix} 0 \\ v \end{pmatrix} \quad (1.29)$$

Expanding the Higgs field about it's minimum as

$$\phi_{ground} \rightarrow \phi(x) = \frac{1}{\sqrt{2}} e^{i\sigma_\alpha \theta^\alpha(x)} \begin{pmatrix} 0 \\ v + h(x) \end{pmatrix}, \alpha = 1, 2, 3 \quad (1.30)$$

³⁷ results in a massive field $h(x)$ and and three massless scalar fields, or Goldstone bosons, $\theta_{1,2,3}$ which represent degrees of freedom. By then transforming into the unitary gauge we can remove the phase factor, thereby eliminating the explicit appearance of the three Goldstone bosons in the Lagrangian. In gauging away the Goldstone bosons, the three degrees of freedom reappear as longitudinal polarization states of the W^+ , W^- , and Z bosons. In other words, the W and Z bosons have become massive by "eating" the Goldstone bosons.

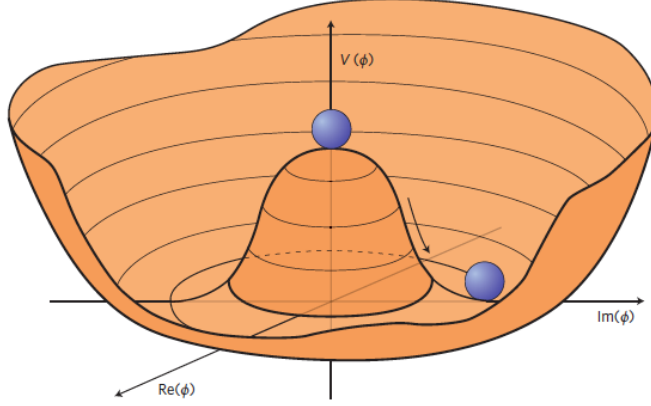


Fig. 1.1: The Higgs potential is shown as a function of the complex scalar field's real and imaginary parts. The balls illustrate that the stable vacuum state of nature is not located at $\phi = 0$ because the symmetry at that point is spontaneously broken. Instead the stable vacuum state of nature is located somewhere along the circle of minimum potential. Reprint from [6]

Writing the Lagrangian in Equation 1.25 in terms of the physical W and Z fields and evaluating at the VEV gives

$$\begin{aligned} \mathcal{L}_{Higgs} = & \frac{1}{2} \partial_\nu h \partial^\nu h + \frac{1}{4} g_w^2 W_\nu^+ W^{-\nu} (v + h)^2 \\ & + \frac{1}{8 \cos^2 \theta_W} Z_\nu Z^\nu (v + h)^2 - V \left[\frac{1}{2} (v + h)^2 \right] \end{aligned} \quad (1.31)$$

⁴⁵ The v^2 terms give the W and Z boson masses and the h^2 term gives the

⁴⁶ mass of the Higgs boson as

$$M_W = \frac{1}{2} g_w v \quad (1.32)$$

$$M_Z = \frac{1}{2} v \frac{g_w}{\cos \theta_W} = \frac{M_W}{\cos \theta_W} \quad (1.33)$$

$$M_H = \sqrt{2} |\mu| \quad (1.34)$$

⁴⁷ while the photon remains massless.

Charged leptons and quarks also acquire mass through Yukawa interactions via the Higgs mechanism. For leptons the Yukawa interaction has the form of

$$\mathcal{L}_{Yukawa} = -G_e [\bar{e}_R \phi^\dagger \ell_L + \bar{\ell}_L \phi e_R] \quad (1.35)$$

where

$$\ell_L = \begin{pmatrix} \nu_{eL} \\ e_L \end{pmatrix} \quad (1.36)$$

⁴⁸ and G_e is an arbitrary coupling parameter. Note that this is the Yukawa term for the electron doublet. The muon and tau doublets would have the same form. Then using the unitary gauge version of ϕ we get

$$\mathcal{L}_{Yukawa} = -\frac{G_e}{\sqrt{2}}(v+h)(\bar{e}_L e_R + \bar{e}_R e_L) \quad (1.37)$$

$$= -\frac{G_e v}{\sqrt{2}}(\bar{e}e) - \frac{G_e}{\sqrt{2}}(h\bar{e}e) \quad (1.38)$$

where the electron mass is given by

$$m_e = \frac{G_e v}{\sqrt{2}}. \quad (1.39)$$

Repeating the process for the second and third lepton generations gives the muon and tau masses as

$$m_\mu = \frac{G_\mu v}{\sqrt{2}}, m_\tau = \frac{G_\tau v}{\sqrt{2}} \quad (1.40)$$

⁵¹ Since there are no ν_R fields in the SM, neutrinos are not able to acquire

⁵² mass the way charged leptons do.

In order to generate quark masses for both the up and down-type quarks it's necessary to use ϕ , which has $Y = 1$, and the conjugate multiplet which is given by

$$\tilde{\phi} = \begin{pmatrix} \phi^{0*} \\ -\phi^- \end{pmatrix} \quad (1.41)$$

and has $Y = -1$. The conjugate multiplet then, similar to ϕ , breaks to

$$\tilde{\phi} \rightarrow \begin{pmatrix} v + h \\ 0 \end{pmatrix} \quad (1.42)$$

The Yukawa term for the first generation quarks has the form

$$\mathcal{L}_{Yukawa} = -G_d \bar{q}_L \phi d_R - G_u \bar{q}_L \tilde{\phi} u_R + h.c. \quad (1.43)$$

where G_d and G_u are arbitrary coupling parameters and

$$q_L = \begin{pmatrix} u_L \\ d_L \end{pmatrix}. \quad (1.44)$$

Applying the broken *phi* and $\tilde{\phi}$ gives us

$$\mathcal{L}_{Yukawa} = -(m_d \bar{d}d + m_u \bar{u}u)(1 + \frac{h}{v}) \quad (1.45)$$

where the mass eigenstates are

$$m_q = \frac{G_q v}{\sqrt{2}}. \quad (1.46)$$

53 It's worth noting that for each of these masses there is an arbitrary
 54 coupling parameter (G_q , G_e , G_μ , and G_τ). This means that the values of
 55 the fermion masses are not predicted by SM, but these parameters are tuned
 56 to reflect observation.

57 At this point we can summarize the particle content of the SM and their
 58 allowed interactions in a way that is seen in Figure 1.2.

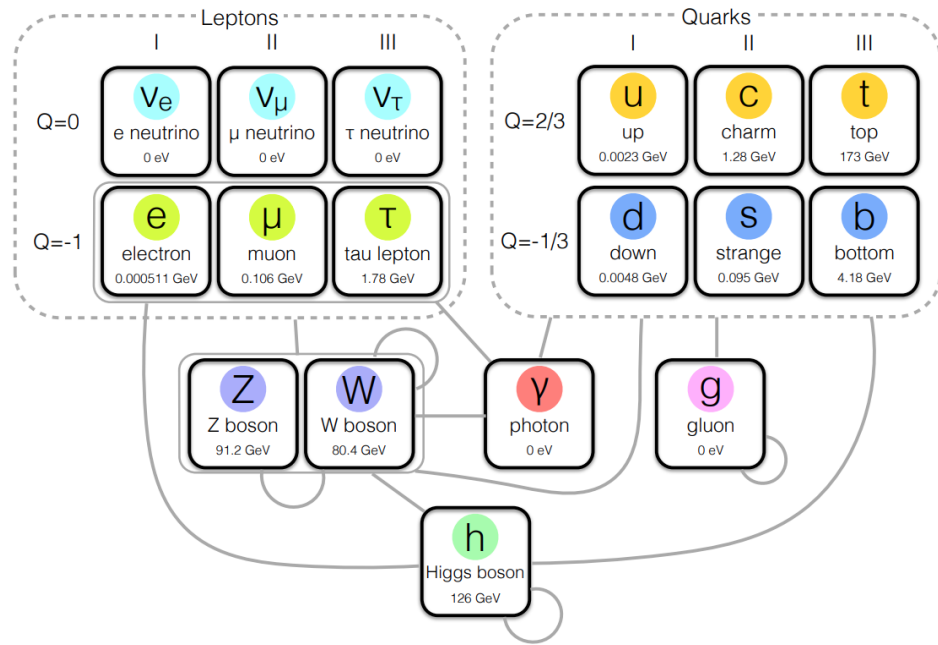


Fig. 1.2: Summary of particle content in the SM. Gray lines connecting groups of particles indicates allowed interactions. Self-coupling is indicated by a gray line connecting a particle to itself. The leptons and quarks are organized in columns corresponding to generation, which is specified at top, and rows corresponding to electric charge Q , which is listed to the left. Each particle's mass is listed beneath its name and symbol. It should be noted that neutrinos in the SM are still treated as massless leptons despite the fact that experimental evidence has established that at least two of the neutrinos are massive. Reprinted from [32]

1.3 Problems with the SM

2. SUPERSYMMETRY

61

3. THE LARGE HADRON COLLIDER

62

3.1 *Introduction*

63 The Large Hadron Collider (LHC) is a 26.7 kilometer-long, two-ring particle
64 accelerator and collider located on the border of France and Switzerland at
65 the European Organization for Nuclear Research (CERN). During normal
66 operations the LHC maintains two counter-rotating beams of proton bunches
67 that collide at four interaction points (IP) with up to $\sqrt{s} = 14$ TeV center
68 of mass energy and a luminosity of $10^{34}\text{cm}^{-2}\text{s}^{-1}$. The ALICE (Point 2),
69 ATLAS (Point 1), CMS (Point 5), and LHC-b experiments each have a
70 detector at one of these interaction points as scene in Figure 3.1 . The CMS
71 and ATLAS are general-purpose detectors while LHC-b specializes in beauty
72 quark studies. ALICE is a heavy-ion experiment which uses $^{208}\text{Pb} - p$ or
73 $^{208}\text{Pb} - ^{208}\text{Pb}$ collisions that can also be produced by the LHC.

74

3.2 *Injection Complex*

75 In order to bring the protons from rest up to their target collision energy
76 a series of accelerators, as shown in Figure 3.2, are used. The acceleration
77 sequence begins with the injection of hydrogen gas into a duoplasmatron.
78 Here a bombardment of electrons ionize the hydrogen atoms while an electric

79 field pushes them through the duoplasmatron cavity. The result is 100 keV
80 protons being passed on to a quadrupole magnet which guides them into
81 the aperture of a linear accelerator (LINAC2). The radio frequency (RF)
82 cavities in LINAC2 accelerate the protons up to 50 MeV. At this point the
83 protons are sent into one of four rings in the Proton Synchrotron Booster
84 (PSB). The PSB repeatedly accelerates the protons around a circular path
85 until they reach an energy of 1.4 GeV. The bunches of protons from each PSB
86 ring are then sequentially injected into the single-ringed Proton Synchrotron
87 (PS). Each bunch injected into the PS are captured by one of the "buckets"
88 (Figure 3.3) provided by the PS RF system which also manipulates the
89 bunches into the desired profile and proton density. These proton bunches
90 are accelerated to 25 GeV and injected into the Super Proton Synchrotron
91 (SPS) where they are accelerated to 450 GeV. Finally the proton bunches
92 are injected into the LHC ring where they are accelerated to 6.5 TeV and
93 collided in 25 ns intervals to yield a center of mass energy of $\sqrt{s} = 13$ TeV.

94 *3.3 Tunnel and Magnets*

95 The LHC was designed to produce collisions with up to $\sqrt{s} = 14$ TeV. That
96 requires confining and guiding 7 TeV protons around the circumference of
97 the LHC ring. The ring is housed in a 4 meter-wide underground tunnel
98 that ranges in depth between 45 and 170 meters below the surface. This
99 tunnel was repurposed from the Large Electron-Positron (LEP) Collider
100 which previously occupied the space. For this reason the tunnel is not
101 completely circular but is instead made up of alternating curved and straight

102 sections of 2500 m and 530 m in length respectively. The straight sections,
103 labeled 1-8 in Figure 3.1, are used as either experimental facilities or sites for
104 hardware necessary for LHC operations such as RF cavities for momentum
105 cleaning, quadrupole magnets for beam focusing, and sextupole magnets for
106 acceleration and betatron cleaning.

107 Steering a 7 TeV proton beam around the curved sections requires a mag-
108 netic field of 8.33 Tesla which is provided by 1223 superconducting dipole
109 magnets cooled to 1.9 K. A cross section of the LHC dipole is shown in
110 Figure 3.4. Supercooled liquid helium flows through the heat exchanger
111 pipe to cool the iron yolk to a temperature of 1.9 K. Ultra high vacuum
112 is maintained in the outer volume to provide a layer of thermal insulation
113 between the inner volume and the outer steel casing. Inside the iron yolk is a
114 twin bore assembly of niobium-titanium superconducting coils. Two parallel
115 beam pipes are located within the focus of the superconducting coils. This
116 is the ultra high vacuum region where the subatomic particles are confined
117 as they travel around the LHC ring.

118 *3.4 Luminosity*

The number of events generated per second for specific process having cross-
section σ_{event} is given by:

$$\frac{dN_{event}}{dt} = L\sigma_{event} \quad (3.1)$$

where L is the machine luminosity. The machine luminosity for a Gaussian beam distribution can be written in terms of the beam parameters as:

$$L = \frac{N_b^2 n_b f_{rev} \gamma_r}{4\pi \epsilon_n \beta_*} F \quad (3.2)$$

where N_b is particle density in each bunch, n_b is the number of bunches in each beam, f_{rev} is the frequency of revolution, and γ_r is the relativistic gamma factor. The variables ϵ_n and β_* are the normalized transverse beam emittance and the beta function at the IP respectively, while F is the geometric reduction factor depending due to the beams' crossing angle at the IP. [24]

The total number of events produced over a given amount of time would then be

$$N_{event} = \sigma_{event} \int L dt = \sigma_{event} L_{integrated}. \quad (3.3)$$

The integrated luminosity delivered each year to the CMS experiment is shown in 3.5. The analysis presented here uses data collected from the 2016, 2017, and 2018 campaigns which gives a combined integrated luminosity of 158.7 fb^{-1} .

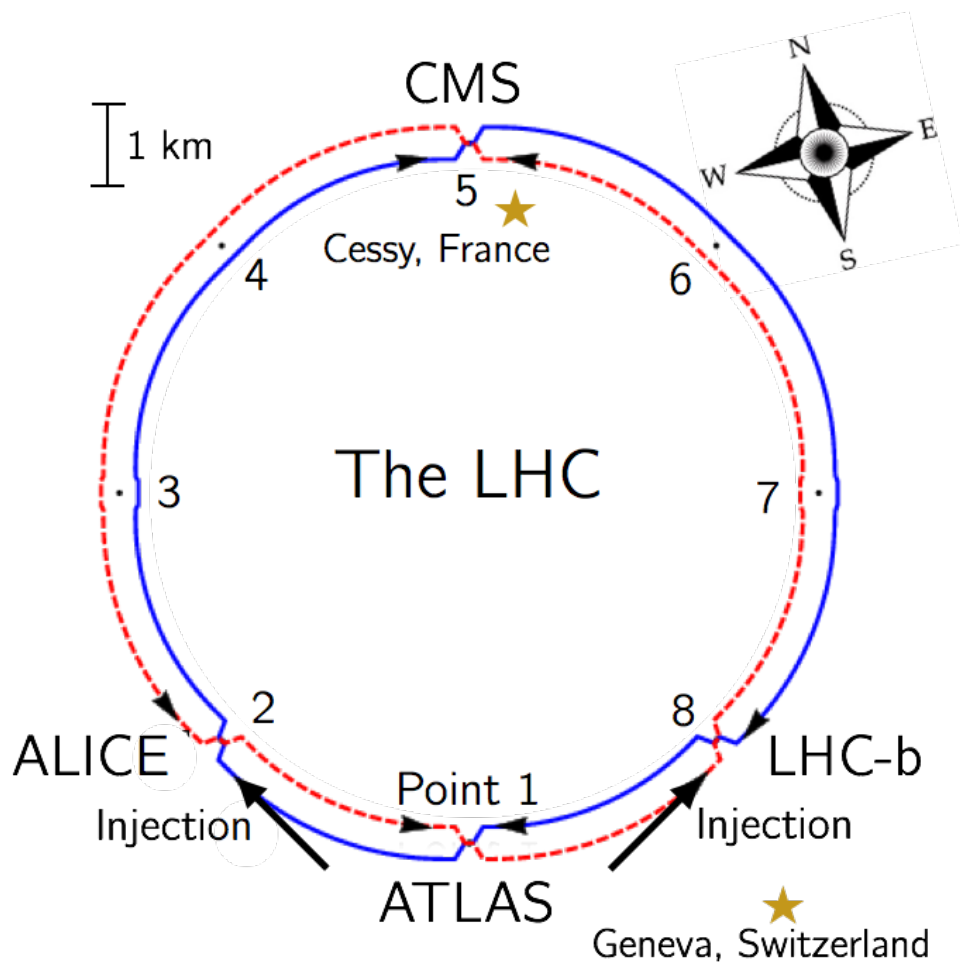


Fig. 3.1: Interaction points of the LHC

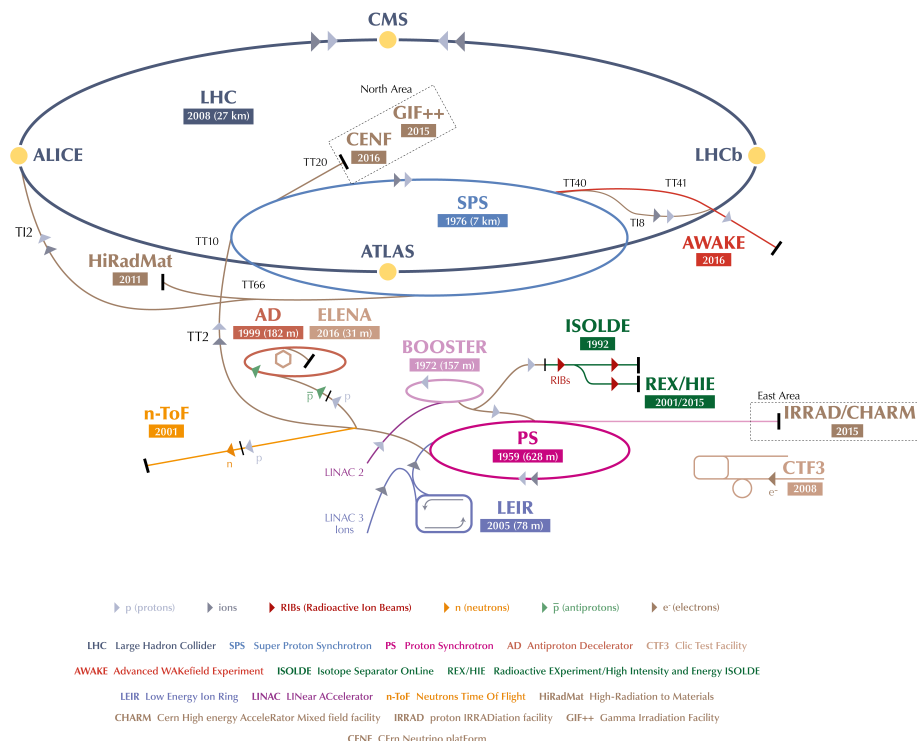


Fig. 3.2: Layout of LHC accelerator complex [24].

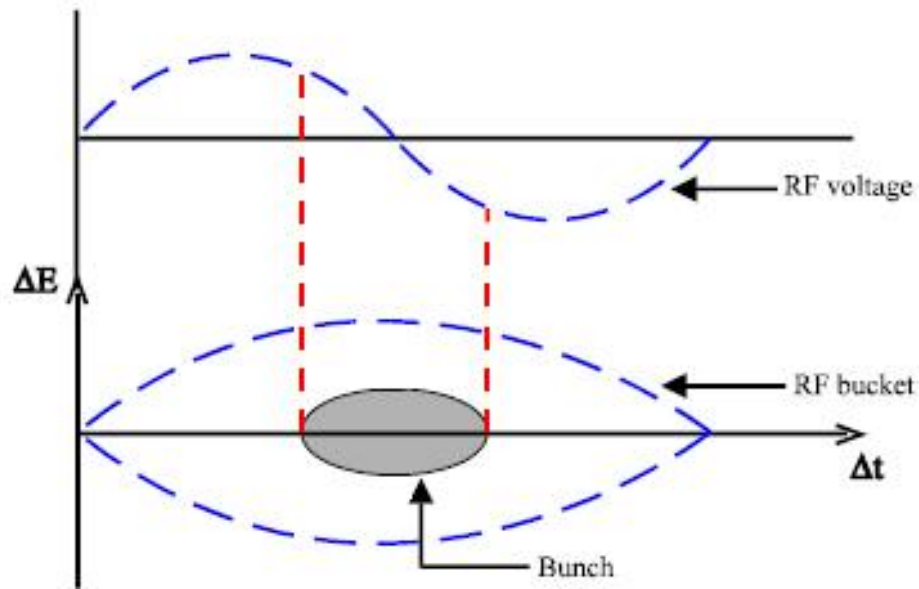
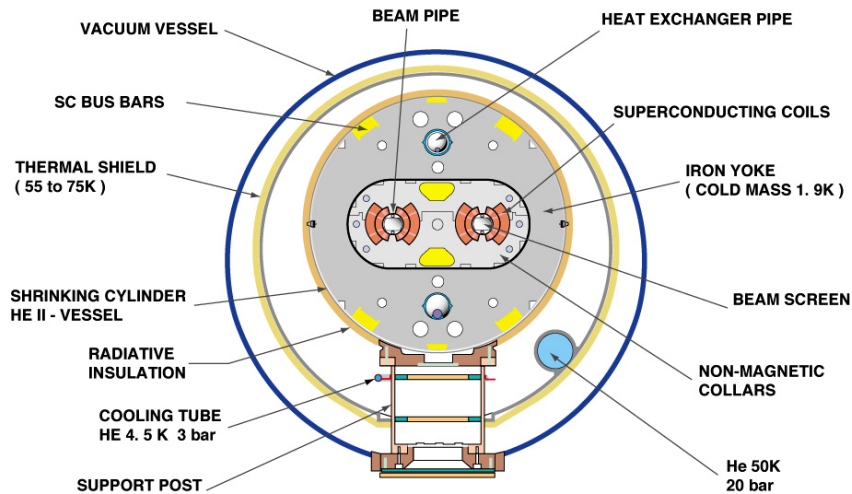


Fig. 3.3: Proton bunch capture onto RF bucket [9].

CROSS SECTION OF LHC DIPOLE



CERN AC _HE107A_ V02/02/98

Fig. 3.4: Cross section of LHC dipole [14]

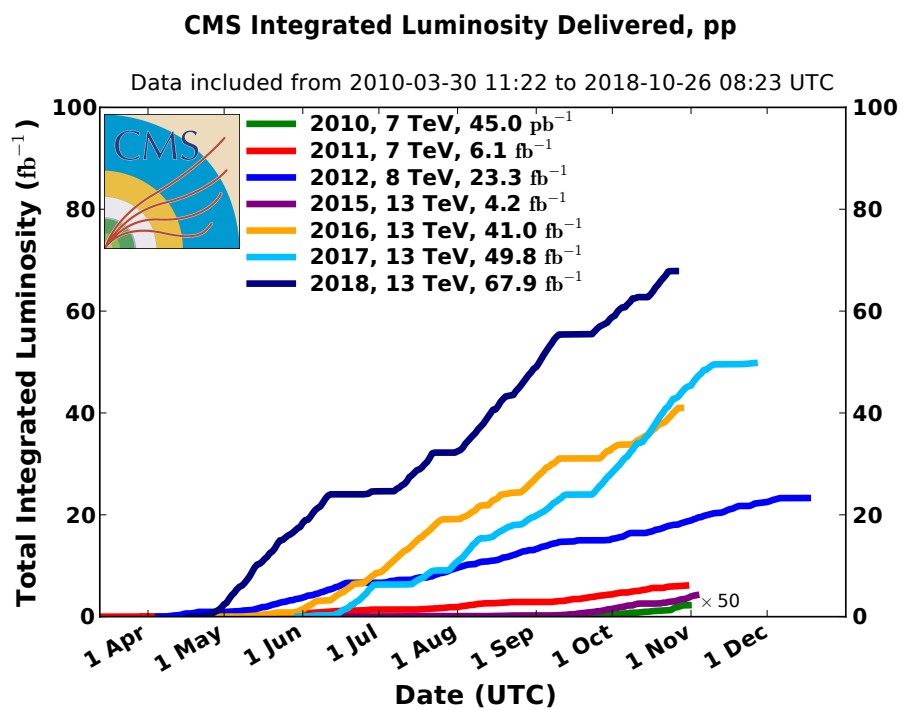


Fig. 3.5: Integrated luminosity delivered by the LHC to the CMS experiment each year from 2010-2018.

129

4. COMPACT MUON SOLENOID

130

4.1 *Introduction*

131 About 100 meters below the town of Cessy, France at Point 5 is the Compact
132 Muon Solenoid (CMS). The CMS is a general purpose detector weighing
133 14,000 tonnes with a length of 28.7 meters and a 15.0-meter diameter that
134 was designed to accurately measure the energy and momentum of particles
135 produced in the proton-proton or heavy-ion collisions at the LHC [20]. A
136 perspective view of of the detector is shown in Figure 4.1. In order to get
137 a full picture of what is being produced by the collisions the CMS detector
138 must be able identify the resulting particles as well as accurately measure
139 their energy and momentum. For this reason the detector was designed to
140 be a collection of specialized sub-detectors, each of which contributes data
141 used in the reconstruction of a collision.

142 At the heart of the CMS detector is a 3.8-Tesla magnetic field produced
143 by a superconducting solenoid. Inside the 6-meter diameter solenoid are
144 three layers of sub-detectors. These make up the inner detector and are, in
145 order from innermost to outermost, the silicon tracker, the electromagnetic
146 calorimeter (ECAL), and the hadronic calorimeter (HCAL). Outside the
147 solenoid is the muon system. A transverse slice of the detector (Figure 4.2)

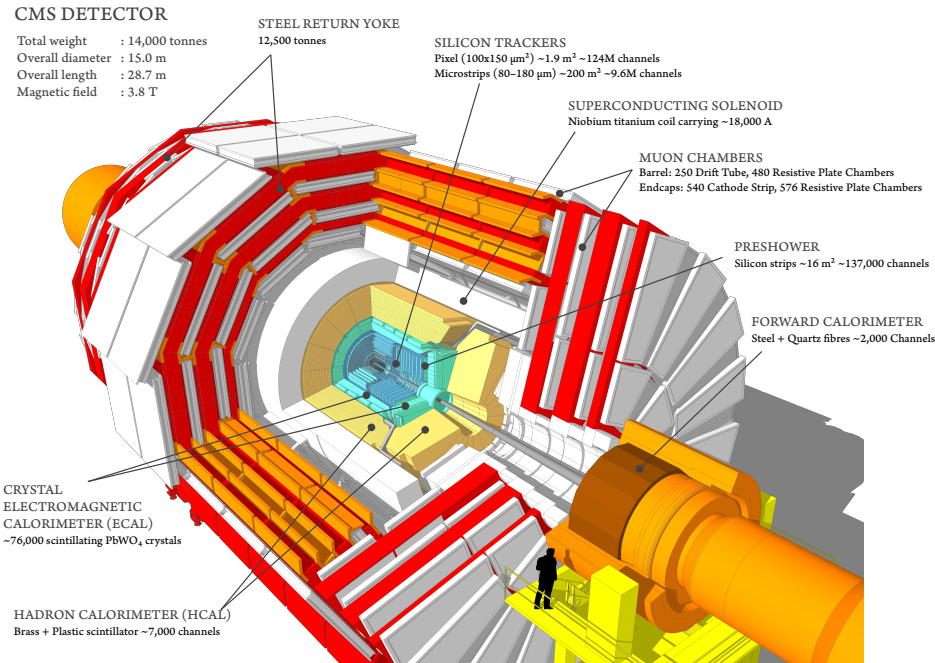


Fig. 4.1: Schematic of CMS detector [36]

148 shows the sub-detectors and how different types of particles interact with
 149 with them. Table 4.1 shows a summary of which sub-detectors are expected
 150 to produce signals for different types of particles.

Particle	Tracker	ECAL	HCAL	Muon
Photons	No	Yes	No	No
Electrons	Yes	Yes	No	No
Hadrons (charged)	Yes	Yes	Yes	No
Hadrons (neutral)	No	No	Yes	No
Muons	Yes	Yes	Yes	Yes
Invisible (ν , SUSY, etc)	No	No	No	No

Tab. 4.1: Summary of signals expected for each particle type in each sub-detector.

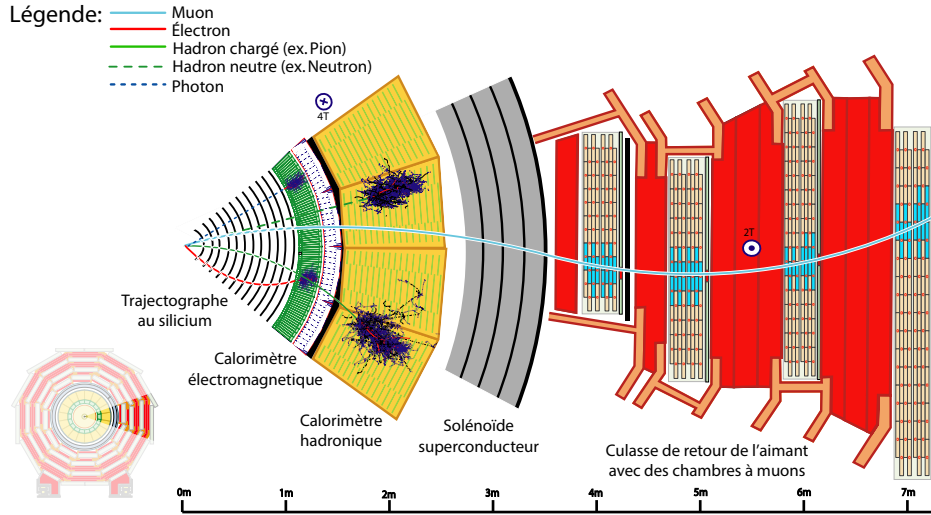


Fig. 4.2: Transverse slice of the CMS detector[10].

151

4.2 Coordinate System

The origin of the coordinate system used by CMS is centered at the nominal collision point in the center of the detector. A right-handed Cartesian system is used with the x-axis pointing radially inward toward the center of the LHC ring, y-axis pointing vertically upward, and the z-axis pointing tangent to the LHC ring in the counterclockwise direction as viewed from above. CMS also uses an approximately Lorentz invariant spherical coordinate system spanned by three basis vectors. They are the transverse momentum p_T , pseudorapidity η , and azimuthal angle ϕ . The transverse momentum and azimuthal angle translate to the Cartesian system in the following ways

using the x and y-components of the linear momentum:

$$p_T = \sqrt{(p_x)^2 + (p_y)^2} \quad (4.1)$$

$$\phi = \tan^{-1} \frac{p_y}{p_x} \quad (4.2)$$

while the pseudorapidity can be translated using the polar angle θ relative the positive z-axis as

$$\eta = -\ln[\tan \frac{\theta}{2}] \quad (4.3)$$

152

4.3 Tracker

153 The innermost sub-detector in CMS is the silicon tracker. The tracker is
 154 used to reconstruct tracks and vertices of charged particles. In order to give
 155 precise reconstruction of charged particle trajectories it needs to be position
 156 as close as possible to the IP and have high granularity. The close proximity
 157 to the IP requires the materials to be tolerant to the high levels of radiation
 158 in that region. Being the innermost sub-detector it must also minimally
 159 disturb particles as they pass through it into the other sub-detectors. These
 160 criteria led to the design of the tracker using silicon semiconductors.

161 The silicon tracker is made up of two subsystems, an inner pixel detector
 162 and an outer strip tracker which are oriented in a cylindrical shape with an
 163 overall diameter of 2.4 m and length of 5.6 m centered on the interaction
 164 point. Both subsystems consist of barrel and endcap regions which can be
 165 seen in Figure 4.3.

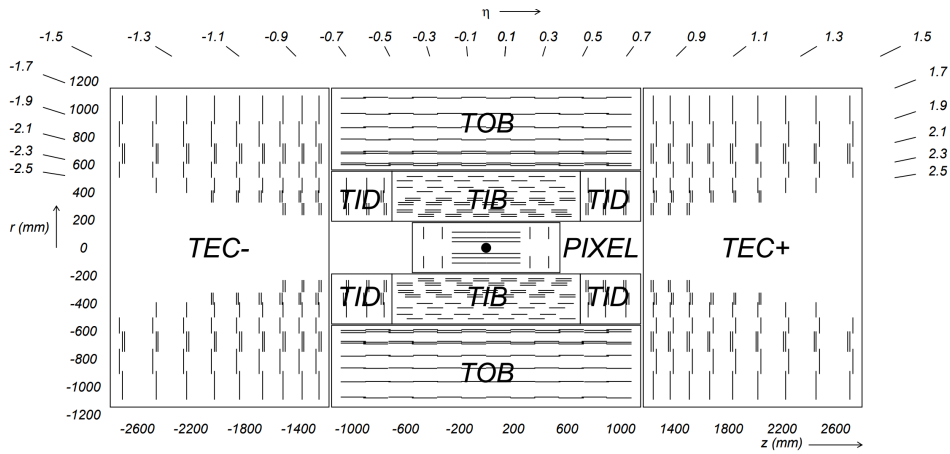


Fig. 4.3: Cross section (side) of CMS tracker prior to the Phase 1 upgrade during the year-end technical stop of 2016/2017. Each line represents a detector module while double lines indicate back-to-back strip modules. Surrounding the pixel tracker (PIXEL) is the strip detector, which is divided into the Tracker Inner Barrel (TIB), Tracker Outer Barrel (TOB), Tracker Inner Disks (TID), and Tracker Endcaps (TEC). Reprinted from Reference [19].

166

4.3.1 Pixel Detector

167 The pixel detector is the innermost subsystem in the silicon tracker and
 168 spans the pseudorapidity range $|\eta| < 2.5$ and is responsible for small im-
 169 pact parameter resolution which is important for accurate reconstruction of
 170 secondary vertices [20]. In order to produce these precise measurements a
 171 very high granularity is required. In addition to this the proximity to the
 172 IP means that one expects there to be high occupancy of the tracker. These
 173 constraints are met by using pixels with a cell size of $100 \times 150 \mu\text{m}^2$.

174 The original pixel detector was designed for operation at the nominal
 175 instantaneous luminosity of $10^{34} \text{ cm}^{-2}\text{s}^{-1}$ with 25 ns between proton bunch
 176 crossings, resulting in on average about 25 proton-proton interactions occur-

ring per bunch crossing or pileup [19]. During the LHC technical shutdown of 2016/17, the pixel detector underwent the scheduled Phase 1 upgrade which would allow operation at higher levels of instantaneous luminosity and pileup. Figure 4.4 shows a cross sectional view in the r - z plane. Prior to 2017 there were three barrel layers and two endcap layers on each side which provide three very precise space points for each charged particle. The upgrade decreased the radius of the innermost barrel layer from 4.4 cm to 3.0 cm and added a fourth barrel layer as well as adding third endcap layer to each side. Each of the endcap layers consisted of two half-disks populated with pixel modules whereas the upgraded endcap layers were split into inner and outer rings. [18]

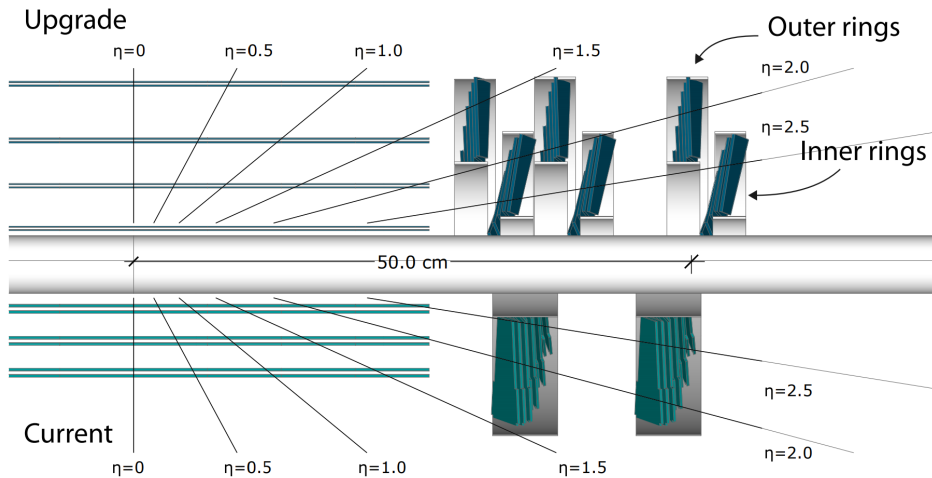


Fig. 4.4: Cross section (side) of pixel detector. The lower half , labeled "Current", shows the design prior to 2017 while the upper half, labeled "Upgrade", shows the design after the upgrade. Reprinted from Resource [18]

188

4.3.2 Strip Detector

189 The silicon strip detector surrounds the pixel detector and is comprised of
190 four subsystems, the Tracker Inner Barrel (TIB), the Tracker Outer Barrel
191 (TOB), the Tracker Inner Disks (TID), and the Tracker Endcaps (TEC),
192 all of which can be seen in Figure 4.3 [20]. The TIB and TID both use
193 320 μm thick silicon micro-strip sensors oriented along z and r respectively.
194 The TIB has four layers while the TID is composed of three layers. This
195 geometry allows the TIB and TID to combine to provide up to four $r - \phi$
196 measurements on charged particle trajectories.

197 Surrounding the TIB and TID is the TOB, which extends between $z \pm 118$
198 cm. This subsystem consists of six layers of 500 μm thick silicon micro-strip
199 sensors with strip pitches ranging from 122 μm to 183 μm , providing six
200 more $r - \phi$ measurements in addition to those from the TIB/TID subsystems.
201 Beyond the z range of the TOB is the TEC. Each TEC is made up of nine
202 disks. Each of the nine disks has up to seven concentric rings of micro-strip
203 sensors oriented in radial strips with those on the inner four rings being
204 320 μm thick and the rest being 500 μm thick, providing up to nine ϕ
205 measurements for the trajectory of a charged particle.

206 To provide additional measurements of the z coordinate in the barrel and
207 r coordinate in the disks a second micro-strip detector module is mounted
208 back-to-back with stereo angle 100 mrad in the first two layers of the TIB
209 and TOB, the first two rings of the TID, and rings 1, 2, and 5 of the TEC.
210 The resulting single point resolution is 230 μm in the TIB and 530 μm in the
211 TOB. The layout of these subsystems ensures at least nine hits for $|\eta| < 2.4$

212 with at least four of hits yielding a 2D measurement.

213 *4.4 Electromagnetic Calorimeter*

214 The electromagnetic calorimeter (ECAL) lies just outside the tracker and is a
215 hermetic homogeneous calorimeter designed to measure the energy deposited
216 by electrons and photons. It consists of a central barrel (EB) with 61200
217 lead tungstate (PbWO_4) crystals which is closed by two endcaps (EE), each
218 having 7324 crystals. Highly-relativistic charged particles passing through a
219 crystal primarily lose energy by producing bremsstrahlung photons. Photons
220 lose energy by producing $e^- - e^+$ pairs. In front of each EE is a preshower
221 (ES) detector which acts as a two-layered sampling calorimeter. The crystals
222 in the EB are instrumented with avalanche photodiodes (APDs) while the
223 EE crystals are instrumented with vacuum phototriodes (VPTs). The ECAL
224 design was strongly driven to be sensitive to the di-photon decay channel
225 of the Higgs boson. This led to the design of a calorimeter that was fast,
226 radiation-hard, and had good spatial and energy resolution.

227 *4.4.1 Crystals*

228 In order to provide a good spacial resolution it was necessary for the ECAL
229 to have a fine granularity. The small Molier radius (22 mm) and short radia-
230 tion length (8.9 mm) of PbWO_4 allows for fine granularity while maintaining
231 good energy resolution by containing nearly all of the energy from an EM
232 shower without the need for a restrictively thick crystal layer. The PbWO_4
233 scintillation is also fast enough that approximately 80 percent of an EM

shower is produced within 25 ns, which is also the amount of time between bunch crossings at the LHC. These crystals have a Gaussian-shaped spectrum spanning from 360 nm to 570 nm with a maximum at approximately 440 nm. While PbWO_4 is relatively radiation-hard, the amount of ionizing radiation seen by the crystal leading up to the HL-LHC era of operations causes wavelength-dependent degradation in light transmission. The scintillation mechanism however is unchanged so this damage can be tracked and accounted for by injecting laser light near the peak wavelength of the emission spectrum into the crystals to monitor optical transparency.

Light produced in the crystal is transmitted along its length and collected at the rear by either an APD in the EB or a VPT in one of the EE. Light output is temperature dependent so the crystals are kept at precisely 18°C at which the yield is about 4.5 photoelectrons per MeV. The EB and EE crystals, which have a truncated pyramidal shape to match the lateral development of the shower, along with their photosensors are shown in Figure 4.5.



Fig. 4.5: PbWO_4 crystals. Left: EB crystal with APD. Right: EE crystal with VPT. Reprinted from [20]

250

4.4.2 Barrel and Endcaps

251 The EB covers the pseudorapidity range $|\eta| < 1.479$ and uses crystals that
252 are 230 mm long, which corresponds to 25.8 radiation lengths. The front
253 face of each crystal measures $22 \times 22 \text{ mm}^2$ while the rear face measures 26×26
254 mm^2 . These are grouped in 36 supermodules (SM), each comprised of 1700
255 crystals arranged in a 20×85 grid in $\phi \times \eta$. Each SM spans half the length
256 of the barrel and covers 20° in ϕ . On the back face of each crystal is a
257 pair of APDs (semiconductor diodes). APDs are compact, immune to the
258 longitudinal 3.8 T magnetic field produced by the solenoid at this location,
259 and resistant to the radiation levels expected in the EB over a ten year
260 period. They also have high enough gain to counter to low light yield of
261 the crystals. All of this makes them an ideal choice for use in the EB. Each
262 APD has an active area of $5 \times 5 \text{ mm}^2$ and are operated at a gain of 50 which
263 requires a bias voltage between 340 and 430 V. As the gain of the APDs is
264 highly dependent on the applied bias voltage and any gain instability would
265 translate to degradation in energy resolution, very stable power supplies are
266 used to maintain voltages within a few tens of mV.

267 The EE cover the pseudorapidity range $1.497 < |\eta| < 3.0$. The crystals in
268 the EE have a $28.62 \times 28.62 \text{ mm}^2$ front face cross section and $30 \times 30 \text{ mm}^2$ rear
269 face cross section. Each crystal is 220 mm long which corresponds to 24.7
270 radiation lengths and are grouped in 5×5 units called supercrystals (SCs).
271 Two halves, called *Dees*, make up each EE. Each Dee contains 138 SCs and
272 18 partial SCs which lie along the inner and outer circumference. On the
273 back of each crystal in EE is a VPT which is a conventional photomultiplier

with a single gain stage. While not as compact as the APDs used in the EB, the VPTs are a more suitable for the more hostile environment at higher η . Each VPT has a 25-mm diameter and approximately 280 mm^2 of active area. Though the VPT gain and quantum efficiency are lower than that of the APDs this is offset by the larger active area allowing for better light collection. Figure 4.6 shows the orientation of the crystals, modules, and supermodules within the ECAL. [20]

4.4.3 Preshower layer

In front of each EE is a preshower (ES) detector. The main purpose of the ES is to identify photons resulting from $\pi^0 \rightarrow \gamma\gamma$ within the pseudorapidity range $1.653 < |\eta| < 2.6$, but it also aids in the identification of electrons against minimum ionizing particles (MIPs) and provides a spacial resolution of 2 mm compared to the 3 mm resolution of the EB and EE. The ES acts as a two-layered sampling calorimeter. Lead radiators make up the first layer. These initiate electromagnetic showers from incoming electrons or photons. The deposited energy and transverse profiles of these showers are then measured by the silicon strip sensors which make up the second layer.

4.4.4 Performance

The energy resolution of the ECAL can be parameterized as

$$\frac{\sigma}{E} = \frac{S}{\sqrt{E}} \oplus \frac{N}{E} \oplus C \quad (4.4)$$

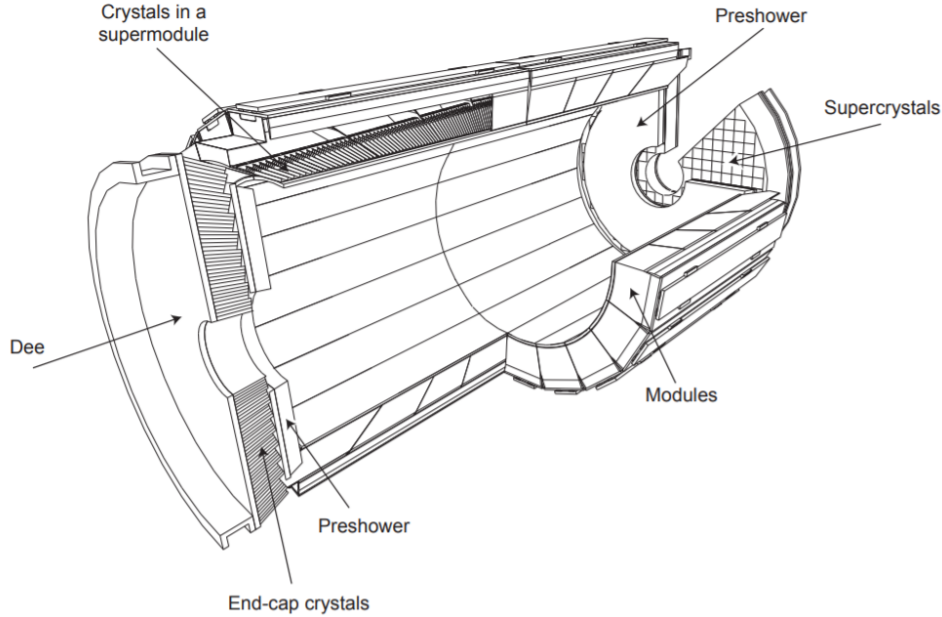


Fig. 4.6: Schematic of ECAL. Reprint from [20]

where S is the stochastic term characterizing the size of photostatistical fluctuations, N is the term characterizing the contributions of electronic, digital, and pileup noise, and C is a constant which accounts for crystal performance non-uniformity, intercalibration errors, and leakage of energy from the back of a crystal. The values for these terms, as measured in a beam test using 20 to 250 GeV electrons, are $S = 0.028 \text{ GeV}^{1/2}$, $N = 0.12 \text{ GeV}$, and $C = 0.003$. [20]

4.5 Hadronic Calorimeter

In the space between the bore of the superconducting magnet and the ECAL is the Hadronic Calorimeter (HCAL) [2]. The HCAL is a sampling calorimeter used for the measurement of hadronic jets and apparent missing trans-

verse energy resulting from neutrinos or exotic particles. It is made up of alternating layers of plastic scintillator tiles and brass absorbers. EM showers are generated by charged/neutral hadrons in the brass absorber. Charged particles in the shower then produce scintillation light in the plastic scintillator. Wavelength-shifting optical fibers embedded in the scintillator collect and guide the scintillation light to pixelated hybrid photodiodes. A longitudinal cross-section view in Figure 4.7 shows the geometric layout of the HCAL's barrel (HB), outer barrel (HO), endcap (HE), and forward (HF) sections. The HB is comprised of 17 scintillator layers extending from 1.77 to 1.95 m and covers the pseudorapidity range of $|\eta| < 1.4$. The HO lies outside the solenoid and is composed of only scintillating material. This increases the interaction depth of the calorimeter system to a minimum of $11\lambda_I$ for $|\eta| < 1.26$ and thus reduces energy leakage. Also located inside the solenoid are the two HE which cover pseudorapidities $1.3 < |\eta| < 3.0$ and provide a thickness of $10\lambda_I$. In the forward region is the HF. This is located 11.2 m away from the IP and covers the $2.9 < |\eta| < 5.2$. As the HF is exposed to the highest levels of particle flux, it uses quartz fibers embedded in steel absorbers rather than the materials used in the other parts of the HCAL. Showers initiated by the absorbers produce Cerenkov light in the quartz which transmits along to the fibers to photomultiplier tubes (PMTs).

The HCAL inherently has lower energy resolution than the ECAL. A large portion of the energy from hadronic showers is deposited in the absorbers and never makes it to the scintillation material. There are also the possibilities that showers can be initiated prior to the particles reach-

ing HCAL or a charged particle could deposit energy in the ECAL through bremsstrahlung. The combined energy resolution of the ECAL and the HCAL barrels can be parameterized as

$$\frac{\sigma}{E} = \frac{S}{\sqrt{E}} \oplus C, \quad (4.5)$$

where E is the energy of the incident particle. These quantities were measured in a beam test using 2 to 350 GeV/c hadrons, electrons, and muons. The stochastic term is $S = 0.847 \text{ GeV}^{1/2}$, and the constant term is $C = 0.074$ [5].

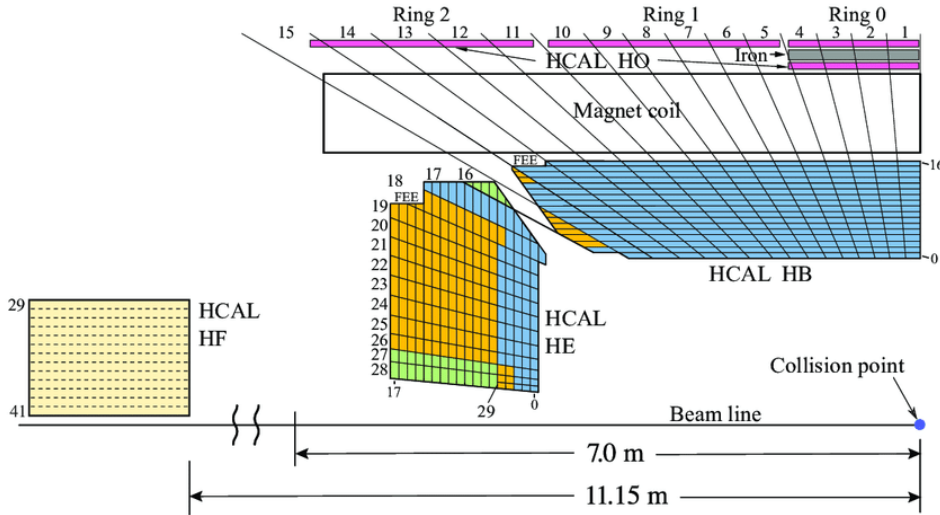


Fig. 4.7: Longitudinal view of HCAL [2]

4.6 Superconducting Solenoid

In between the HCAL barrel and outer barrel is the superconducting solenoid magnet. The magnet is 12 m long with a 6-m inner diameter and provides

the bending power necessary to precisely measure the momentum of charged particles. While it is capable of producing a 4 T magnetic field, the magnet is typically operated at 3.8 T. This is done to prolong the lifetime of the magnet. The Niobium Titanium coils used to create the uniform 3.8-T magnetic field are suspended in a vacuum cryostat and cooled by liquid helium to a temperature of 4.5 K. The magnet has a stored energy of 2.6 GJ when operating at full current. There are five wheels in the barrel and three disks on each endcap that make up a 12,000 ton steel yoke which serves to return the magnetic flux. This, along with a mapping of the calculated field strength, can be seen in Figure 4.8. More details on the superconducting solenoid magnet can be found at [1]

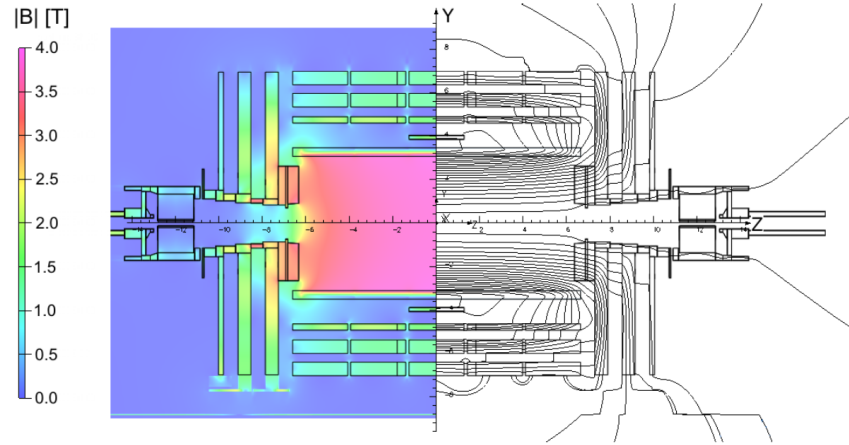


Fig. 4.8: Longitudinal slice of CMS detector while operating at 3.8-T central magnetic field. The right-hand side of the figure shows a mapping of the magnetic field lines while the left-hand side shows a mapping of the field strength. Reprint from [16]

342

4.7 Muon System

343 Embedded in magnet return yoke and encapsulating all of the other sub-
344 detectors is the muon system. The muon system is the outermost layer
345 because muons don't interact via the strong force and electromagnetic in-
346 teractions alone are not enough stop them due to their large mass, therefore
347 the only particles that are capable of making it to the muon system are
348 muons and weakly-interacting particles such as neutrinos. The muon sys-
349 tem is comprised of three different types of detectors. These are drift tube
350 (DT) chambers, cathode strip chambers (CSC), and resistive plate chambers
351 (RPC). A cross-sectional view of the muon system along with the rest of the
352 CMS detector is shown in Figure 4.9.

353 The DT chambers are used barrel region for $|\eta| < 1.2$. Each chamber is
354 comprised of three superlayers which are made up of four staggered layers
355 of rectangular drift cells. Each of these drift cells contains a mixture of
356 Ar and CO₂ gases. An anode wire, located at the center of each tube, is
357 made of gold-plated stainless steel and is held at 3.6 kV. The gas is ionized
358 when a charged particle passes through and the resulting free electrons are
359 attracted to the anode wire. As these electrons pass through the gas they
360 cause further ionization which results in an electron avalanche. The layers
361 of drift cells are oriented in such a way that two of the three superlayers
362 give the muon position in the ϕ -direction and one gives the position in the
363 z -direction. The result is a spacial resolution of 77-123 μm along the ϕ
364 direction and 133-193 μm along the z direction for each DT chamber [21].

365 On the endcaps, covering the pseudorapidity range of $0.9 < |\eta| < 2.4$,

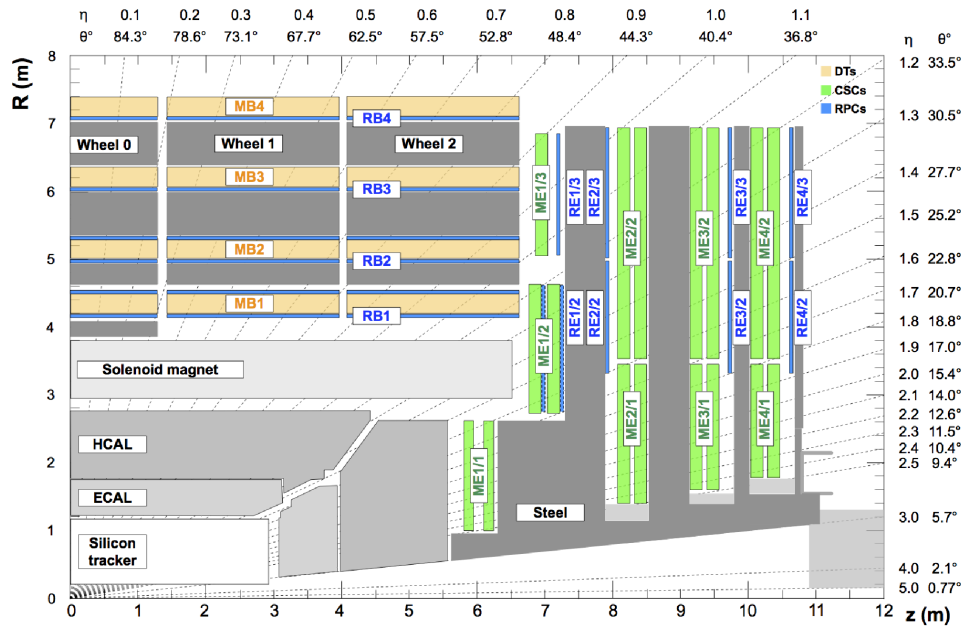


Fig. 4.9: Cross-section of one quadrant of the CMS detector. The DTs are labeled as "MB" (Muon Barrel) and the CSCs are labelled as "ME" (Muon Endcap). The RPCs are "RB" for those in the barrel and "RE" for those in the endcap. Reprint from [39].

366 are the CSCs. In this region there is a higher muon flux as well non-uniform
367 magnetic fields so this portion of the muon system must have higher gran-
368 ularity provided by the CSCs. Each of these chambers contain panels that
369 divide it into six staggered layers. The cathode strips are oriented along the
370 r -direction to give position measurements in the ϕ -direction while anode
371 wires run perpendicular in between the panels to give r -direction position
372 measurements. The spacial resolution provided by the CSCs is 45-143 μm
373 [39].

374 Both the endcap and barrel regions, spanning $|\eta| < 1.6$, contain RPCs to
375 provide more precise timing measurements. Each RPC is a gaseous parallel-
376 plate detector. High voltage is applied to two large plates which have a
377 layer of gas between them. Outside the chamber is an array of cathode
378 strips which is used to detect electron cascades resulting from muons passing
379 through and ionizing the gas. Where the DTs and CSCs provide precise
380 position information, the RPCs have a very fast response time which gives
381 a time resolution better than 3 ns [39]. This allows for the RPCs to be used
382 as a dedicated muon trigger that can insure each muon is assigned to the
383 correct bunch crossing.

384

5. CMS TRIGGER SYSTEM

385 When operating at nominal luminosity the LHC produces over 1 billion
386 proton-proton collisions per second. Finite computing speed and storage
387 capacity limit the rate at which CMS can record events to be about 1 kHz
388 [13]. Decreasing the rate from 1 GHz to 1 kHz is accomplished by using
389 a two-level trigger system to quickly decide which events will be discarded
390 and which will be recorded. The first stage is a hardware-based Level 1 (L1)
391 trigger and the second stage is software-based High Level Trigger (HLT).

392

5.1 *L1 trigger*

393 The L1 trigger decreases the rate by about six orders of magnitude from 1
394 GHz to 100 kHz by performing rough calculations on information from the
395 ECAL, HCAL, and muon subsystems using field-programmable gate arrays
396 (FPGAs). The L1 trigger can be divided further into the calorimeter and
397 muon triggers. The schematic of the L1 trigger system in Figure 5.1 shows
398 both the calorimeter and muon triggers. The calorimeter trigger trigger
399 uses information from the ECAL and HCAL subdetectors to construct pho-
400 ton, electron, and jet candidates in addition to quantities such as missing
401 transverse momentum and total hadronic activity. The muon trigger uses
402 information from all three muon subsystems to construct muon candidates.

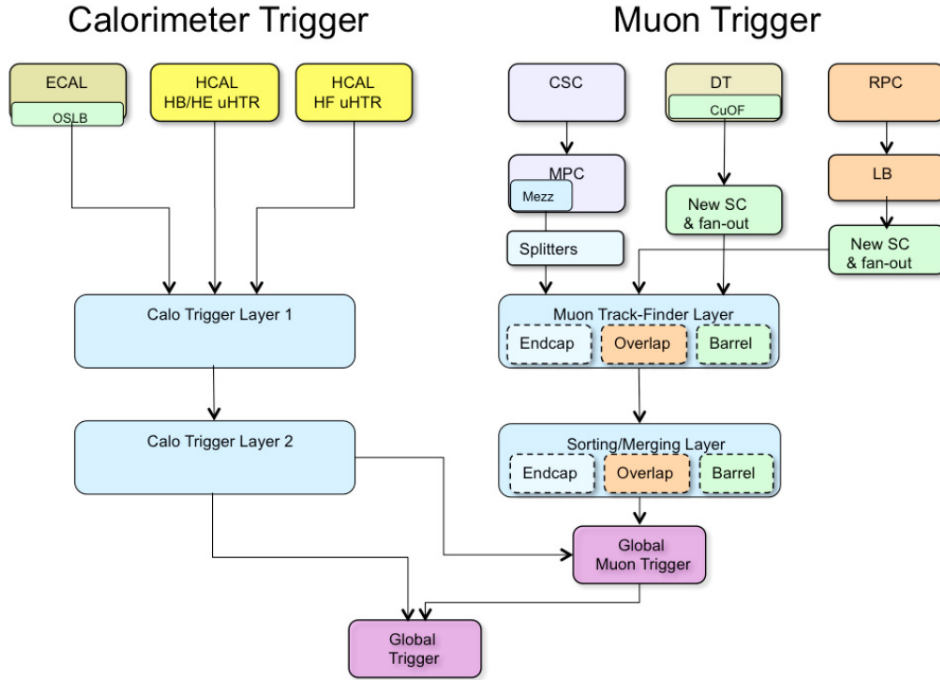


Fig. 5.1: L1 trigger system. Reprint from [3]

403 The outputs from the calorimeter and muon triggers goes into the Global
 404 Trigger (GT) which decides which events should be recorded and which are
 405 to be discarded [42].

406 5.1.1 Calorimeter trigger

407 Trigger Primitives (TP) are the raw inputs from the ECAL and HCAL
 408 for the calorimeter trigger. The TP, which contain information regarding
 409 the energy deposits in the calorimeters, are passed to the first layer of the
 410 calorimeter trigger. This first layer consists of several FPGA cards that
 411 receive data from several bunch crossings, but are each mapped to a section
 412 of the detector. This data is then passed on to the second layer in such a way

413 that each FPGA in this layer will receive data for the entire calorimeter for
414 each bunch crossing. Candidate objects are then constructed and organized
415 into a sorted list according to transverse momentum and passed on to the
416 GT and the global muon trigger.

417 *5.1.2 Muon trigger*

418 TP for the muon trigger come from the three muon detectors, the CSCs,
419 DTs, and RPCs. These are then passed on to the first layer of the muon
420 trigger (Muon Track-Finding Layer) where the TP are combined to recon-
421 struct muon tracks for sections of ϕ for different regions of $|\eta|$. The barrel
422 track-finder for $|\eta| < 0.83$, the endcap track-finder for $|\eta| > 1.24$, and the
423 overlap track-finder for $0.83 < |\eta| < 1.24$. This data is passed on to the
424 second layer where the sections of ϕ are merged and subsequently passed
425 on to the global muon trigger where it is combined with the output from
426 Calo Trigger Layer 2 to compute isolation. The global muon trigger then
427 combines the η regions and passes a list of the top eight muon candidates
428 to the GT.

429 *5.1.3 Global Trigger*

430 Final processing of the reconstructed objects and quantities constructed by
431 the calorimeter and muon triggers is carried out by the GT. L1 algorithms
432 or "seeds" are implemented by the GT using these objects. A full set of L1
433 seed is called a L1 menu and can be adjusted to meet the requirements of
434 the CMS physics program. Each L1 seed can be given a "prescale", which is
435 an integer value N that can be used to reduce the rate of a particular trigger

436 path. This is done by only applying the trigger to one out of N events and
437 can be used to take advantage of the current LHC running conditions.

438 *5.2 High Level Trigger*

439 Events that are accepted by the L1 trigger are passed on to the HLT which
440 is based in software and is therefore capable of analyzing events with a higher
441 degree of sophistication. The HLT has access to information from the full
442 detector and implements "paths" to select events of interest from those pass-
443 ing the L1 trigger. Each HLT path is a set of criteria that is used to either
444 accept or reject an event. The full set of HLT paths is the HLT menu. Each
445 HLT path is "seeded" by one or more L1 seeds in order to decrease comput-
446 ing time. That means that a given HLT path will only be processed if the
447 L1 bits associated with its seed or seeds fire. Each HLT path is assigned to
448 a primary dataset depending on its general physics signature. In the case
449 of this analysis, the primary dataset used for signal events was DoubleEG
450 for years 2016 and 2017. This was merged into the EGamma dataset for
451 2018. The SingleMuon dataset was used for trigger efficiency studies. A list
452 of the primary HLT used for each year along with its associated primary
453 dataset is listed in Table 5.1. The HLT path for 2016 is different because
454 HLT_DoublePhoton70 was not a part of the HLT menu until 2017.

Tab. 5.1: Primary HLT

Year	HLT path	Primary dataset
2016	HLT_DoublePhoton60	DoubleEG
2017	HLT_DoublePhoton70	DoubleEG
2018	HLT_DoublePhoton70	EGamma

5.3 Trigger efficiency

456

6. CMS PARTICLE AND EVENT RECONSTRUCTION

457 After an event is chosen to be stored by the trigger system, the output from
458 all of the sub-detectors is saved and recorded to disk as "RAW" data. These
459 data contain information about the response of each sub-detector, such as
460 tracker hits and energy deposition in the calorimeters. As was mentioned
461 in Chapter 4, shown in Table 4.1 and Figure 4.2, the CMS was designed
462 such that each type of particle resulting from the pp collisions at the IP
463 would leave a distinct signature in the sub-detectors. This allows for the
464 information to be reconstructed into lists of physics object candidates such
465 as photons, electrons, muons, etc and quantities such as missing transverse
466 momentum. The particle flow (PF) algorithm performs this reconstruction
467 by first building tracks and calorimeter clusters. These two elements are the
468 inputs to the reconstruction of the aforementioned physics object candidates
469 using a "link" algorithm.

470

6.1 Tracks

471 A combinatorial track finder algorithm based on the Kalman filtering tech-
472 nique uses the hits in the silicon tracker to reconstruct tracks of charged
473 particles [25]. Each iteration of the algorithm is comprised of three steps:

- 474 • Seed generation: Find a seed consisting of two to three hits that is

475 compatible with a track from a charged particle.

476 • Track finding: Use pattern recognition to identify any hits that are
477 compatible with the trajectory implied by the seed generated in the
478 first step.

479 • Track fitting: Determine the properties of the track, such as origin,
480 trajectory, and transverse momentum by performing a global χ^2 fit.

481 The first iteration uses stringent requirements on the seeds and the χ^2
482 of the track fit to pick out isolated jets which have very high purity. The
483 hits associated with these high purity tracks are then removed to reduce the
484 combinatorial complexity for subsequent iterations. This allows successive
485 iterations to identify less obvious tracks by progressively loosening criteria
486 while the removal of previously associated hits mitigates the likelihood of
487 fake tracks being built.

488 6.2 Calorimeter clusters

489 Calorimeter clusters are constructed using energy deposition information
490 from the calorimeters. Clusters are formed by first identifying the seed cell
491 (ECAL crystal or HCAL scintillating tile) that corresponds to the local
492 maxima of an energy deposit that is above a given threshold. Neighboring
493 cells are then aggregated to grow topological clusters if their signals are
494 above twice the standard deviation of the level of electronic noise.

495

6.3 Object identification

496 At this point the tracks and calorimeter clusters are linked to form a PF
497 block. This linkage is done with an algorithm that quantifies the likelihood
498 that a given track and cluster were results of the same particle. As PF blocks
499 are identified as object candidates they are removed from the collection prior
500 to each subsequent iteration until all tracks and clusters have been assigned
501 to a PF object candidate. The following sections will outline how each of
502 these PF objects is identified.

503

6.3.1 Muons

504 Muons are the easiest particle to identify, so they are the first objects recon-
505 structed in the CMS. PF Muons are classified in three categories depending
506 on how their tracks are reconstructed:

- 507 • Tracker muons: Tracks reconstructed from the inner tracker having
508 $p_T > 0.5$ GeV and $|\vec{p}| > 2.5$ GeV that, when propagated to the muon
509 system, match at least one hit in the muon chambers.
- 510 • Stand-alone muons: Tracks reconstructed only using hits in the muon
511 system.
- 512 • Global muons: Stand-alone muons that coincide with a track from the
513 inner tracker.

514 After a muon is reconstructed it is given an identification or ID based on
515 observables such as the χ^2 of the track fit, how many hits were recorded
516 per track, or how well the tracker and stand-alone tracks matched. These

517 IDs represent different working points (loose, medium, and tight) which
518 correspond to increasing purity but decreasing efficiency as you move from
519 loose toward tight.

520 *6.3.2 Electrons*

521 The next objects reconstructed in the CMS are electrons. Bremsstrahlung in
522 the tracker layers causes substantial energy loss and changes in momentum
523 which requires the use of a dedicated tracking algorithm. In place of the
524 Kalman filtering technique, a Gaussian-sum filter (GSF) algorithm is used.
525 This algorithm uses a weighted sum of Gaussian PDFs which does a bet-
526 ter job of modeling the Bremsstrahlung effects than the Kalman filtering
527 technique which uses a single Gaussian PDF.

528 PF ECAL clusters are regrouped by identifying a seed cluster then asso-
529 ciating and adding clusters from Bremsstrahlung photons to form superclus-
530 ters. The schematic in Figure 6.1 shows how the Bremsstrahlung photons
531 are emitted in directions tangent to the trajectory of the electron. Electrons
532 bending in the magnetic field causes spreading of PF ECAL clusters to typ-
533 ically occur along the ϕ -direction. Two approaches are used to associate
534 the superclusters to GSF tracks. One is the ECAL-driven method, which
535 uses superclusters with $p_T > 4$ GeV as seeds for the GSF track finding al-
536 gorithm. This works well for high- p_T isolated electrons because the bend
537 radius is less severe which decreases the spread of the PF ECAL clusters.
538 This results in more of the Bremsstrahlung radiation being recovered and
539 correctly associated with an electron candidate. The second approach is the
540 tracker-driven method which uses tracks with $p_T > 2$ GeV as seeds that are

541 propagated out to the surface of the ECAL and used for clustering. This
 542 method works best with soft electrons like those in jets because it relies on
 543 the high granularity of the tracker to disentangle overlapping energy deposits
 544 in the ECAL. [35]

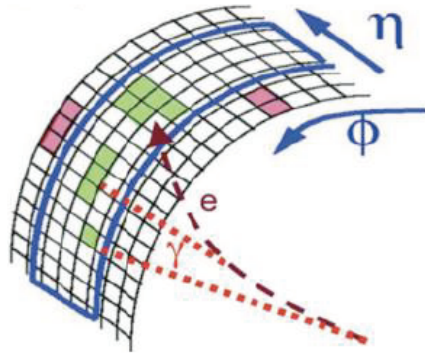


Fig. 6.1: The Bremsstrahlung photons continue along a straight trajectory while the electron path is bent by the magnetic field. This results in energy deposited in the calorimeter for such electrons to be spread out along the ϕ -direction.

545 As a final step, a boosted decision tree (BDT) is used to discriminate
 546 between real and fake electrons. The BDT is given variables associated with
 547 track-cluster matching, shower shape, and tracking. The output score of
 548 the BDT is used to classify electrons into loose, medium, and tight working
 549 points which exhibit to the same purity and efficiency trends as the muon
 550 working points.

551 6.3.3 Photons

552 Unlike electrons, photons typically deposit most of their energy in the ECAL
 553 without interacting with the tracker therefore their reconstruction is seeded

554 from ECAL superclusters that do not have any GSF tracks associated with
555 them. When photons interact with the tracker material they convert into
556 electron-positron pairs which follow bent trajectories due to the magnetic
557 field prior to entering the ECAL. This causes a spread of the energy deposi-
558 tion along the ϕ -direction. The goal of the clustering algorithm for photon
559 reconstruction is to include all of the energy deposits of electrons resulting
560 from photon conversions. As with the calorimeter clustering algorithm, the
561 photon clustering starts by identifying a local energy maxima as a seed crys-
562 tal. In the EB a cluster is made up of several parallel strips of crystals 5×1
563 in $\eta \times \phi$. The first strip has the seed crystal at its center. Neighboring strips
564 in the ϕ -direction are added if they have energy above a threshold of 10 GeV
565 but less than that of the subsequent strip with a maximum of 17 strips in
566 a cluster. In the EE, the seed cluster is 5×5 with adjacent 5×5 clusters
567 being added if they meet the minimum energy requirement.

568 Converted and unconverted photons can be differentiated by looking at
569 how the energy is distributed in a supercluster. The variable R_9 is used for
570 this purpose. It is defined as the ratio of the energy in a 3×3 crystal array to
571 the energy in the entire supercluster. As the energy deposits resulting from
572 converted electrons is more spread out they result in a lower R_9 value than
573 unconverted photons. A photon candidate is considered to be unconverted
574 when $R_9 > 0.93$.

575 An important point regarding the clustering algorithm is that it does
576 not differentiate between showers resulting from photons and those resulting
577 from electrons. This allows for electron from $Z \rightarrow ee$ events to be used as
578 high purity samples to study analysis inputs and for defining control regions

579 using electron in place of photons.

580 *6.3.4 Jets*

581 When quarks or gluons are produced they hadronize to make cone-shaped,
 582 collimated collections of particles called jets. The jet clustering algorithm
 583 aims to combine these particles in order to accurately measure the kine-
 584 matics of the initial gluon or quark. The algorithm uses the two distance
 585 parameters

$$d_{ij} = \min(k_{T_i}^{2p}, k_{T_j}^{2p}) \frac{\Delta R_{ij}^2}{R^2} \quad (6.1)$$

$$d_{iB} = k_{T_i}^{2p} \quad (6.2)$$

586 where d_{ij} is the distance between objects i and j and d_{iB} is the distance
 587 between object i and the beam B . The transverse momentum of the ob-
 588 ject is k_T . The parameter p is set as either -1, 0, or +1 to specify whether
 589 the anti- k_T , Cambridge/Aachen, or k_T algorithm is used, respectively. The
 590 difference between these three algorithms is which object pairs to combine
 591 first. The Cambridge/Aachen algorithm clusters starts by clustering par-
 592 ticles with the smallest angles between their 4-vectors. The k_T algorithm
 593 clusters soft particles first. And the anti- k_T algorithm clusters hard particles
 594 first. A comparison of these algorithms in Figure 6.2 shows that both the k_T
 595 and Cambridge/Aachen algorithms result in irregular clustering of partons
 596 while the anti- k_T algorithm results in more regular, circular jet shapes. The
 597 value of ΔR_{ij}^2 is defined as $(\eta_i - \eta_j)^2 + (\phi_i - \phi_j)^2$ and R is the distance
 598 parameter that defines the radius or cone size of the jet.

599 This analysis uses jets reconstructed from PF candidates using the anti- k_T
 600 algorithm with the cone size set to $R = 0.4$, also known as AK4PFJets or
 601 just PFJets. The algorithm goes through the following steps:

- 602 1. The smallest values of d_{ij} and d_{iB} are computed for all objects in the
 event.
- 604 2. Objects i and j are merged into a single object if $d_{ij} < d_{iB}$.
- 605 3. Object i is labeled as a jet and removed from the list if $d_{iB} < d_{ij}$.
- 606 4. This is repeated until there are no more objects.

After clustering, a series of jet energy corrections (JEC) are sequentially applied to the jets in order to improve calibration and energy resolution.

We define the jet p_T response as

$$\mathcal{R} = \frac{p_T}{p_T^{gen}} \quad (6.3)$$

607 where p_T is the measured or reconstructed transverse momentum of a jet
 608 and p_T^{gen} is the generator-level value. Ideally the distribution of \mathcal{R} would
 609 have $\langle \mathcal{R} \rangle = 1$, but this is not the case which is where the JEC come in.
 610 The first stage of the correction process is a flat correction to remove pileup
 611 contributions from the measured jet energy. A description of what pileup is
 612 and the mitigation process is available in Section 6.5. The next correction is
 613 a detector response correction derived from simulation in bins of η and p_T
 614 which is derived by comparing the measured and generator-level p_T in each
 615 bin. Next is a residual correction for differences between data and detector

616 simulation. This step exploits momentum conservation in the transverse
 617 plain by using dijet, $Z \rightarrow \mu\mu + \text{jet}$, and $\gamma + \text{jet}$ data events to derive correction
 618 factors. The result can be summarized as

$$\vec{p}_{corr} = C \cdot p_T^{raw} \quad (6.4)$$

$$= C_{PU}(p_T^{raw}, \eta) \cdot C_{sim}(p'_T, \eta) \cdot C_{res}(p''_T, \eta) \cdot \vec{p}_{raw} \quad (6.5)$$

619 where each of correction is applied sequentially such that p'_T is the trans-
 620 verse momentum after application of C_{PU} and p''_T is after the all subsequent
 621 correction have been applied. Once the JEC has been applied the mean of
 622 the jet response distribution should be very close to 1 and the width gives
 623 the jet energy resolution (JER).

624 6.4 Missing transverse momentum

The missing transverse momentum \vec{p}_T^{miss} is defined as the negative vector sum of transverse momentum over all PF objects and can be written as

$$\vec{p}_T^{\text{miss}} = - \sum_i \vec{p}_{Ti}. \quad (6.6)$$

We call the magnitude of this quantity the missing transverse energy E_T^{miss} . For reasons described in Section 7.6.1 a similar variable called the Hard E_T^{miss} is used in which only objects with $p_T > 30$ GeV are used so we have

$$\text{Hard}E_T^{\text{miss}} = \left| - \sum_i \vec{p}_{Ti} \cdot \Theta(30 - p_{Ti}) \right| \quad (6.7)$$

625 where the p_T is measured in units of GeV and Θ is a Heaviside function.

626 *6.5 Pileup mitigation*

Multiple interactions occurring in each bunch crossing is referred to as pileup (PU) and can affect reconstruction performance. The number of PU interaction, μ , is simply the number of interactions in a bunch crossing. It's calculated using Equation 6.8 where L_{inst} is the instantaneous luminosity, σ_{in}^{pp} is the total proton-proton inelastic cross section, and f_{rev} is the LHC orbit frequency.

$$\mu = L_{inst} \frac{\sigma_{in}^{pp}}{f_{rev}} \quad (6.8)$$

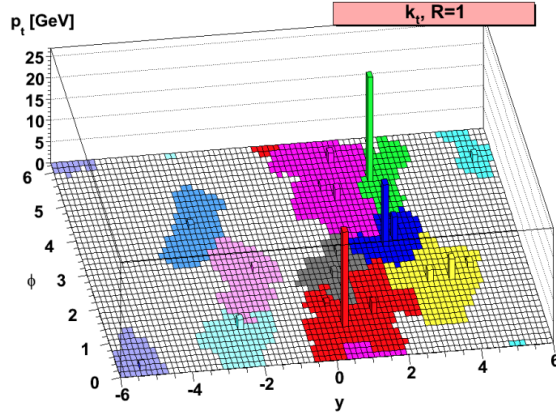
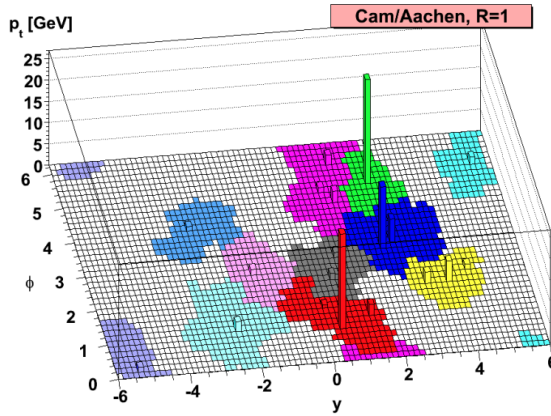
627 Figures 6.3, 6.4, and 6.5 show the distributions of PU interactions during
628 each year of datataking used in this analysis.

When analyzing an *event* we are looking at a single hard-scatter vertex in a bunch crossing. In order to do this, the PF algorithm must mitigate effects associated with additional PU vertices. Charged particles have track information from the silicon tracker and can be removed if they are associated with one of the additional PU vertices on an object-by-object basis, but this is not the case for neutral particles such as photons and neutral hadrons. These effects are instead removed from the event on average. Particular care must be taken to correct isolation variables, which take sum energy deposited within a specified cone of a target object. For example, an isolation variable for photons would sum the energy deposited from different object types (like charged hadrons, neutral hadrons, etc) in the vicinity of a target photon. For isolation variables the PU corrections are given by ρA_{eff}

where ρ is the event-specific energy density per unit area in $\eta \times \phi$ and A_{eff} is an effective area specific to the type of isolation. The corrected isolation variable would then be given by

$$I_{corrected} = \max(I - \rho A_{eff}, 0) \quad (6.9)$$

, with I being the uncorrected isolation, and is referred to as the ρ -corrected isolation.

(a) k_T jet clustering algorithm.

(b) Cambridge/Aachen jet clustering algorithm

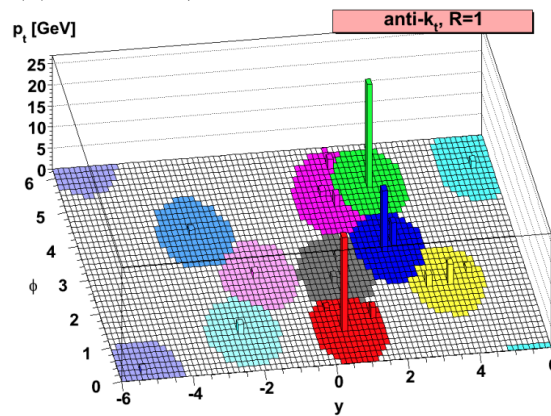
(c) Anti- k_T jet clustering algorithm

Fig. 6.2: Comparison of the k_T , Cambridge/Aachen, and anti- k_T jet clustering algorithms with the distance parameter set to $R = 1$. This is a sample parton-level event upon which each algorithm was applied. Of the three, the anti- k_T algorithm gives the most regularly shaped jets. Reprint from [12]

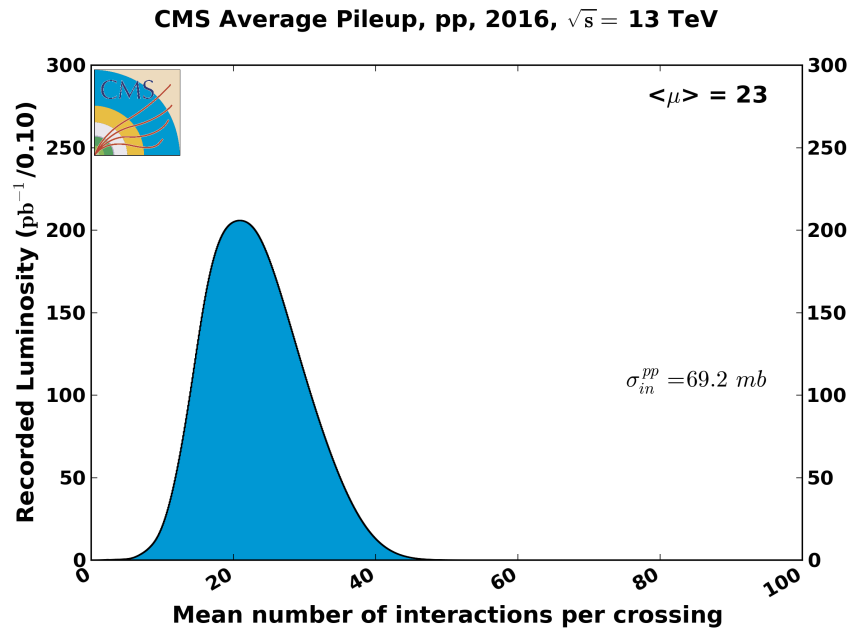


Fig. 6.3: Pileup distribution for 2016

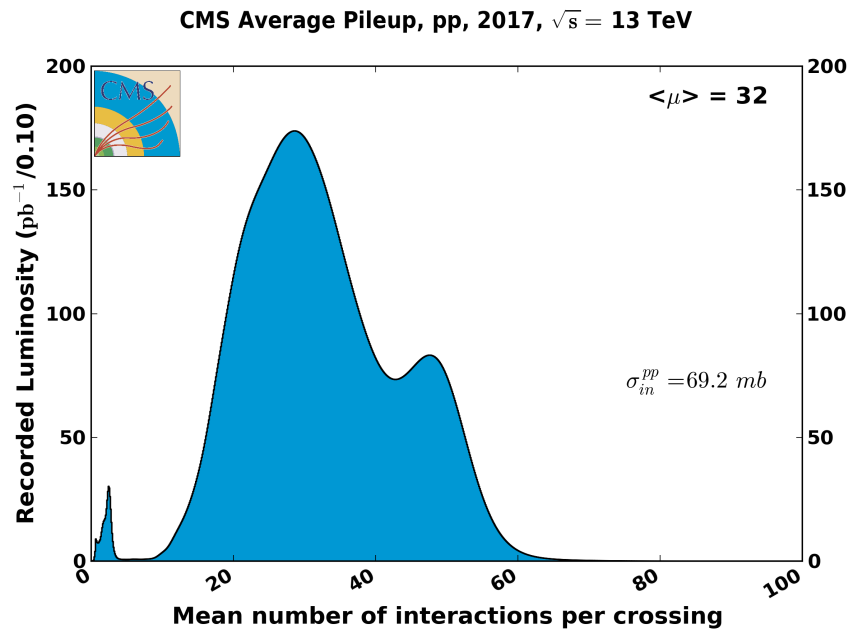


Fig. 6.4: Pileup distribution for 2017.

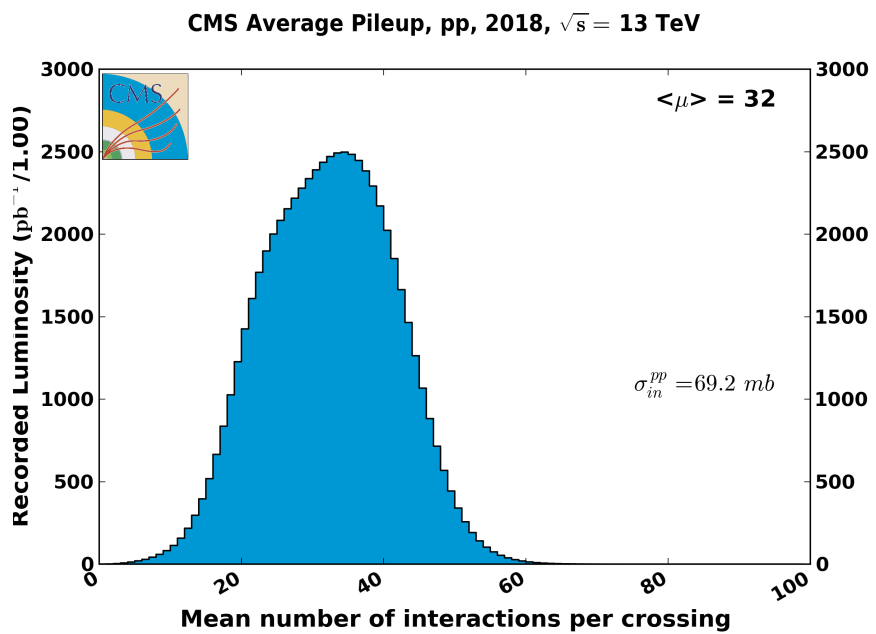


Fig. 6.5: Pileup distribution for 2018.

7. DATA ANALYSIS

7.1 Overview

633 This analysis is motivated by the GGM supersymmetry breaking scenario
 634 in which the strong production of either gluinos or squarks result in a final
 635 state containing two photons, jets, and missing transverse momentum. Two
 636 example topologies are shown in Figure 7.1. In the T5gg model, each of the
 637 produced gluinos decays to a neutralino which then decays to a photon and
 638 a gravitino. Similarly, the T6gg model has each of the produced squarks
 639 decays to a neutralino which then decays to a photon and a gravitino. In
 640 both cases the gravitino escapes the CMS without detection which manifests
 641 as missing transverse momentum.

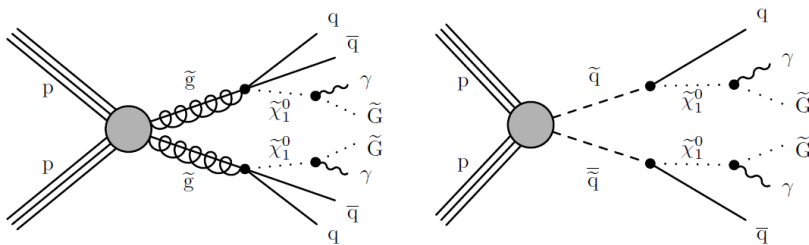


Fig. 7.1: Two examples of GGM supersymmetry breaking processes resulting in final states containing two photons and missing transverse momentum. The T5gg model (left) shows gluinos produced from $p - p$ collisions which subsequently result in two neutralinos, each decaying to a photon and a gravitino. The T6gg model (right) shows squarks produced from $p - p$ collisions following a similar decay chain.

642

7.2 Data

643 This analysis was performed using 137 fb^{-1} of data collected from the CMS
644 detector during the time period commonly referred to as Run 2 which spans
645 from 2016 to 2018. The complete list of the datasets used can be found in
646 Table 7.1. The JSON files used to identify events passing all of the CMS
647 offline data quality monitoring requirements are:

648 Cert_271036_284044_13TeV_23Sep2016ReReco_Collisions16_JSON.txt
649 Cert_294927_306462_13TeV_EOY2017ReReco_Collisions17_JSON_v1.txt
650 Cert_314472_325175_13TeV_PromptReco_Collisions18_JSON.txt

Tab. 7.1: Data Samples

/DoubleEG/Run2016B-17July2018-ver2-v1
/DoubleEG/Run2016C-17July2018-v1
/DoubleEG/Run2016D-17July2018-v1
/DoubleEG/Run2016E-17July2018-v1
/DoubleEG/Run2016F-17July2018-v1
/DoubleEG/Run2016G-17July2018-v1
/DoubleEG/Run2016H-17July2018-v1
/DoubleEG/Run2017B-31Mar2018-v1
/DoubleEG/Run2017C-31Mar2018-v1
/DoubleEG/Run2017D-31Mar2018-v1
/DoubleEG/Run2017E-31Mar2018-v1
/DoubleEG/Run2017F-31Mar2018-v1
/EGamma/Run2018A-17Sep2018-v2
/EGamma/Run2018B-17Sep2018-v1
/EGamma/Run2018C-17Sep2018-v1
/EGamma/Run2018D-22Jan2019-v2

Tab. 7.2: Table of MC samples used.

Sample name	Purpose
GJets	Training MVA discriminate for QCD background
ZGGToNuNuGG	Prediction of irreducible $Z\gamma\gamma \rightarrow \nu\nu\gamma\gamma$ background
ZGGToLLGG	Renormalization of $Z\gamma\gamma \rightarrow \nu\nu\gamma\gamma$ background
TTJets	Testing EWK background prediction method

651 *7.3 Monte Carlo samples*

652 Monte Carlo (MC) simulation were used to validate performance of the anal-
 653 ysis on backgrounds, model background contributions, constructing a mul-
 654 tivariate discriminant, and determining signal efficiencies. The MC samples
 655 used for this analysis are listed in Table 7.2.

656 The distribution of pileup (PU) interactions produced in simulated events
 657 differs from data. Since the presence of additional PU interactions affects
 658 many aspects of reconstruction, it's important for the PU to be properly
 659 simulated. To correct for these differences between MC and data the simu-
 660 lated events are reweighted so that the PU profile in MC matches the profile
 661 in data. In MC the PU is number of simulated vertices in an event while
 662 the PU in data is calculated by the method discussed in Section 6.5.

663 *7.4 Object definitions*

664 The object candidates that are identified by the reconstruction algorithms
 665 are subject to further scrutiny in order to achieve optimal purities in the
 666 offline analysis.

667

7.4.1 Photons

668 Photons are required to have $p_T > 80$ GeV and meet the criteria prescribed
669 by loose ID cuts derived by the e/γ Physics Object Group (EGM POG).

670 The cut variables used to determine the photon ID are:

671 • H/E - The ratio of the energy deposited in the HCAL tower that is
672 directly behind the ECAL supercluster associated with the photon to
673 the energy deposited in the ECAL supercluster.

674 • $\sigma_{i\eta i\eta}$ - The log-fractional weighted width of a shower in $i\eta$ -space. This
675 variable is used to describe the shower shape or more specifically it
676 provides a measure of the spread of the shower in the η -direction. The
677 log-fractional weight is the log of the ratio of energy deposited in a
678 specific ECAL crystal versus the energy deposited in the associated
679 5×5 supercluster.

680 • Particle Flow Charged Isolation - Sum of the p_T of charged hadrons
681 associated with the primary vertex within a cone of $0.02 < \Delta R < 0.3$
682 of the supercluster.

683 • Particle Flow Neutral Isolation - Sum of the p_T of neutral hadrons
684 associated with the primary vertex within a cone of $\Delta R < 0.3$ of the
685 supercluster.

686 • Particle Flow Photon Isolation - Sum of the p_T of photons within a
687 cone of $\Delta R < 0.3$ of the supercluster.

688 All of the isolation variables listed above are corrected in order to remove

689 pileup as described in Section 6.5. Table 7.3 gives a summary of the pileup-
 690 corrected requirements for a loose ID photon. The loose ID working point
 691 has an efficiency (background rejection) of 90.08% (86.25%) in the barrel
 692 and 90.65% (76.72%) in the end caps. In addition to the p_T and loose ID
 693 requirements, a photon must also pass a pixel seed veto (PSV). This means
 694 that there is no pixel seed in the tracker matched to the photon.

Tab. 7.3: Summary of loose ID photons cuts

Variable	Cut Value (Barrel)	Cut Value (Endcap)
H/E	0.04596	0.0590
$\sigma_{inj\eta}$	0.0106	0.0272
Charged Iso	1.694	2.089
Neutral Iso	$24.032 + 0.01512 p_{T\gamma} + 2.259 \times 10^{-5} p_{T\gamma}^2$	$19.722 + 0.0117 p_{T\gamma} + 2.3 \times 10^{-5} p_{T\gamma}^2$
Photon Iso	$2.876 + 0.004017 p_{T\gamma}$	$4.162 + 0.0037 p_{T\gamma}$

Photon ID efficiencies differ between data and MC, so when using a photon ID in MC samples we scale them by a "scale factor" (SF) in order to replicate detector efficiencies for that that particular ID. The loose photon ID efficiency is measured using the tag-and-probe method on $Z \rightarrow ee$ events in both data and MC. The probe is chosen to be one of the electrons while the other electron is used as the tag. The ratio of how many probes pass the loose photon ID requirements and the total number of tag and probe pairs gives the efficiency ϵ for the loose photon ID. We then define the SF as the data efficiency divided by the efficiency in MC or $SF = \frac{\epsilon_{data}}{\epsilon_{MC}}$. Applying the SF to MC events essentially removes the MC efficiency and replaces it with the real detector efficiency to give

$$N_{obs} = N_{gen} \cdot \epsilon_{MC} \cdot SF = N_{gen} \cdot \epsilon_{MC} \cdot \frac{\epsilon_{data}}{\epsilon_{MC}} = N_{gen} \cdot \epsilon_{data}. \quad (7.1)$$

695 Since this analysis requires two loose ID photons, the scale factor SF is
 696 given by the product of scale factors for each of the two loose photons,
 697 $SF = SF_{\gamma 1} \cdot SF_{\gamma 2}$. The scale factors for each year are shown in Figures 7.2,
 7.3, and 7.4 in bins of photon p_T and η [17].

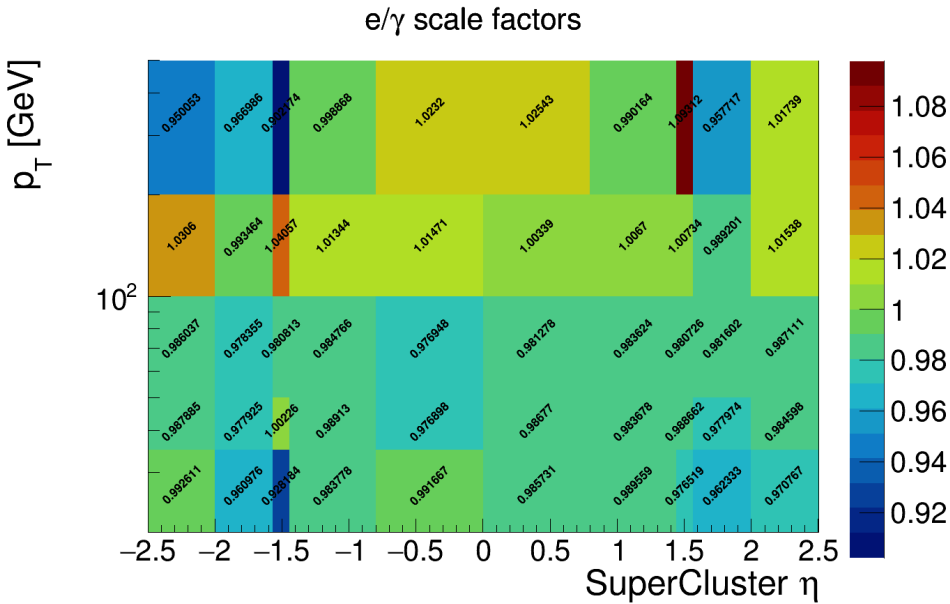


Fig. 7.2: The loose photon ID scale factors for 2016 in bins of photon p_T and η

698

699

7.4.2 Electrons

700 As mentioned earlier, the clustering algorithm doesn't differentiate between
 701 showers from photons and those from electrons. In this analysis an electron
 702 is defined as an object that passes all of the photon requirements except
 703 for the PSV. Inverting the pixel seed requirement while using the same ID
 704 criteria ensures that we have orthogonal selections while minimizing the
 705 bias potentially introduced by using control regions with electrons to model

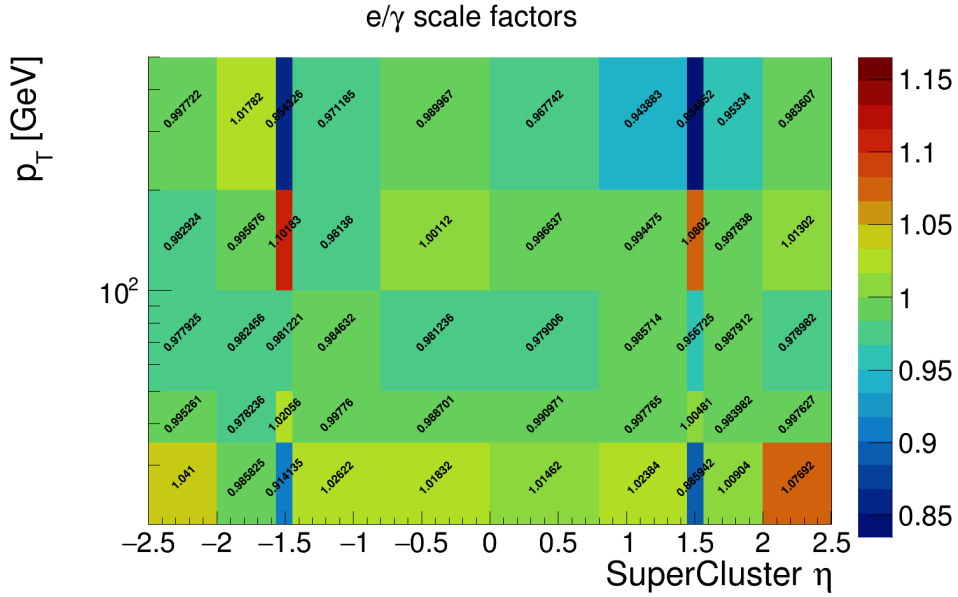


Fig. 7.3: The loose photon ID scale factors for 2017 in bins of photon p_T and η .

diphoton signal regions. This essentially allows us to group photons and electrons together to be treated as electromagnetic objects and then splitting those objects into photon and electron objects depending on whether or not there is a pixel seed associated with it.

7.4.3 Muons

Muons are required to have $p_T > 30$ GeV, $|\eta| < 2.4$, and pass the medium ID requirements listed below [39]:

- Must be identified by PF algorithm as either a tracker or a global muon.
- At least 80% of the inner tracker layers traversed by a track must have recorded hits.

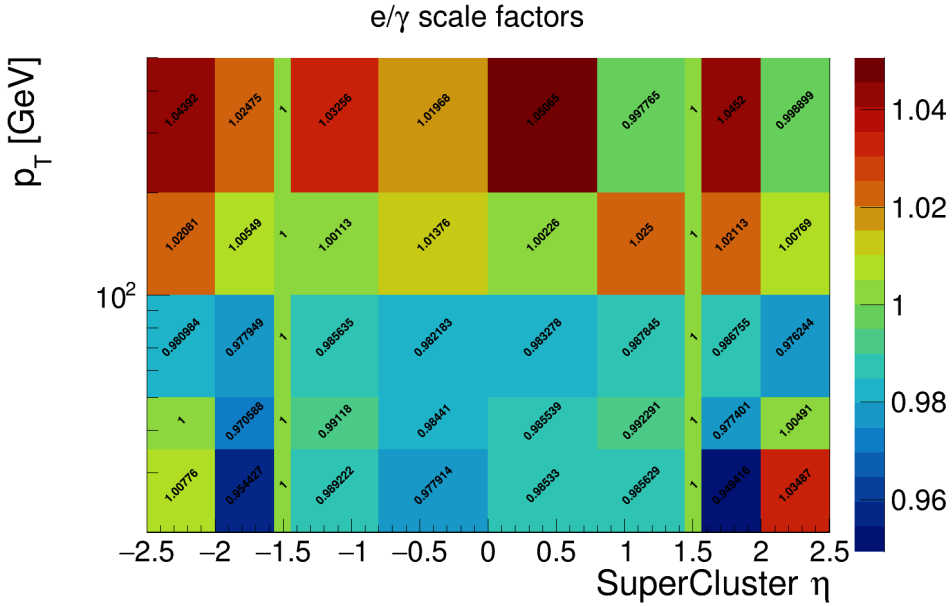


Fig. 7.4: The loose photon ID scale factors for 2018 in bins of photon p_T and η .

- 717 • If it's only reconstructed as a tracker muon, the muon segment com-
- 718 patibility must be > 0.451 .
- 719 • If it's reconstructed as both a tracker and a global muon:
 - 720 – the muon segment compatibility must be > 0.303
 - 721 – the global fit must have a goodness-of-fit per degree of freedom
 722 $(\chi^2/\text{dof}) < 3$
 - 723 – the χ^2 of the position match between standalone muon and the
 724 tracker muon must be < 12
 - 725 – the kink-finding algorithm must give a maximum χ^2 that is < 20
- 726 The types of muons (global, tracker, and standalone) are those described in
- 727 Chapter 6.3.1. The medium ID criteria results in an efficiency of $> 98\%$ for

728 muons with $p_T > 20$ GeV [15].

729 **7.4.4 Jets**

730 Jets are reconstructed using the anti- k_T algorithm described in Chapter
731 6.3.4 within a cone having radius $R = 0.4$.

732 The nature of this reconstruction also labels the previously mentioned
733 objects (photons, electrons, and muons) as jets so these need to be removed
734 from the jet collection in order to leave us with only hadronic jets. This
735 process is called "cleaning" the jets.

736 Still working on this section...

737 **7.5 Event selection**

738 Candidate events are required to pass the following requirements:

739 • Number of loose photons without a pixel seed requirement ≥ 2

740 • Number of hadronic jets ≥ 2

741 • Hard $E_T^{miss} \geq 130$ GeV

742 • Pass HLT

743 • Pass relevant event filters recommended by various POGs

744 The event filters mentioned above are designed to reject events with instru-
745 mental anomalies such as noise and beam backgrounds. These filters are:

746 • globalSuperTightHalo2016Filter

747 • HBHENoiseFilter

- 748 • HBHEIsoNoiseFilter
- 749 • eeBadScFilter
- 750 • BadChargedCandidateFilter
- 751 • BadPFMuonFilter
- 752 • CSCTightHaloFilter
- 753 • EcalDeadCellTriggerPrimitiveFilter
- 754 • ecalBadCalibReducedExtraFilter
- 755 • ecalBadCalibReducedFilter
- 756 • Good vertex filter (requiring at least one good reconstructed vertex)

757 7.6 Backgrounds

758 The sources of background in this analysis can be grouped into three cate-
759 gories. In order of decreasing contribution they are mismeasured hadronic
760 activity, electrons misidentified as photons, and standard model processes
761 having final states with neutrinos and two photons. In events with mul-
762 tiple jets, limitations on the jet energy resolution can give rise to an ap-
763 parent imbalance in p_T as is shown in Figure 7.5. Such events are usually
764 from quantum chromodynamics (QCD) processes. In these cases jets can
765 be misidentified as photons or there can be real photons being produced.
766 In both cases the result is the appearance of two photons accompanied by
767 E_T^{miss} which mimics our signal. Given the large cross-section for QCD, this

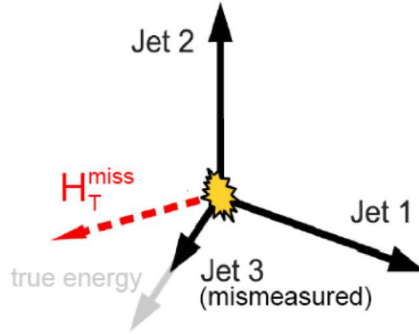


Fig. 7.5: Mismeasurement of Jet3 results in an imbalance in the events transverse momentum.

is the most significant background in this analysis. The next background, resulting from the misidentification of electrons as photons, comes from electroweak (EWK) processes, in particular $W\gamma$ and $W + \text{jets}$ events where $W \rightarrow e\nu$. Here the neutrino contributes real E_T^{miss} while the fake photon allows this event to fulfill the diphoton requirement. The final background is from $Z\gamma\gamma \rightarrow \nu\nu\gamma\gamma$ events, which exactly mimic our signal, and is modeled using simulation as it is irreducible.

7.6.1 Instrumental background

The instrumental background is the contribution from events with spurious E_T^{miss} due to mismeasured hadronic activity. The vast majority of interactions produced from proton-proton collisions at the LHC are hadronically rich QCD events. Aside from some very rare final states with heavy-flavor jets, these events do not include neutrinos, which are the only stable particles in the SM that pass through the CMS detector unobserved, and therefore exhibit little or no E_T^{miss} at the parton level. However, the measurements of

final-state particles are made using the tracker and calorimeters which have finite energy and momentum resolution. These limitations propagate into the calculation of E_T^{miss} leading to an inequality between the real, parton level E_T^{miss} in an event and the measured E_T^{miss} . Since most of this background is comprised of QCD events, it is commonly referred to as the "QCD background" and those terms are used interchangeably in this thesis. Modeling of this background was done using the Rebalance and Smear technique while a multivariate discriminant was constructed to improve the efficiency of identifying events with fake E_T^{miss} .

792 *Rebalance and Smear*

793 To estimate the QCD background, the Rebalance and Smear method is used.
794 The first step in this method is to *rebalance* events such that the E_T^{miss} is
795 removed from the event to create a set of seed event. In the second step all
796 of the jets are *smeared* with the full jet response function, which is obtained
797 from the jet response discussed in Section 6.3.4. This creates a set of seed
798 events which are used in the second step to *smear* all of the jets with the full
799 jet response function to create events that model the detector response to
800 multi-jet final states. Figure This method has been developed in the context
801 of QCD background estimation for several previous SUSY searches in the
802 all-hadronic channel [27], [37]. It has been developed here to accommodate
803 the presence of photons and other particles in the event who's energy is
804 measured more accurately than that of jets. This was done by fixing the
805 4-vectors of all of these particles during both the rebalance and smear steps
806 so that only the jet energies are allowed to float in the maximization.

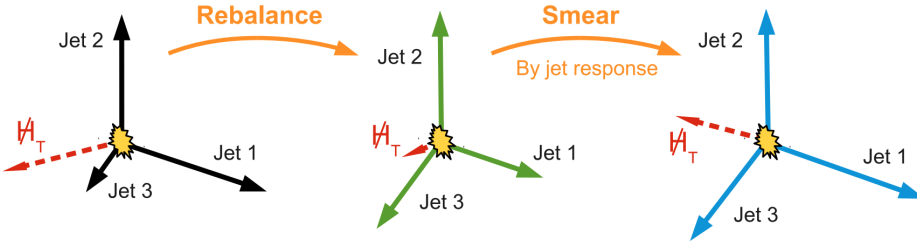


Fig. 7.6: Summary of the steps in the Rebalance and Smear method. The diagram shown here is for an all-hadronic final state and therefore uses hadronic missing transverse energy H_T which is synonymous with E_T^{miss} in this case[27].

807 The rebalancing in the first step is performed based on a kinematic
 808 fit [23], which is a least-square fit of the jet energies in the event while
 809 taking into account the jet response function. When performing the fit,
 810 it is assumed that in each event the kinematic constraints of conservation
 811 momentum are fulfilled, i.e. the total \vec{p}_T in the event is balanced. Figure 7.7
 812 shows a comparison of the jet energy response $\mathcal{R} = \frac{\vec{p}_{T,gen}}{\vec{p}_T}$ between leading jets
 813 in QCD MC events having $E_T^{miss} > 120$ GeV before and after rebalancing
 814 of the event. We see that rebalancing has the effect of improving the jet
 815 energy resolution, which is the width of this distribution as discussed in
 816 6.3.4, and also recovering some of the energy that was lost in the original
 817 jet reconstruction.

818 In the next step, the seed events obtained through rebalancing are smeared
 819 in order to simulate the expected detector-level measurement of each jet.
 820 The smearing is done by scaling the p_T of each jet by a random factor
 821 sampled from the full pre-rebalanced jet response distribution described in
 822 Section 6.3.4. The smear step was performed 50 times on each seed event
 823 in order to probe more of the response distribution and improve prediction

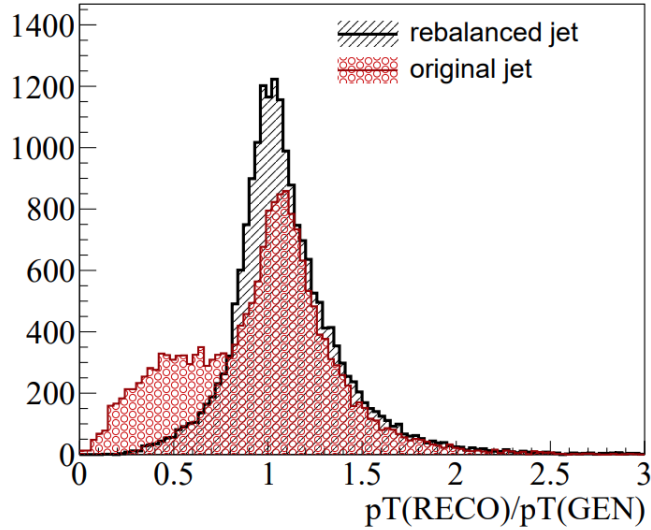


Fig. 7.7: Energy response for the leading jet in QCD MC events with $E_T^{miss} > 120$ GeV before and after being rebalanced. The original jet collection is shown shaded in red while the rebalanced collection is shaded in black. The jet energy response is defined as the ratio of the reconstructed jet p_T and the generator-level jet p_T as described in Section 6.3.4. Rebalancing improves the jet energy resolution and recovers some of the energy that was lost in original reconstruction of the jet.

824 stability by decreasing the effect of statistical fluctuations.

825 The result of this process is that we are able to take events from real
 826 data, rebalance them to closer to truth-level, and then use those rebalanced
 827 events as seeds to generate multiple detector-level events. This method has
 828 been proven effective in all-hadronic final states, but in this case it is being
 829 used in the presence of two photons also in the final state. As the photon p_T
 830 values in the seed events are not smeared like the jets to create these new
 831 detector-level events, there is a danger that the photon p_T spectrum could
 832 be distorted. This was checked using simulated di-photon events from QCD
 833 MC requiring two loose ID photons and Hard $E_T^{miss} > 120$ GeV. The results

in Figures 7.8 and 7.9 show that there is no significant distortion of either the leading or next-to-leading photon p_T spectra.

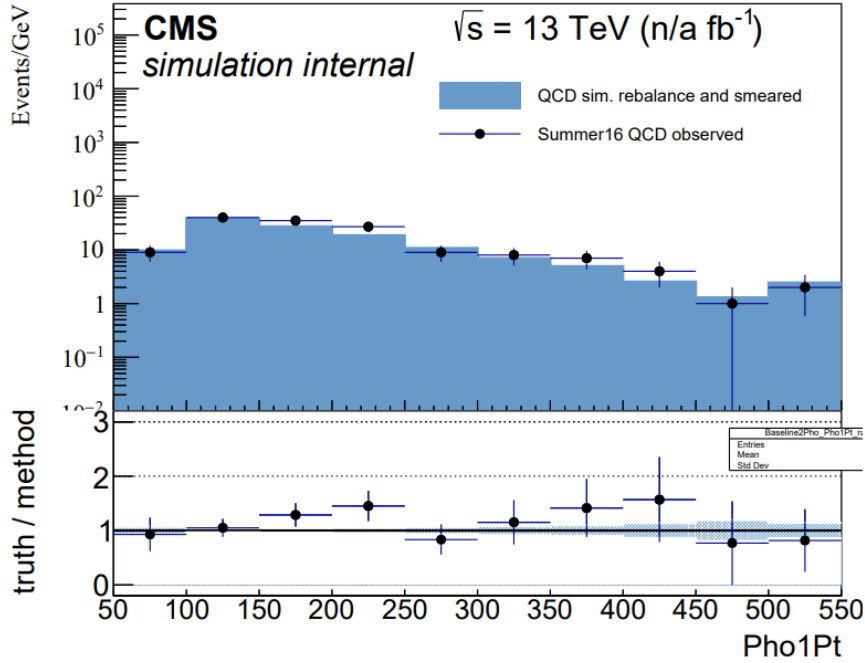


Fig. 7.8: This shows a comparison of the p_T distribution for the leading photons in di-photon QCD MC events before and after being Ralanced and Smeared. These events were required to have two loose ID photons and Hard $E_T^{miss} > 120$ GeV. The data points are taken directly from the QCD simulation while the blue shaded area shows the distribution after application of Rebalance and Smear. We see here that the Rebalance and Smear method causes no significant distortions to the leading photon p_T spectrum in di-photon events.

836

Multivariate discriminant

837 A boosted decision tree (BDT) was used to develop a discriminating vari-
 838 able for identifying events with real E_T^{miss} . A decision tree is a classifier
 839 with a binary tree structure that recursively partitions data or samples into
 840 classifications of either signal or background. Figure 7.10 shows an example

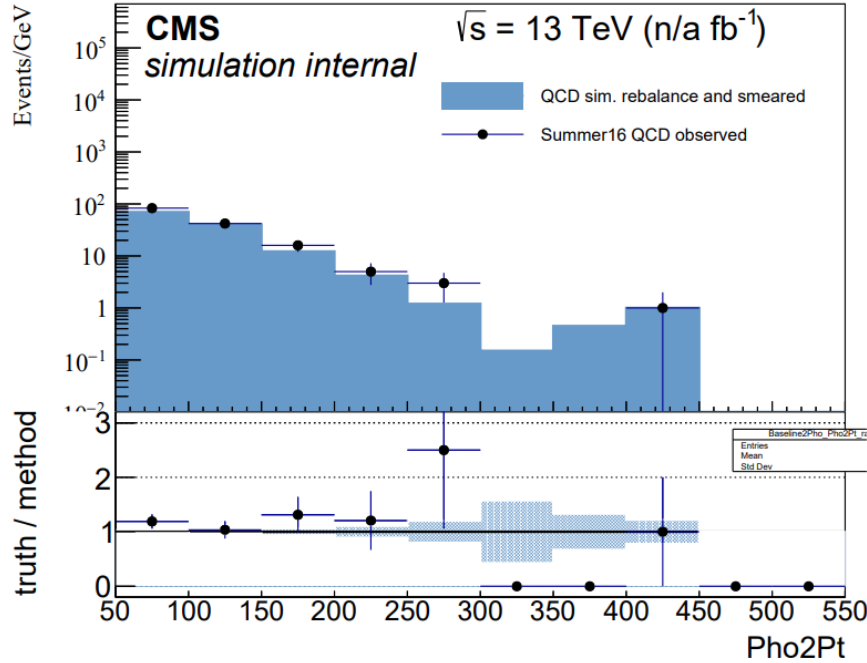


Fig. 7.9: This shows a comparison of the p_T distribution for the next-to-leading photons in di-photon QCD MC events before and after being Rebalanced and Smeared. These events were required to have two loose ID photons and Hard $E_T^{miss} > 120$ GeV. The data points are taken directly from the QCD simulation while the blue shaded area shows the distribution after application of Rebalance and Smear. We see here that the Rebalance and Smear method causes no significant distortions to the next-to-leading photon p_T spectrum in di-photon events.

841 schematic of a single decision tree. Each splitting of the data takes place at
842 a *node*. Each node uses a single input variable to make a decision regarding
843 classification. This process begins at a *root* node and continues until the
844 final node in the tree is reached, which is referred to as a *leaf* node. The
845 number of layers of nodes is what we call the *depth* of a tree. *Training* is
846 the process of building or growing a tree. The training process begins by
847 setting an initial splitting criteria at a root node. The root node splits the

848 training data, which consists a set of background samples and a set of signal
 849 samples, into two subsets which each go to different node where this same
 850 process is repeated until the entire tree is built. The splitting criteria at
 851 each node is determined by finding which variable and cut value on said
 852 variable results in the best separation between signal and background. The
 853 amount of separation is quantified by a separation index known as the Gini
 854 Index, which is defined by $p(1 - p)$ where p is the purity of the resulting
 855 subsets. Once the entire tree is built, the leaf nodes are identified as either
 856 signal or background depending on whether the majority of the events they
 857 contain are from the signal or background training samples.

Extending this process to many trees, which we call a *forest*, allows us to enhance the classification performance by applying a *boosting* algorithm. For this analysis the AdaBoost (adaptive boost) algorithm was used. The AdaBoost algorithm gives added weight (boost weight) to events in the training sample that misidentified as either signal or background and then uses these reweighted events as the training sample for growing the next tree.

The boost weight is given as

$$\alpha = \frac{1 - \epsilon}{\epsilon} \quad (7.2)$$

where ϵ is the misclassification rate of the previous tree. The same α is applied to every event that was misclassified in the training sample. The boosted classification, or BDT score, is then given by

$$BDT_{score}(x) = \frac{1}{N_{trees}} \cdot \sum_i^{N_{trees}} \ln(\alpha_i) \cdot h_i(x) \quad (7.3)$$

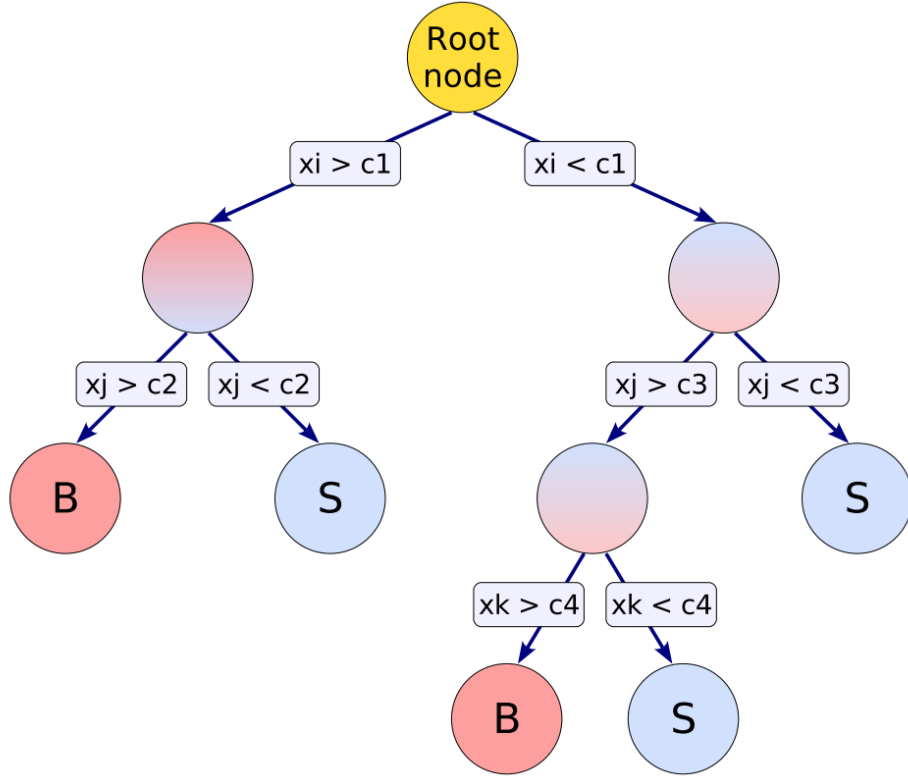


Fig. 7.10: This is a schematic view of a decision tree. Reprint from [31]

858 where x is the set of input variables, and $h(x) = 1$ if the event falls into a
 859 signal leaf and -1 if it is in a background leaf. The result is a BDT_{score} that
 860 ranges between -1 (background-like) and +1 (signal-like).

861 Training and testing of the BDT was performed in ROOT using the
 862 Toolkit for MultiVariate Analysis (TMVA). The signal samples used for both
 863 training and testing are comprised of a combination of different mass points
 864 from the T5Wg and T6Wg MC samples. The mass points used were chosen
 865 to represent a wide range of mass differences between gluino/squark and neu-
 866 tralino masses. This was done by using the bands of gluino/squark masses

867 shown in Figure 7.11. In order to minimize any bias in the BDT response
868 to model-dependent parameters like the difference between gluino/squark
869 and neutralino masses, the training events used from each mass point were
870 weighted by a factor of one over the number events generated for that par-
871 ticular model. This ensures that each mass point in the mass band is equally
872 represented in the training sample for the BDT. The location of the mass
873 bands were chosen to be near the edge of the exclusion region to target the
874 phase space not yet ruled out by previous analyses. The background sam-
875 ples use for training and testing of the BDT were GJets MC samples that
876 had been Rebalanced and Smeared to increase statistics. These simulate
877 Standard Model processes resulting in final states containing jets and at
878 least one photon which is the source of the fake E_T^{miss} background. The full
879 list of MC samples used in the BDT training can be seen in Table 7.4. As
880 mentioned in Section 4.3.1, there was a substantial upgrade to the pixel de-
881 tector in between 2016 and 2017 which separates Run 2 into Phase 0 (2016)
882 and Phase 1 (2017 and 2018). In order to remove any effects on the BDT
883 due to different detector response before and after the upgrade, a separate
884 BDT was trained and applied for each of these two phases. For events from
885 these samples to be included in the training or testing of the BDT, they
886 were required to have

- 887 • At least two photons without associated pixel seeds as described in
888 Section 7.4.1.
- 889 • At least one of those photons is in the EB ($|\eta| < 1.44$)
- 890 • Both photons within the range of tracker acceptance ($|\eta| < 2.4$)

- 891 • At least two jets as described in Section 7.4.4.
- 892 • Hard $E_T^{miss} > 130$ GeV

Tab. 7.4: List of MC samples used for training and testing BDT

Signal Samples
SMS-T5Wg_TuneCUETP8M1_13TeV-madgraphMLM-pythia8
SMS-T6Wg_TuneCUETP8M1_13TeV-madgraphMLM-pythia8
Background Sample
GJets_DR-0p4_HT-100To200_TuneCUETP8M1_13TeV-madgraphMLM-pythia8
GJets_DR-0p4_HT-200To400_TuneCUETP8M1_13TeV-madgraphMLM-pythia8
GJets_DR-0p4_HT-400To600_TuneCUETP8M1_13TeV-madgraphMLM-pythia8
GJets_DR-0p4_HT-600ToInf_TuneCUETP8M1_13TeV-madgraphMLM-pythia8

893 The input variables used by the BDT are listed below. All energy and
 894 momentum variables were normalized to the scalar sum of all of the p_T in
 895 the event $S_T = \sum_{\gamma, jets} |\vec{p}_T|$ in order to encourage the BDT to focus more
 896 on how the energy and momentum was distributed in an event rather than
 897 simply the scale of the energy or momentum. Distributions of the input
 898 variables for both signal and background are shown in Figure 7.12, 7.13,
 899 and 7.14.

- 900 • $S_{T_{jets}} = \sum_{jets} |\vec{p}_T|$
- 901 • $p_{T_{jets}} = \sum_{jets} \vec{p}_T$
- 902 • $p_{T_{\gamma\gamma}} = \vec{p}_{T_{\gamma_1}} + \vec{p}_{T_{\gamma_2}}$
- 903 • $HardE_T^{miss} = | - \sum_i p_{T_i} \cdot \Theta(30 - p_{T_i}) |$
- 904 • $\Delta\Phi_{\gamma\gamma} = \Delta\Phi(\vec{p}_{T_{\gamma_1}}, \vec{p}_{T_{\gamma_2}})$
- 905 • $\Delta\Phi_{min} = min[\Delta\Phi(\vec{p}_{T_{HardE_T^{miss}}}, \vec{p}_{T_{jet_i}})]$

-
- 906 • $\Delta\Phi_1 = \Delta\Phi(\vec{p}_{T_{HardE_T^{miss}}}, \vec{p}_{T_{jet_1}})$
 907 • $\Delta\Phi_2 = \Delta\Phi(\vec{p}_{T_{HardE_T^{miss}}}, \vec{p}_{T_{jet_2}})$
 908 • $\Delta\Phi_{\gamma\gamma, HardE_T^{miss}} = \Delta\Phi(\vec{p}_{T_{HardE_T^{miss}}}, \vec{p}_{T_{\gamma\gamma}})$
 909 • $\Delta R_{jet_n\gamma_m} = \Delta R(jet_n, \gamma_m)$ for $n = 1, 2$ and $m = 1, 2$

910 Events in both the signal and background samples are randomly split
 911 into either a test or training categories. A substantial difference between the
 912 test and training distributions of the BDT response implies that the BDT
 913 is not drawing reliable conclusions as to whether an event is signal-like or
 914 background-like. A grid search over different combinations of hyperparamete-
 915 rs (the maximum depth of a tree and the number of trees) was performed
 916 to maximize separation between the signal and background BDT response
 917 distributions while maintaining good agreement between the training and
 918 test samples. Using 200 trees with a maximum depth of 4 was found to be
 919 the optimal choice as increasing either or both of those parameters resulted
 920 in over-training with minimal gains in separation of signal and background.
 921 The comparison of BDT scores between signal and background events is
 922 shown in Figures 7.19 and 7.20 for the Phase 0 and Phase 1 BDTs respec-
 923 tively. Comparisons of training and test samples for Phase 0 are shown in
 924 Figures 7.15 (background) and 7.16 (signal). The comparisons for Phase 1
 925 are shown in Figures 7.17 (background) and 7.18 (signal). The training and
 926 test samples comparisons don't show any significant deviations while there
 927 is good separation between signal and background BDT responses.

928 Using the BDT we created one control region (low BDT score) and two

929 signal regions (medium and high BDT scores) by defining two BDT score
930 thresholds. The low threshold corresponds to the minimum BDT score with
931 at least 90% acceptance of every signal model or mass point in signal MC
932 samples. Figures 7.21 and 7.22 show the BDT cuts that resulted in 90%
933 acceptance at each mass point for the T5gg and T6gg models respectively.
934 In both models the value of this BDT cut is always greater than -0.13 so
935 this was chosen as the value separating the low-BDT control region and
936 the medium-BDT signal region. The threshold for the high-BDT region is
937 chosen such that 90% of the fake E_T^{miss} background from the GJets MC
938 is excluded. The BDT response for Rebalanced and Smeared events in this
939 sample for each year is shown in Figures 7.23, 7.24, and 7.25 where over 90%
940 of the events have a score less than 0.03. This puts the threshold for the
941 high-BDT signal region at a BDT score of 0.03. With these three regions
942 we have a very background-pure control region ($BDT \leq -0.13$) and two
943 signal regions, one very pure in signal ($BDT > 0.03$) and one intermediate
944 ($-0.13 < BDT \leq 0.03$), which combined have at least 90% acceptance for
945 all mass points.

946

7.6.2 Electroweak background

947 The electroweak background is dominated by events with $W \rightarrow e\nu$ where
948 the electron is misidentified as a photon. Unlike the QCD background these
949 events have real E_T^{miss} due to the presence of a neutrino. The key to estimat-
950 ing this background is determining the rate at which electrons get incorrectly
951 labeled as photons in the signal region. This is done using a tag-and-probe
952 method where the tag is an electron (a loose ID photon that fails the PSV)

and the probe is categorized as either a photon or an electron. The result is an electron-electron region (ee) and an electron-photon region ($e\gamma$) that are selected from the data. As both of these regions contain $Z \rightarrow ee$ decays, fits are applied in each of the samples to the invariant mass spectra m_{ee} and $m_{e\gamma}$. The integrals of these fits are calculated over the range of the Z mass peak to give the number of events in each category, $N_{e\gamma}$ and N_{ee} . The ratio of the number of

7.6.3 Irreducible background

The irreducible $Z\gamma\gamma \rightarrow \nu\nu\gamma\gamma$ background produces two photons and has inherent E_T^{miss} via the neutrinos. There is no easy way to separate these events from our signal so it is estimated using MC simulation. The prediction of this background is given by $N_{pred} = N_{MC} \cdot R$ where R is an overall simulation-to-data normalization factor obtained by comparing $Z\gamma\gamma \rightarrow LL\gamma\gamma$ MC samples to $Z\gamma\gamma \rightarrow \mu\mu\gamma\gamma$ and $Z\gamma\gamma \rightarrow ee\gamma\gamma$ events in data. The event selection criteria, relaxed from the baseline version in order to maximize statistics, was

- 2 looseID photons with $p_T > 30$ GeV and no pixel seed
- 2 like-flavored leptons with $p_T > 30$ GeV
- 2 mediumID muons or
- 2 electrons (looseID photons with pixel seeds).

The resulting dilepton invariant mass spectra for 2016 MC and data are shown in Figure 7.26. The number of events with dilepton mass within 10 GeV of the Z boson mass is shown in Table 7.5. The ratio of data events to

975 MC events gives the normalization factor R factor which was applied to the
 976 $Z\gamma\gamma \rightarrow \nu\nu\gamma\gamma$ MC to give the background prediction for this process.

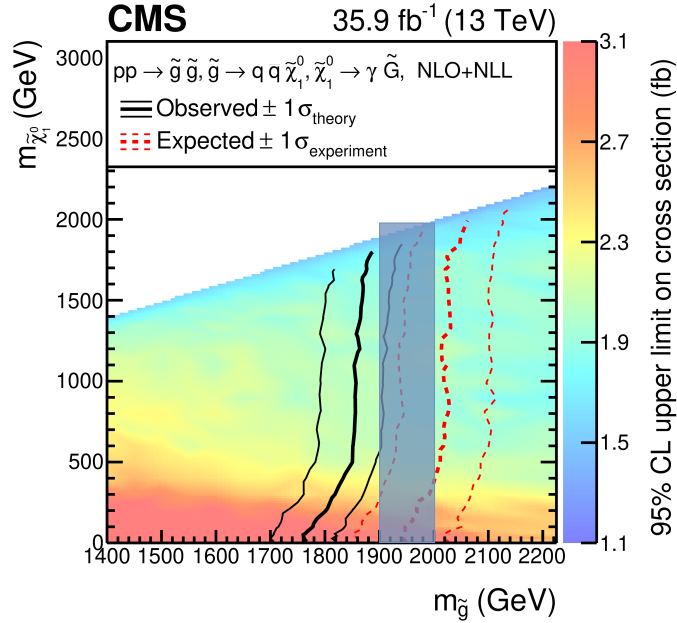
Tab. 7.5: Summary of $Z\gamma\gamma \rightarrow \nu\nu\gamma\gamma$ model validation

Year	Data Events	MC Events	$R = \frac{\text{data}}{\text{MC}}$
2016	10.0 $+4.78 -3.05$	10.54 ± 0.54	$0.95 +0.46 -0.29$
2017	-	-	-
2018	-	-	-

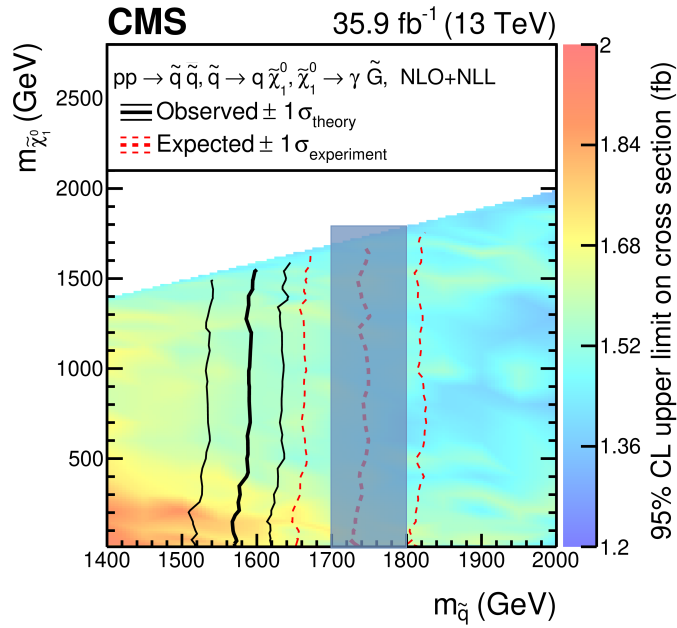
977 **7.7 Signal and control regions**

978 The background estimation methods are validated in various low-BDT data
 979 control regions.

980 The first such region is the low-BDT ee region in which the pixel seed
 981 veto requirements are inverted, resulting in events with two electrons. This
 982 region is primarily composed of $t\bar{t}$, which is a source of real E_T^{miss} , and Drell-
 983 Yan (DY) with $Z \rightarrow ee$. As the DY background is comprised of multi-jet
 984 events with two electrons (photons with inverted pixel seed requirements),
 985 this is a source of fake E_T^{miss} that is very similar yet orthogonal to our
 986 expected signal which consists of multi-jet events with two photons.



(a) Cross-section upper limits for gluino pair production



(b) Cross-section upper limits for squark pair production

Fig. 7.11: The 95% confidence level upper limits on the pair production cross sections for gluinos (7.11a) and squarks (7.11b) as a function of gluino/squark and neutralino masses as reported in [38]. The shaded vertical bands show the mass bands used in the BDT training.

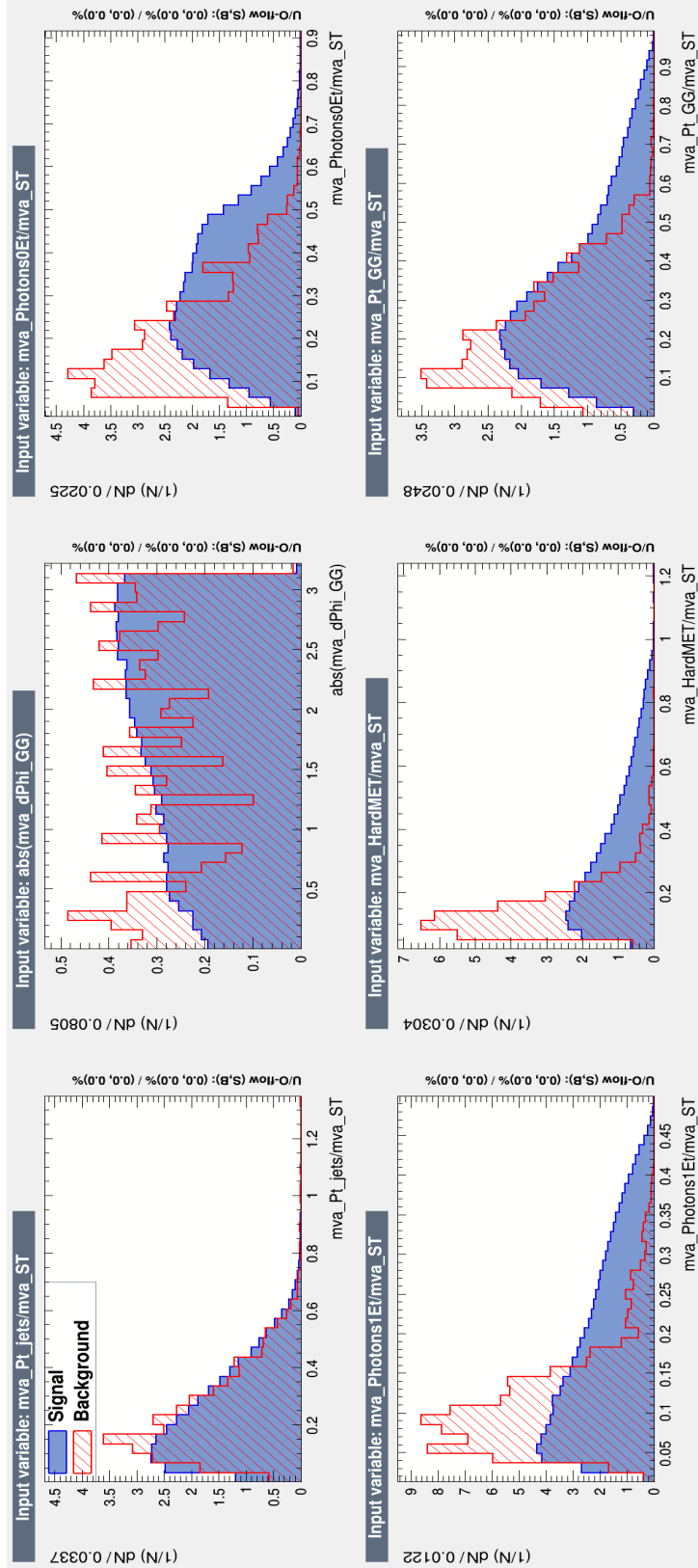


Fig. 7.12: Signal and background input variable distributions for the BDT. The red distribution represents the background while the blue is signal.

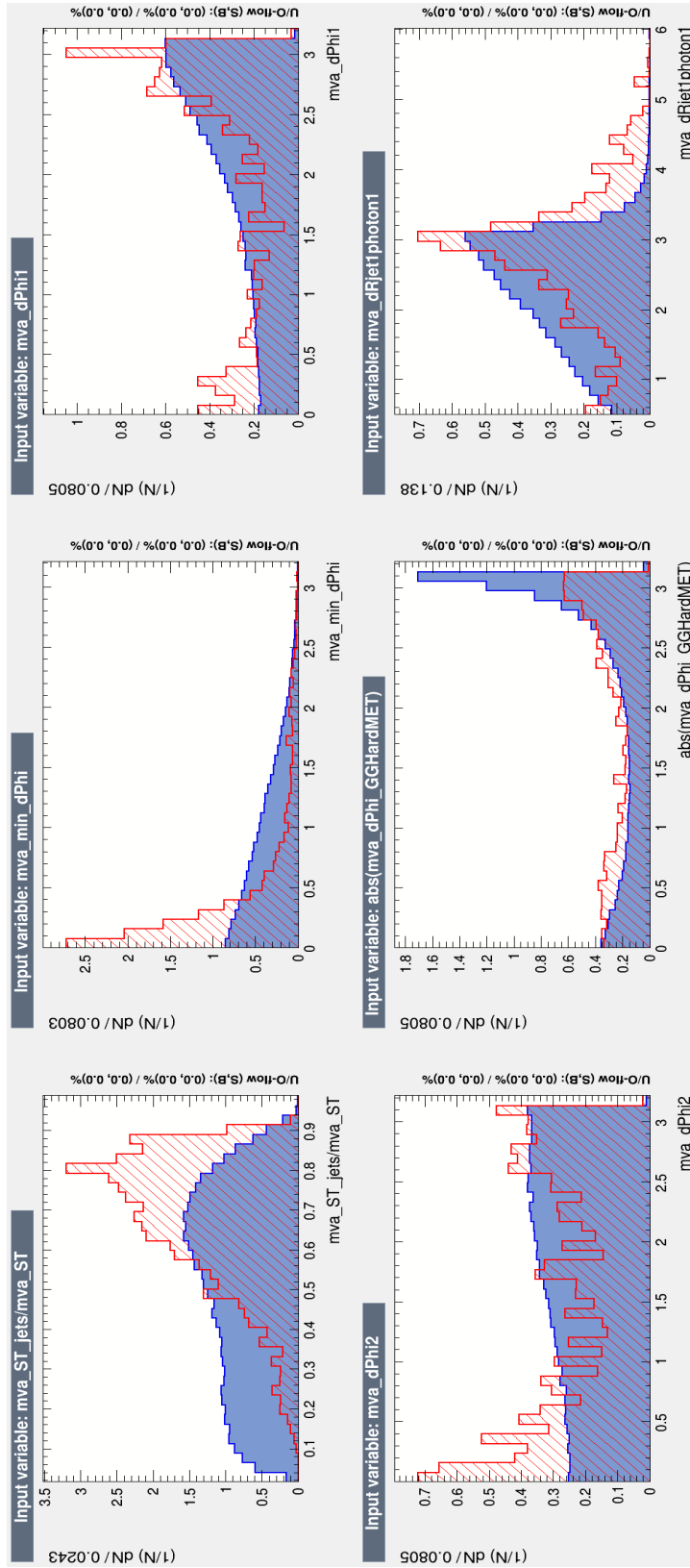


Fig. 7.13: More signal and background input variable distributions for the BDT. The red distribution represents the background while the blue is signal.

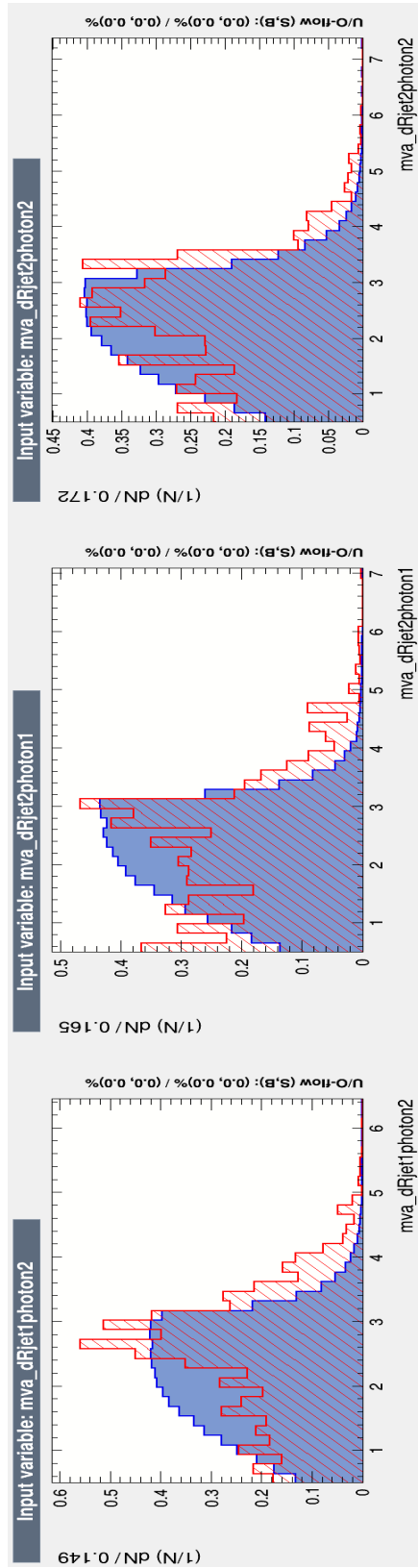


Fig. 7.14: More signal and background input variable distributions for the BDT. The red distribution represents the background while the blue is signal.

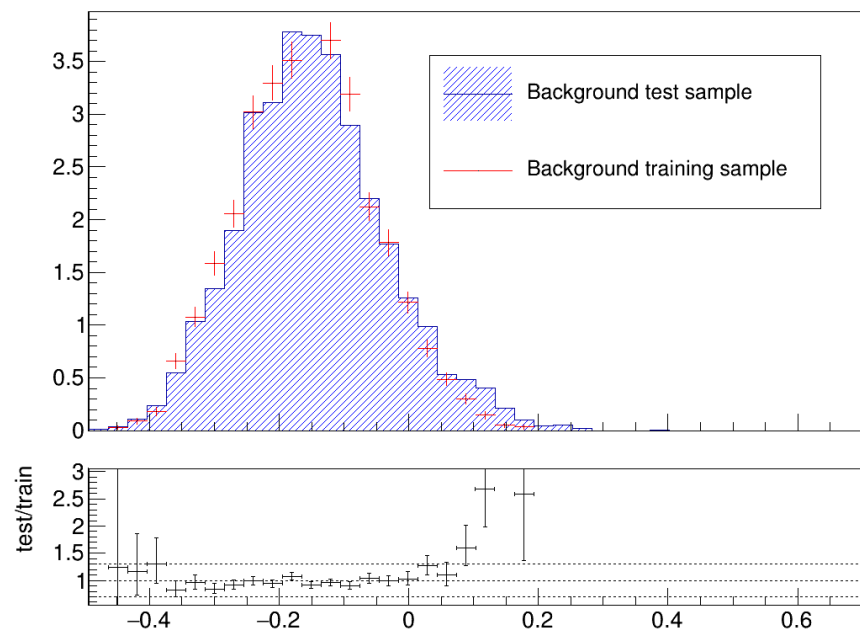


Fig. 7.15: Overtraining check for background samples in Phase 0 BDT. The BDT score distributions for the training (red) and testing (blue) samples are plotted on the same graph.

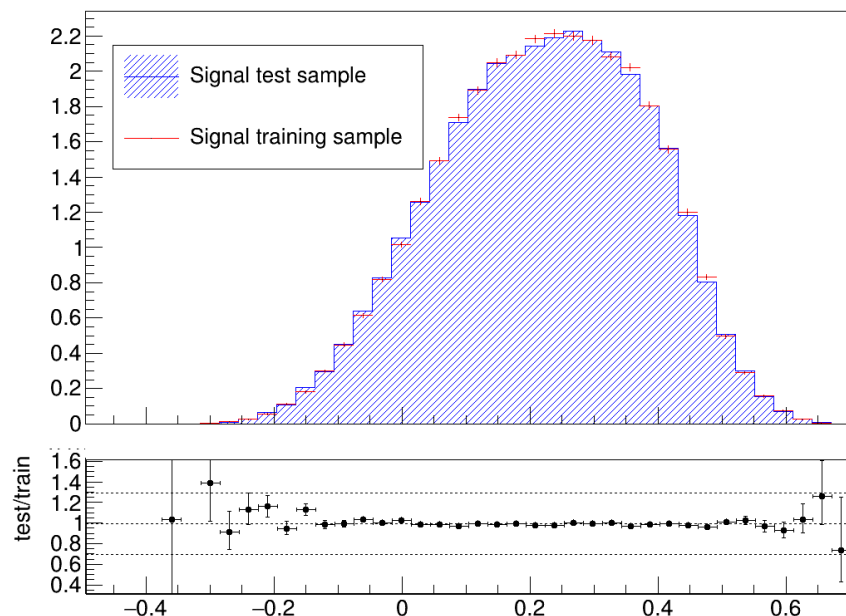


Fig. 7.16: Overtraining check for signal samples in Phase 0 BDT. The BDT score distributions for the training (red) and testing (blue) samples are plotted on the same graph.

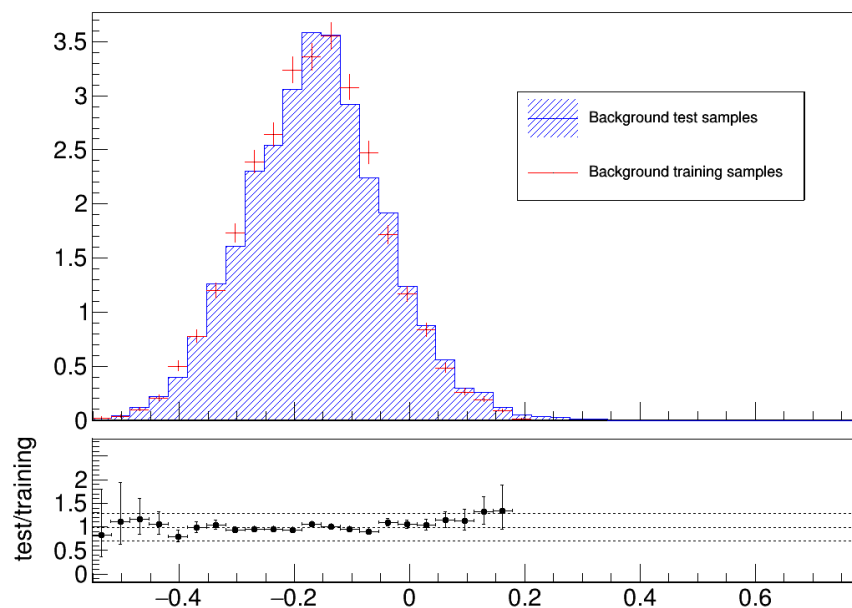


Fig. 7.17: Overtraining check for background samples in Phase 1 BDT. The BDT score distributions for the training (red) and testing (blue) samples are plotted on the same graph.

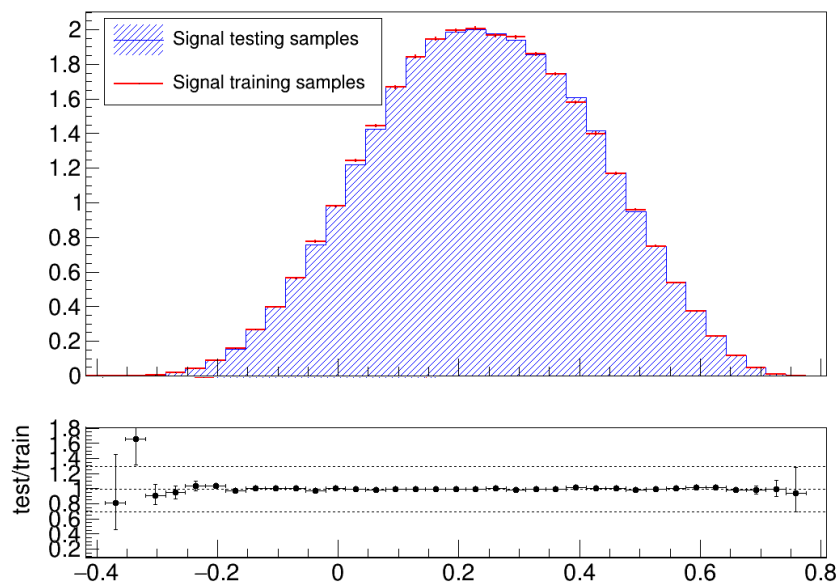


Fig. 7.18: Overtraining check for signal samples in Phase 1 BDT. The BDT score distributions for the training (red) and testing (blue) samples are plotted on the same graph.

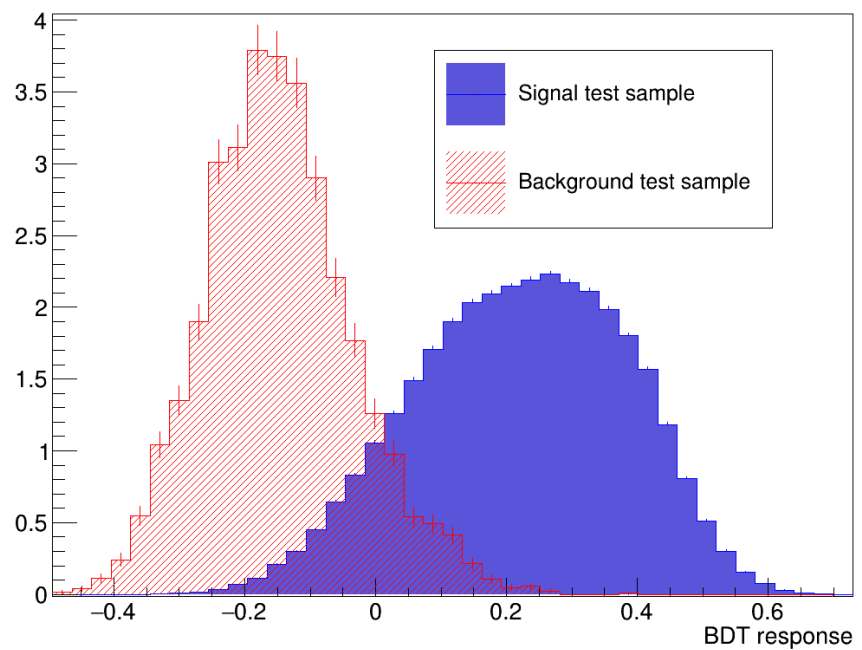


Fig. 7.19: Phase 0 BDT response for signal (blue) and background (red)

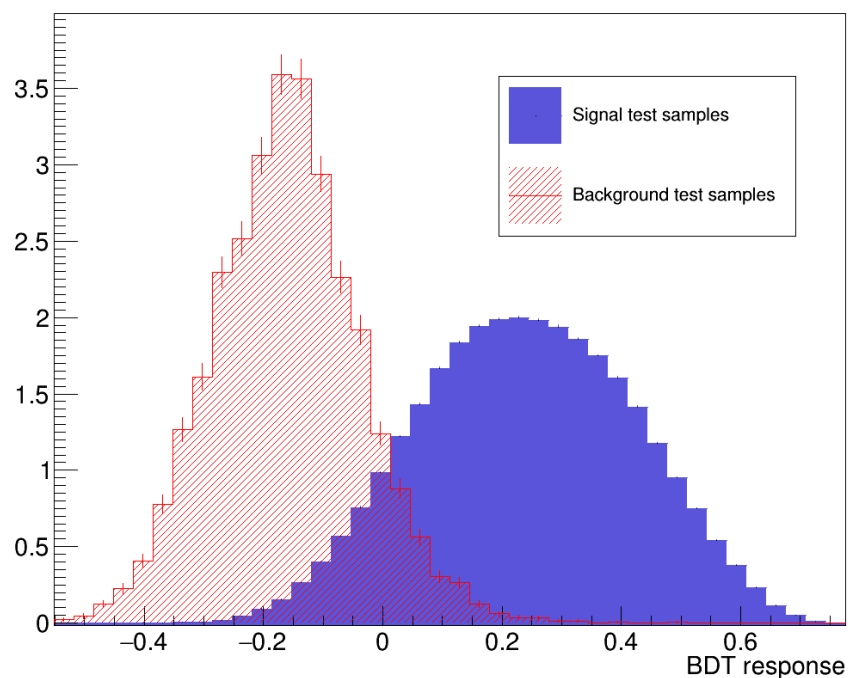


Fig. 7.20: Phase 1 BDT response for signal (blue) and background (red)

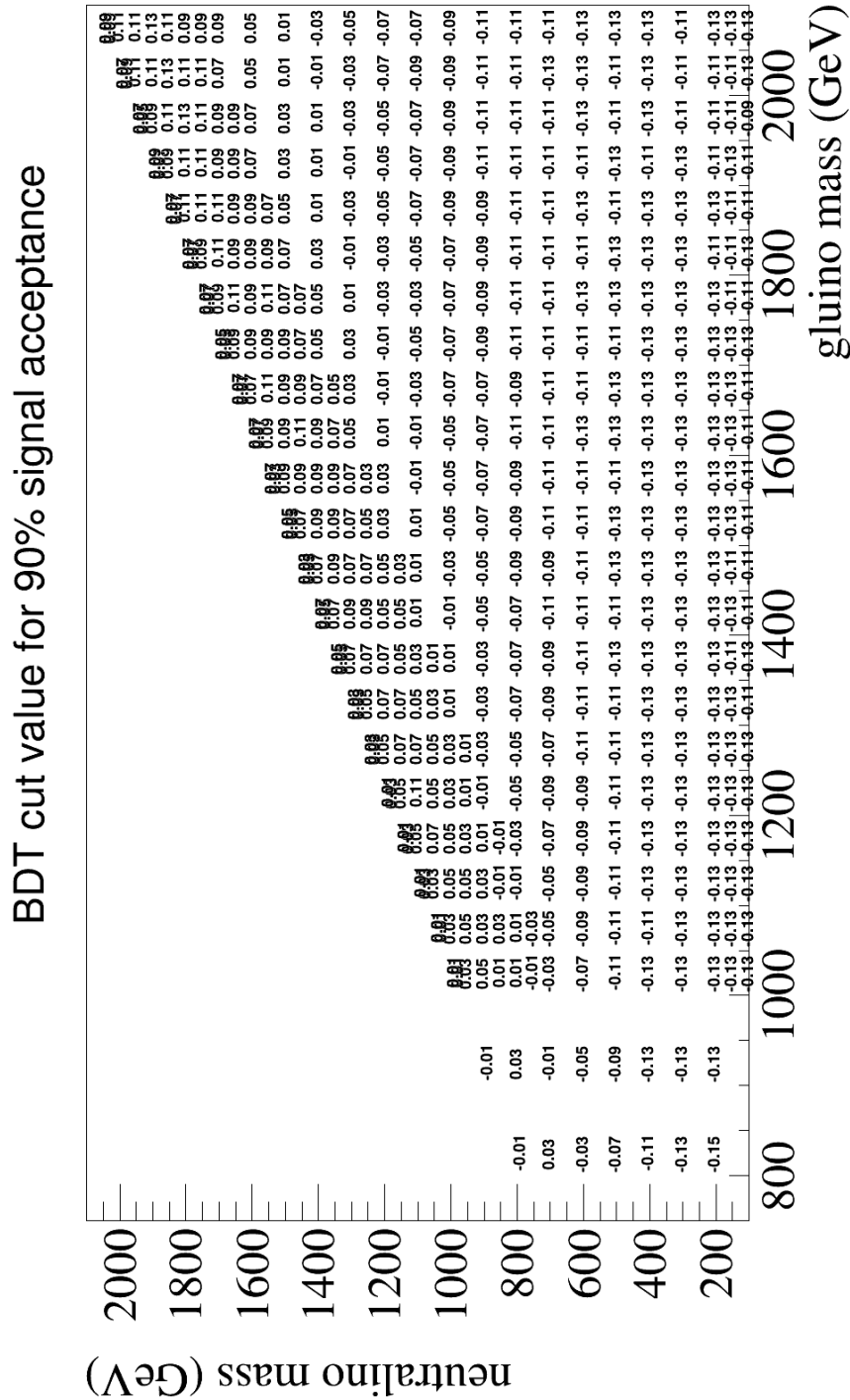


Fig. 7.21: BDT cut values on T5gg models resulting in 90% signal acceptance.

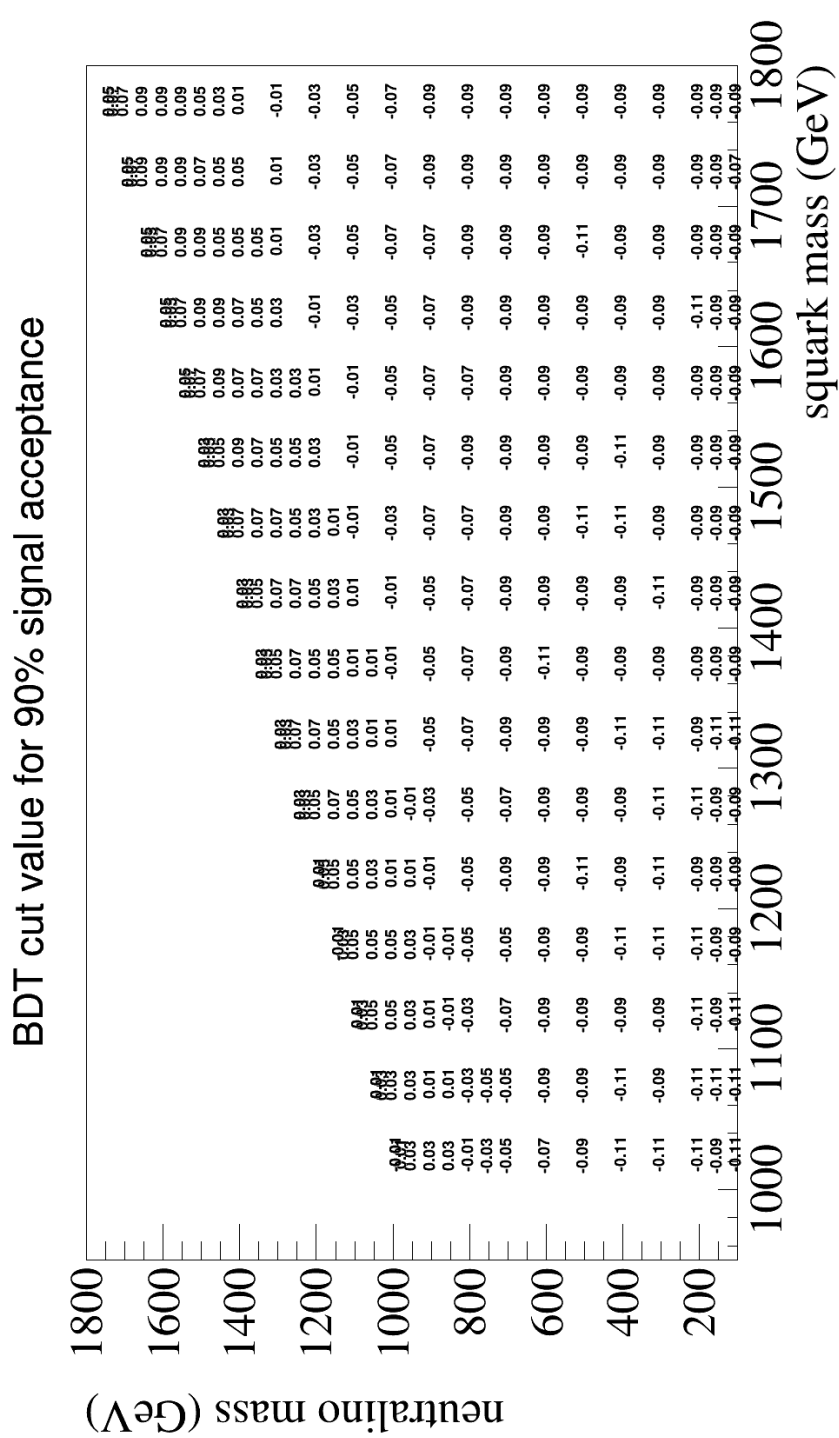


Fig. 7.22: BDT cut values on T6gg models resulting in 90% signal acceptance.

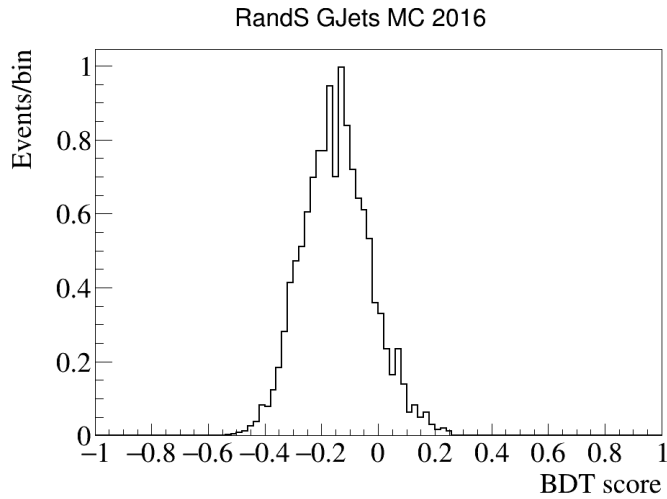


Fig. 7.23: This is the BDT score distribution for Rebalance and Smear events from the 2016 GJets MC samples. Requiring a BDT score above 0.03 removes 90% of this background.

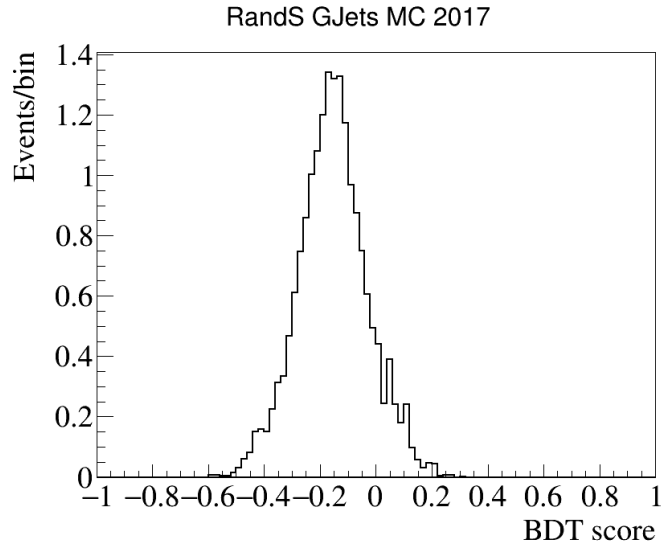


Fig. 7.24: This is the BDT score distribution for Rebalance and Smear events from the 2017 GJets MC samples. Requiring a BDT score above 0.03 removes 90% of this background.

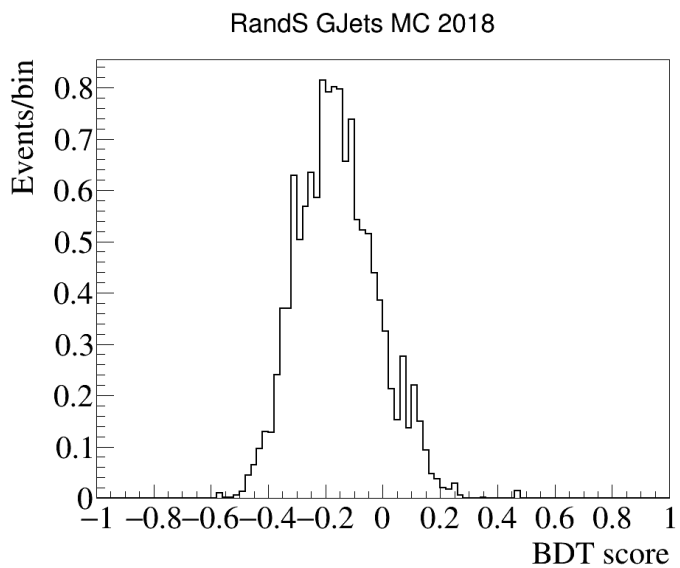


Fig. 7.25: This is the BDT score distribution for Rebalance and Smear events from the 2018 GJets MC samples. Requiring a BDT score above 0.03 removes 90% of this background.

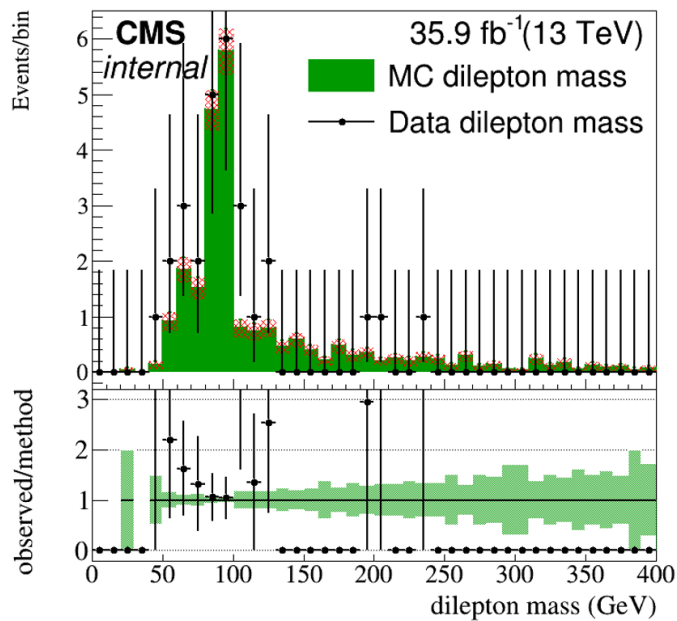


Fig. 7.26: Comparison of dilepton invariant mass spectra from ZGGToLLGG events in MC and data. Good agreement is seen in the region where the invariant mass is within 10 GeV of the Z boson mass (91 GeV).

987

8. RESULTS AND INTERPRETATIONS

988

8.1 *Observation vs Predicted*

989 This is where I'll put the tables for the observed and predicted number of
990 events in each search region bin.

991

8.2 *Simplified models*

992 The interpretation of these results uses the T5gg and T6gg simplified mod-
993 els. The T5gg simplified model gluino (\tilde{g}) pair production while the T6gg
994 model assumes squark (\tilde{q}) pair production. The lightest supersymmetric
995 particle (LSP) in both models is the gravitino \tilde{G} and the next-to-lightest
996 supersymmetric particle is the neutralino $\tilde{\chi}_1^0$. Figure 7.1 shows examples of
997 decay chains for both models.

998 Monte Carlo scans were used to evaluate the expected signal distributions
999 for these models. The scan for the T5gg model was produced in bins of
1000 gluino and neutralino masses while the T6gg scan was binned in squark and
1001 neutralino masses. `MadGraph5_aMC@NLO` was used for event generation[7]
1002 while `PYTHIA 8` was used for simulating parton showering, hadronization,
1003 and multi-parton interactions[40]. The detector response was simulated with
1004 CMS fast simulation[4]. Production cross sections were calculated next-

1005 to-leading order (NLO) plus next-to-logarithmic (NLL) accuracy [11]. For
 1006 calculations of gluino cross sections the squark was taken to be heavy and
 1007 decoupled and vice versa for squark cross section calculations. The cross
 1008 sections for gluino and squark pair production are shown in Figures 8.1 and
 1009 8.2 respectively.

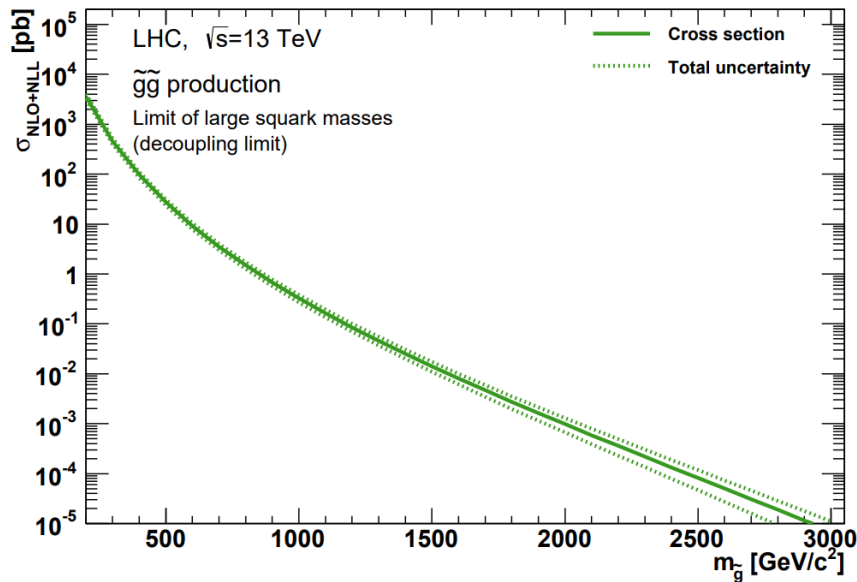


Fig. 8.1: The NLO+NLL cross section for gluino pair production as a function of gluino mass.

1010

8.3 Statistical analysis

Upper limits for the production cross section of each signal model are evaluated using the modified frequentist method, CL_s , with a profile likelihood test statistic. The uncertainties that affect the predicted signal and background yields, s and b respectively, are incorporated by introducing nuisance parameters θ . We can then express the signal and background expectations

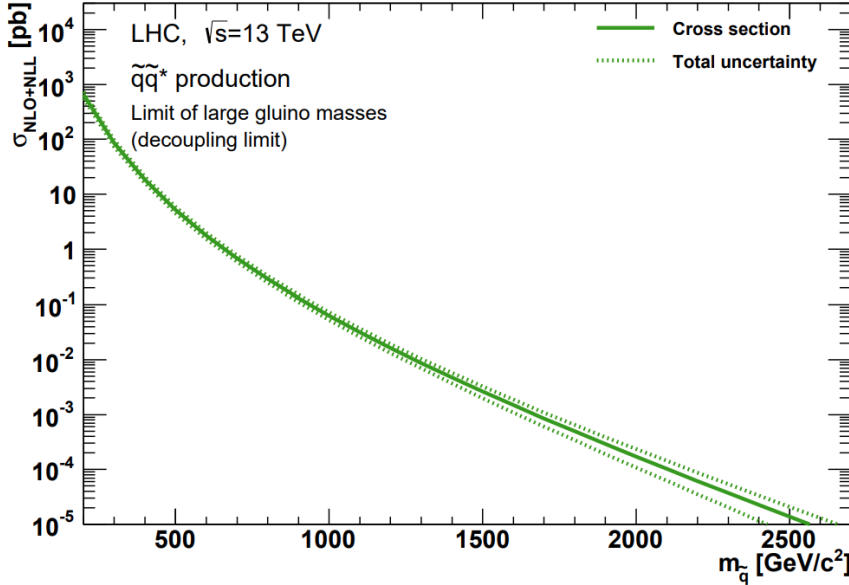


Fig. 8.2: The NLO+NLL cross section for squark pair production as a function of squark mass.

as functions of the nuisance parameters. The probability P for a given search region to contain n observed events when expecting to observe b background events and s signal events can be expressed with signal strength modifier μ and the set of nuisance parameters θ as a Poisson distribution as shown in Equation 8.1.

$$P(n|\mu, \theta) = \frac{(\mu s(\theta) + b(\theta))^n}{n!} e^{-(\mu s(\theta) + b(\theta))} \quad (8.1)$$

1011 The probability distribution $p_i(\theta)$ for each nuisance parameter θ_i depends
 1012 on the uncertainty that it represents. For statistical uncertainties the prob-
 1013 ability distribution is modeled with a gamma density distribution, while
 1014 systematic uncertainties are modeled using a log-normal density distribu-

1015 tion.

Combining all of the search regions we can make a likelihood function \mathcal{L} , which is the probability to have signal strength μ and the set of nuisance parameters θ given n_i events are observed observed in search region i .

$$\mathcal{L}(n|\mu, \theta) = \prod_i P(n_i|\mu, \theta) \prod_j p_j(\theta) \quad (8.2)$$

We then get the best fit values for μ and θ , which will be represented by $\hat{\mu}$ and $\hat{\theta}$, by maximizing \mathcal{L} . The test statistic t_μ is then used to quantify the compatibility of a given value of signal strength μ with the observed data. That test statistic is defined as

$$t_\mu = -2 \ln \frac{\mathcal{L}(n|\mu, \tilde{\theta})}{\mathcal{L}(n|\hat{\mu}, \hat{\theta})} = -2 \ln \frac{\mathcal{L}_\mu}{\mathcal{L}_{max}} \quad (8.3)$$

1016 where $\tilde{\theta}$ is the nuisance parameter set with values that maximize \mathcal{L} for a given
1017 value of μ . The ratio inside the natural log is essentially the maximum like-
1018 lihood with fixed μ divided by the maximum likelihood. The best fit values
1019 for these nuisance parameters $\hat{\theta}_\mu$ are then used to generate toy MC pseudo-
1020 data in order to construct probability distributions for the background-only
1021 case, where we set $\mu = 0$, and the signal+background case. This gives the
1022 p-values for each hypothesis in terms of the a comparison between the value
1023 of test statistic resulting from the MC generated pseudo-data (t_μ) and the

¹⁰²⁴ one resulting from observed data (t_μ^{obs}) as follows:

$$p_\mu = P(t_\mu \geq t_\mu^{obs} | signal + background) \quad (8.4)$$

$$1 - p_0 = P(t_0 \geq t_0^{obs} | background - only) \quad (8.5)$$

Using the CL_s method, as described in [33] and [34], we have the Confidence Level

$$CL_s(\mu) = \frac{p_\mu}{1 - p_0}. \quad (8.6)$$

¹⁰²⁵ By adjusting μ until $CL_s = 0.05$ we get an upper limit on the signal
¹⁰²⁶ strength $\mu^{95\%CL}$ for a particular model with a 95% Confidence Level. We
¹⁰²⁷ would then say that any model for which $CL_s \leq 0.05$ is excluded. The cross
¹⁰²⁸ section upper limit for model would then be the product of $\mu^{95\%CL}$ and
¹⁰²⁹ the expected cross section of that model. This process yields the observed
¹⁰³⁰ cross section upper limit as it uses real observed data being plugged into the
¹⁰³¹ test statistic t_μ . If instead we use background prediction we would get the
¹⁰³² expected cross section upper limits. Essentially, the expected upper limit is
¹⁰³³ what we expect to find if there is no signal present, i.e. the background-only
¹⁰³⁴ hypothesis is true.

¹⁰³⁵ 8.4 Limits for T5gg and T6gg

¹⁰³⁶ The upper limits placed on production cross sections and the exclusion con-
¹⁰³⁷ tours are shown in Figures 8.3 and 8.4 for the T5gg and T6gg simplified
¹⁰³⁸ models respectively. The signal models in which the 95% CL upper limit on
¹⁰³⁹ production cross section is less than the theoretical cross section are con-

sidered to be excluded. These excluded signal models are to the left of the exclusion contour. As discussed in the previous section, the expected limit exclusion contour tells us what the region of phase space we can expect to exclude if there is no signal present and everything we observe is processed consistent with the Standard Model. The observed limit exclusion contour tells us what region of phase space is excluded given the data that we observed.

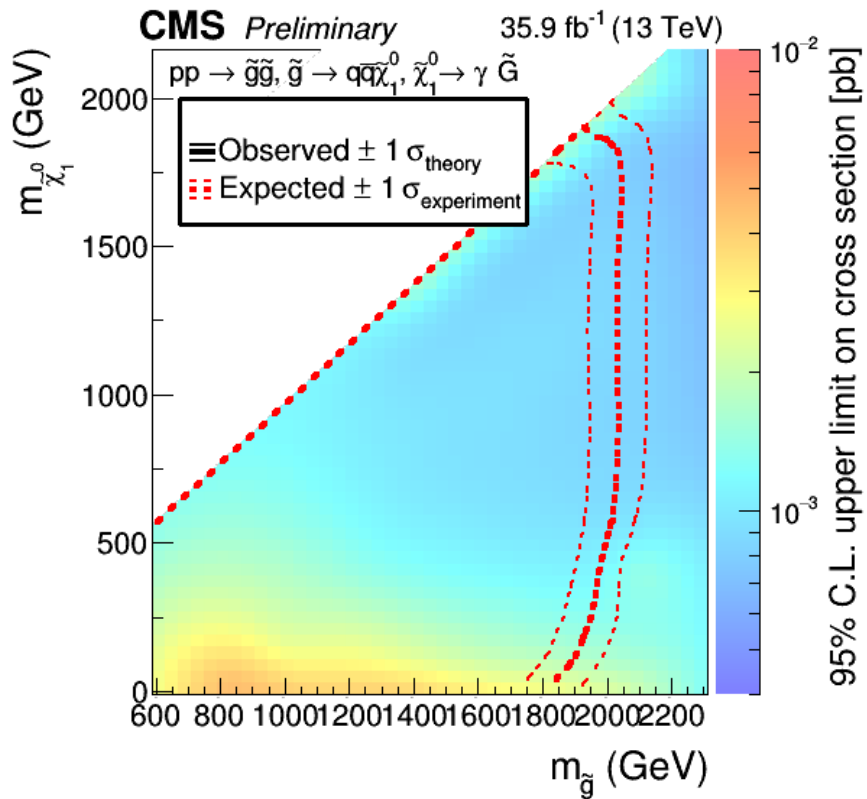


Fig. 8.3: Cross section limits for T5gg simplified model. The expected limit (black) is set by assuming that the observed data is consistent with the background-only model. Observed data in from the signal regions is not used in the calculation of the expected limit. The observed limit (red) is set using observed data from the signal regions.

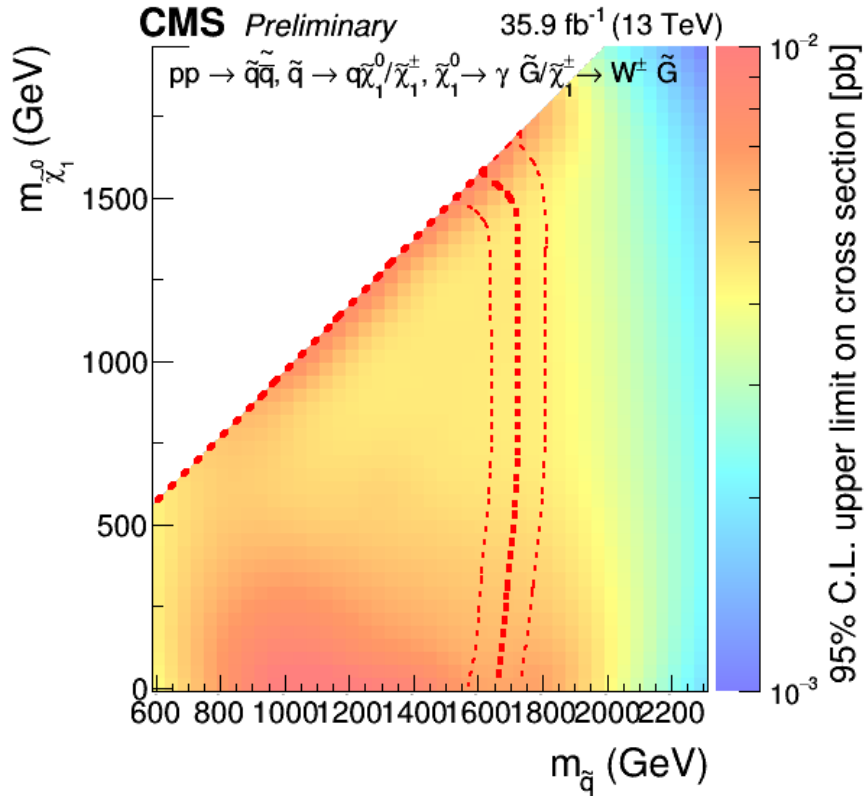


Fig. 8.4: Cross section upper limits for T6gg simplified model. The expected limit (black) is set by assuming that the observed data is consistent with the background-only model. Observed data from the signal regions is not used in the calculation of the expected limit. The observed limit (red) is set using observed data from the signal regions.

9. FUTURE IMPROVEMENTS: MIP TIMING DETECTOR (MTD)

1049 9.1 Introduction

In the coming years the LHC will be working toward upgrades that will lead a substantial increase in luminosity. The timeline for future operations of the LHC is shown in Figure 9.1. In 2019 the LHC entered a two-year shutdown, Long Shutdown 2 (LS2). Upgrades of the LHC injector complex to increase the beam brightness will take place during this shutdown. After LS2 the LHC will enter Run 3 which will run for three years at 13-14 TeV. At the completion of Run 3 the LHC will enter Long Shutdown 3 (LS3) which will last approximately 2.5 years. During LS3 the optics in the interaction region will be upgraded to produce smaller beams at the interaction point. The completion of this upgrade will usher in the High Luminosity (HL-LHC) era or Phase 2 of LHC operations, during which the combination of brighter beams and a new focusing scheme at the IP allows for a potential luminosity of $2 \times 10^{35} \text{ cm}^{-2}\text{s}^{-1}$ at the beginning of each fill [8].

1063 The increased luminosity results in more interactions per bunch cross-
1064 ing or pileup. In order to limit the amount of pileup the experiments must
1065 disentangle to more manageable levels, the nominal scenario would be op-

LHC/ High-Luminosity LHC timeline

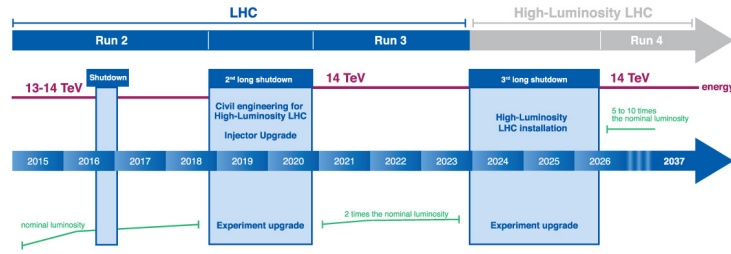


Fig. 9.1: Timeline for LHC [22]

erating at a stable luminosity of $5.0 \times 10^{34} \text{ cm}^{-2} \text{ s}^{-1}$. This would limit the pileup to an average of 140. The ultimate scenario for operations would be running at $7.5 \times 10^{34} \text{ cm}^{-2} \text{ s}^{-1}$ which brings the average pileup up to 200. The CMS detector in its current state is not capable of dealing with $\approx 140\text{-}200$ pileup. At this level of pileup the spacial overlaps of tracks and energy depositions would lead to a degradation in the ability to identify and reconstruct hard interactions. In order to preserve the data quality of the current CMS detector this increased pileup must be reduced to an equivalent level approximately equal to current LHC operations which is ~ 40 . The collision vertices within a bunch crossing have an RMS spread of 180-200 ps in time. If the beam spot were to be sliced into consecutive snap shots of 30-40 ps then the pileup levels per snapshot would be approximately 40. The space-time reconstruction of a 200 pileup event is shown in Figure ???. The addition of timing information to the z position spreads apart the vertices that would otherwise have been merged together and indiscernible. In order to achieve this a detector dedicated to the precise timing of minimum

¹⁰⁸² ionizing particles (MIPs), the MTD, will be added to the CMS detector.

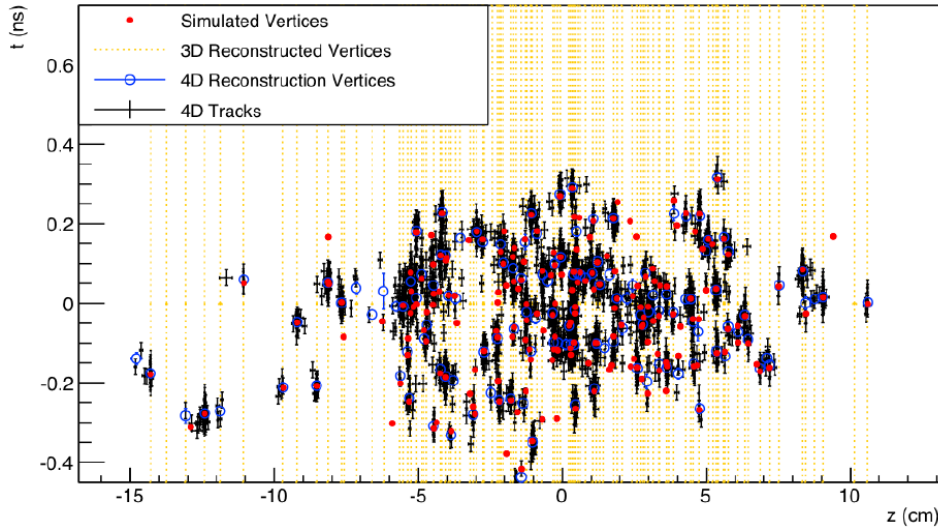


Fig. 9.2: Vertices from a simulated 200 pileup event with MTD timing resolution of ~ 30 ps. The red dots represent the simulated vertices while the yellow lines indicate vertices reconstructed without the use of timing information. The black crosses and blue open circles represent tracks and vertices reconstructed using time information from the MTD. Reprint from

¹⁰⁸³

9.2 Barrel Timing Layer

¹⁰⁸⁴ The Barrel Timing Layer (BTL) makes up the barrel region of the MTD.
¹⁰⁸⁵ It will provide pseudorapidity coverage up to $|\eta| = 1.48$ with a geometric
¹⁰⁸⁶ acceptance of $\sim 90\%$. The BTL will be capable of detecting MIPs with a
¹⁰⁸⁷ time resolution of 30 ps at the start of Phase-2 operations and a luminosity-
¹⁰⁸⁸ weighted time resolution of ~ 45 ps when radiation damage effects are taken
¹⁰⁸⁹ into account. The BTL is designed to operate without significant perfor-
¹⁰⁹⁰ mance degradation over an integrated luminosity of at least 3000 fb^{-1} . The
¹⁰⁹¹ predicted level of radiation exposure over that integrated luminosity is listed

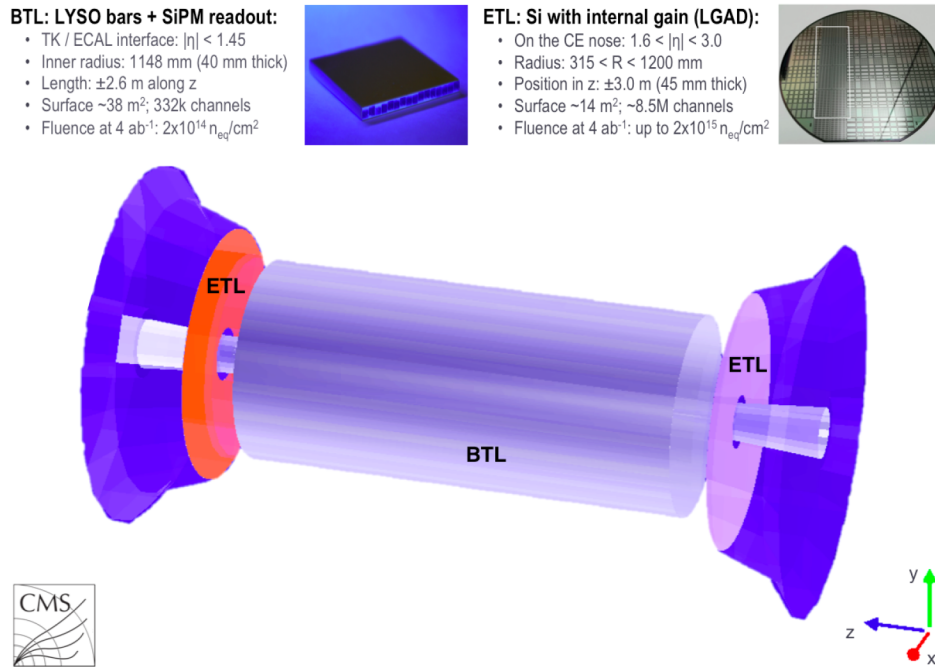


Fig. 9.3: Schematic view of the proposed MTD implemented in the GEANT simulation of the CMS detector. The central region makes up the BTL which will be located in the space between the tracker and the ECAL. The ETL will be located in front of the endcap calorimeter. Reprint from

in Table 9.1.

The fundamental element for MIP detection in the BTL is a thin scintillating bar made of Lutetium Yttrium Orthosilicate crystals doped with Cerium ($(Lu_{1-X}Y_X)_2SiO_5 : Ce$) which is referred to as LYSO:Ce. The bars are 57 mm long, 3.12 mm wide, and have an average thickness of 3 mm. A silicon photomultiplier (SiPM) is attached to each end of the LYSO:Ce bar. This double-ended readout gives uniform time response along the length of the crystal by eliminating the time delay effect from light propagating along the crystal and the ability to extract positional information for tracking.

An overview of the BTL and its components is shown in Figure 9.5. The

Tab. 9.1: Predicted radiation doses and fluences at different location of the BTL after an integrated luminosity of 3000 fb^{-1} . The two far right columns include a safety margin of 1.5.

$ \eta $	r (cm)	z (cm)	3000 fb^{-1}		$1.5 \times 3000 \text{ fb}^{-1}$	
			n_{eq}/cm^2	Dose (kGy)	n_{eq}/cm^2	Dose (kGy)
0.0	116	0	1.65×10^{14}	18	2.48×10^{14}	27
1.15	116	170	1.80×10^{14}	25	2.70×10^{14}	38
1.45	116	240	1.90×10^{14}	32	2.85×10^{14}	48

longitudinal axis of each crystal bar is oriented along the ϕ -direction in the CMS detector. The crystals are grouped in 1×16 ($\phi \times z$) arrays that each form a *module*. Each *module* has 32 SiPMs (2 for each bar) resulting in 32 readout channels. These *modules* are then grouped in a 3×8 ($\phi \times z$) arrangement to make up a readout unit (RU) as shown in Figure 9.6. Each *module* is read out by a dedicated ASIC called the TOFHIR (Time-of-flight, High Rate) chip which is capable of reading out 32 channels at a time. The TOFHIR chip gives precision timing information using discrimination of the leading edge of pulses from the SiPMs followed by a time-to-digital converter (TDC). When using discrimination techniques like this the time for a pulse to cross the discriminating threshold depends on the height of the pulse. This results in an amplitude-dependent timing variation called time walk. In order to correct for this time walk effect the ASIC also measures pulse amplitude. Six ASICs are mounted on each of four front-end boards (FEBs) on a RU giving a total of 24 ASICs and 768 SiPMs per RU. The RUs are then arranged in trays along the z -direction. Each tray holds six RUs, runs along half the length of the detector, and spans 10° along ϕ . To summarize, a total of 72 trays (36 azimuthal sections each split into a $+z$ and

— z section) contain 331776 SiPMs and 165888 LYSO:Ce bars. This gives a detector granularity that has an average occupancy of about 7% at 200 pileup, which limits the likelihood of multiple hits within a single crystal during a bunch crossing.

In order to have a negligible impact on the energy resolution of the ECAL, the thickness of the LYSO:Ce crystals is varied along the z -axis of the detector. This variation is done in three sections such that the thickness of material is as uniform as possible while not exceeding $0.4 X_0$ where X_0 is one radiation length. This is done in three sections as a function of η where crystal thicknesses of 3.75 mm, 3.0 mm, and 2.4 mm will be in the $|\eta|$ regions 0-0.7, 0.7-1.1, and 1.1-1.48 respectively. These details are outlined in Table 9.2. Figure 9.4 shows how the slant thickness changes along η in terms of radiation length for the case where crystal thicknesses are varied as outlined in Table 9.2.

$ \eta $ range	0-0.7	0.7-1.1	1.1-1.48
Crystal thickness (mm)	3.75	3.0	2.4
Average slant thickness (mm)	4.0	4.3	4.6

Tab. 9.2: Summary of crystal and slant thicknesses in different η regions.

The "time stamp" provided by the BTL is a measurement of the time that a MIP crosses the detector. As a MIP passes through the volume of a LYSO:Ce crystal it will produce optical photons along its path. The number of photons produced is proportional to the light yield (LY) of the crystal, which is a function of the amount of energy deposited. Of these photons, a fraction of them will reflect along the length of the crystal bar and be detected by one of the two SiPMs mounted on the ends. The SiPMs con-

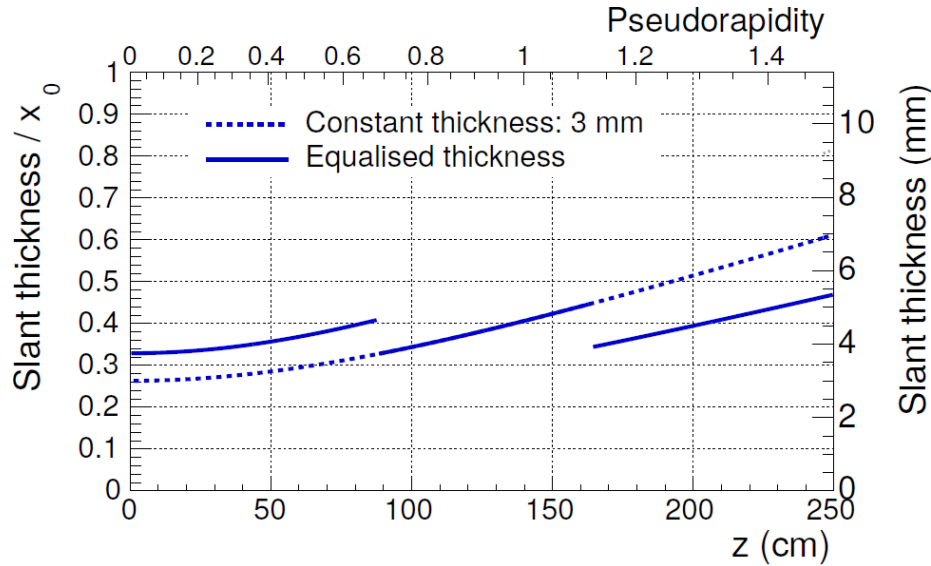


Fig. 9.4: The left and right axes show the slant thickness in terms of radiation length and mm respectively. The dotted blue line shows the slant thickness if all LYSO:Ce bars were 3 mm thick while the solid line has bar thicknesses of 3.75, 3.0, and 2.4 mm. Reprinted from

vert these detected photons into photoelectrons to produce electrical signals which are then processed by the TOFHIR chip to provide the "time stamp" for the MIP. Throughout this process there are multiple contributors to time resolution degradation. The sum of these contributions in quadrature as shown in Equation 9.1 gives the overall time resolution for the BTL.

$$\sigma_t^{BTL} = \sigma_t^{clock} \oplus \sigma_t^{digi} \oplus \sigma_t^{ele} \oplus \sigma_t^{pho} \oplus \sigma_t^{DCR} \quad (9.1)$$

1134 The individual contributions are shown in Table ???. As one can see from this
 1135 table, the two major factors in overall time resolution are photo-statistics
 1136 and, at the end of life, dark counts or noise from the SiPMs. The evo-
 1137 lution of timing performance of the BTL as a function of the integrated

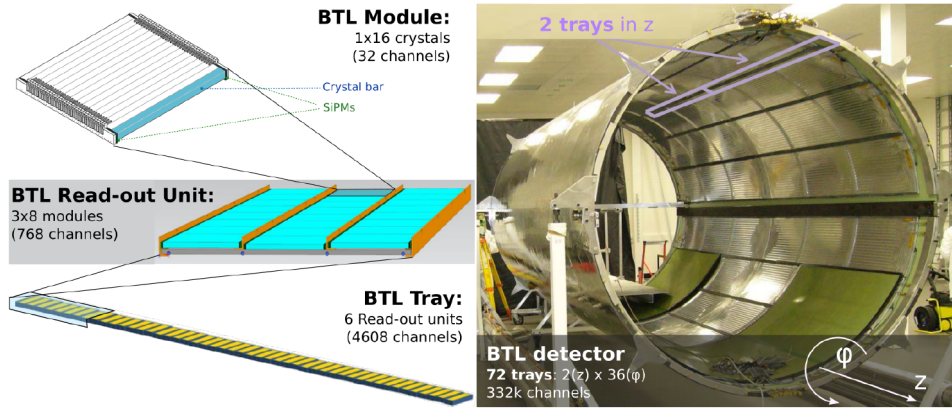


Fig. 9.5: On the left is an overview showing how the various components of the BTL fit together into modules, read-out units, and trays. On the right is a view of how the trays will fit into the Tracker Support Tube (TST)

Source	starting σ_t (ps)	end-of-life (3000 fb^{-1}) σ_t (ps)
Clock jitter	15	15
Digitization	7	7
Electronics	8	8
Photo-statistics	25	30
SiPM dark counts	negligible	50

luminosity is shown in Figure 9.7. It's clear that the two most important details required to obtain and preserve good time resolution are optimizing the photo-statistics and mitigating the increased noise produced by heavily irradiated SiPMs as the integrated luminosity approaches the 3000 fb^{-1} end of life target.

9.2.1 LYSO:Ce crystals

As previously stated, photo-statistics has a major impact on the achievable time resolution of the BTL. The contribution to the overall time resolution

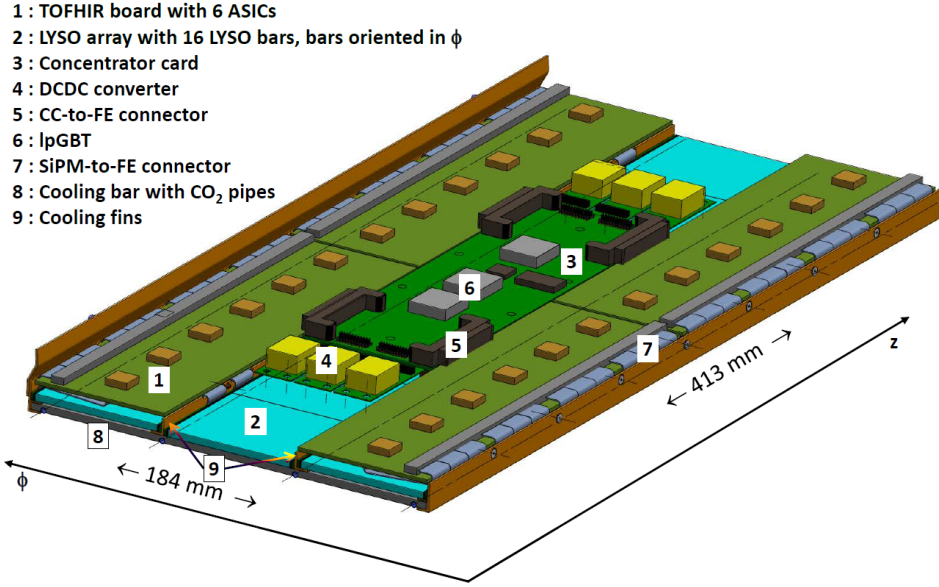


Fig. 9.6: Readout unit for the BTL.

can be expressed as

$$\sigma_t^{pho} \propto \sqrt{\frac{\tau_r \tau_d}{N_{phe}}} \propto \sqrt{\frac{\tau_r \tau_d}{E_{dep} \times LY \times LCE \times PDE}}, \quad (9.2)$$

where the rise and decay times of the scintillation pulses are τ_r and τ_d respectively, N_{phe} is the number of photoelectrons produced, E_{dep} is the energy deposited in the crystal, LY is the light yield, LCE is the light collection efficiency which is the fraction of optical photons that make it down the length of the crystal to the SiPMs, and PDE is the photon detection efficiency which is the fraction of photons incident on the SiPM surface that are detected. From Equation 9.2 we see that an ideal candidate material for the crystals is one with fast decay and rise times, large E_{dep} , and high LY . LYSO:Ce has a decay time ~ 40 ns and a rise time < 100 ps [29]. The

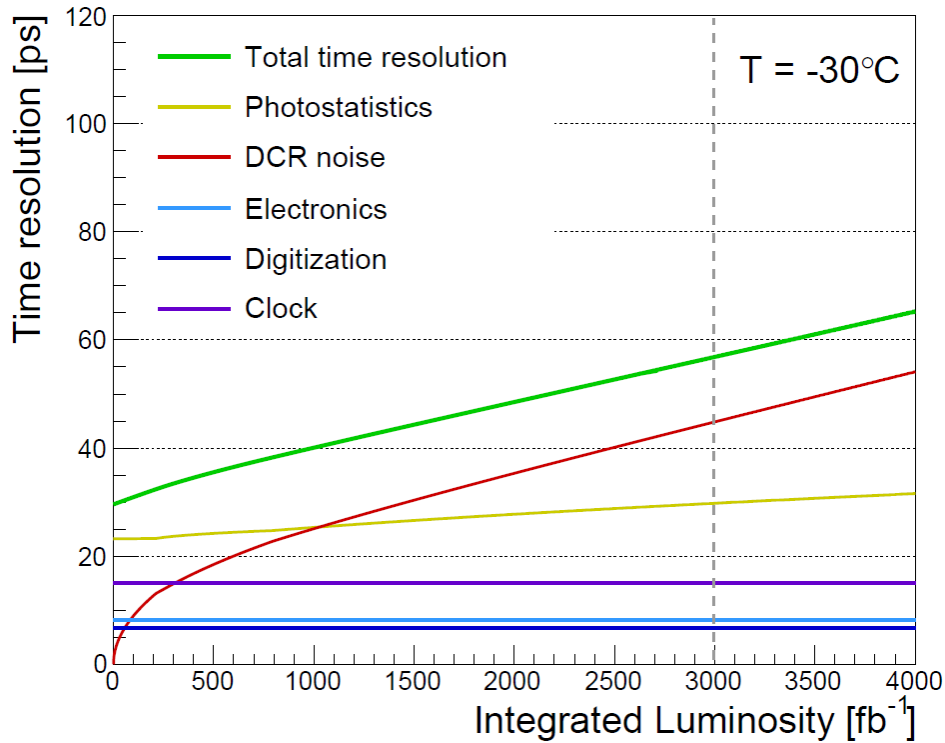


Fig. 9.7: Evolution of time resolution for the BTL.

1153 energy deposited by a MIP in a crystal follows a Landau distribution with
 1154 the most probable value being at 0.86 MeV/mm. For the BTL crystals a
 1155 MIP deposits an average energy of 4.2 MeV when accounting for the longer
 1156 path lengths within the LYSO:Ce volume due to track bending in the mag-
 1157 netic field. While the LY is about 40000 photons/MeV, the most important
 1158 photons are the "early photons" which are those produced in the first 500 ps
 1159 of scintillation. LYSO:Ce produces approximately 400 early photons/MeV
 1160 resulting in about 2000 early photons being produced per MIP in the BTL.

Additionally, these crystals must be tolerant to radiation levels up to
 those listed in Table 9.1 with the 1.5 safety margin. Comparing the change

in transparency of LYSO:Ce after exposure to 24 GeV proton to a $2.5 \times 10^{13} \text{ cm}^{-2}$ fluence, which is more than the expected level including the safety margin, show a negligible loss in transparency T (Figure 9.8). At the LYSO:Ce peak scintillation wavelength of 420 nm the induced absorption coefficient is

$$\mu_{ind} = \frac{\ln(T_{before}/T_{after})}{L} = 0.5 \text{ m}^{-1} \quad (9.3)$$

where L is the length of the crystal bar. In addition to investigating the

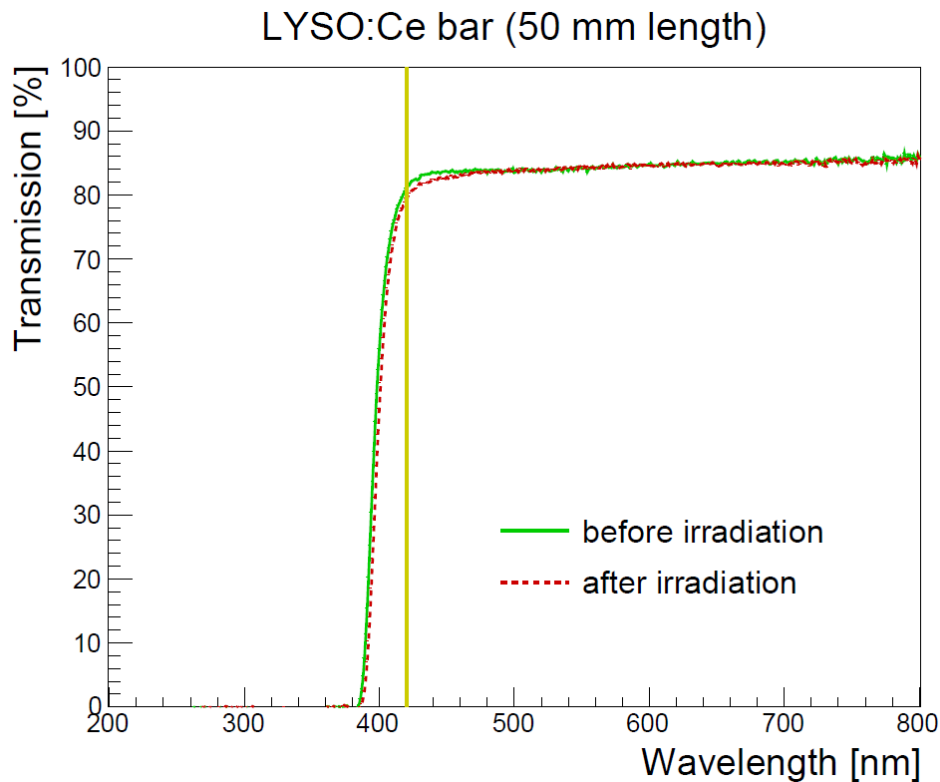


Fig. 9.8: Transmission curve across a 50 mm long bar of LYSO:Ce before and after being irradiated to a fluence of $2 \times 10^{13} \text{ cm}^{-2}$ with 24 GeV protons. The vertical line indicates the peak wavelength in the scintillation emission spectrum of LYSO:Ce.

1162 changes in optical transmission, the effect on the timing resolution was also
 1163 checked to insure that the observed changes in the transmission did not
 1164 have a substantial effect on the timing performance. The time resolution
 1165 before and after irradiation was measured using 511-keV photons from a
 1166 Na²² source with the results shown in 9.9. This shows that there is no
 1167 statistically significant change in the time resolution due to the radiation
 1168 induced changes in optical transmission.

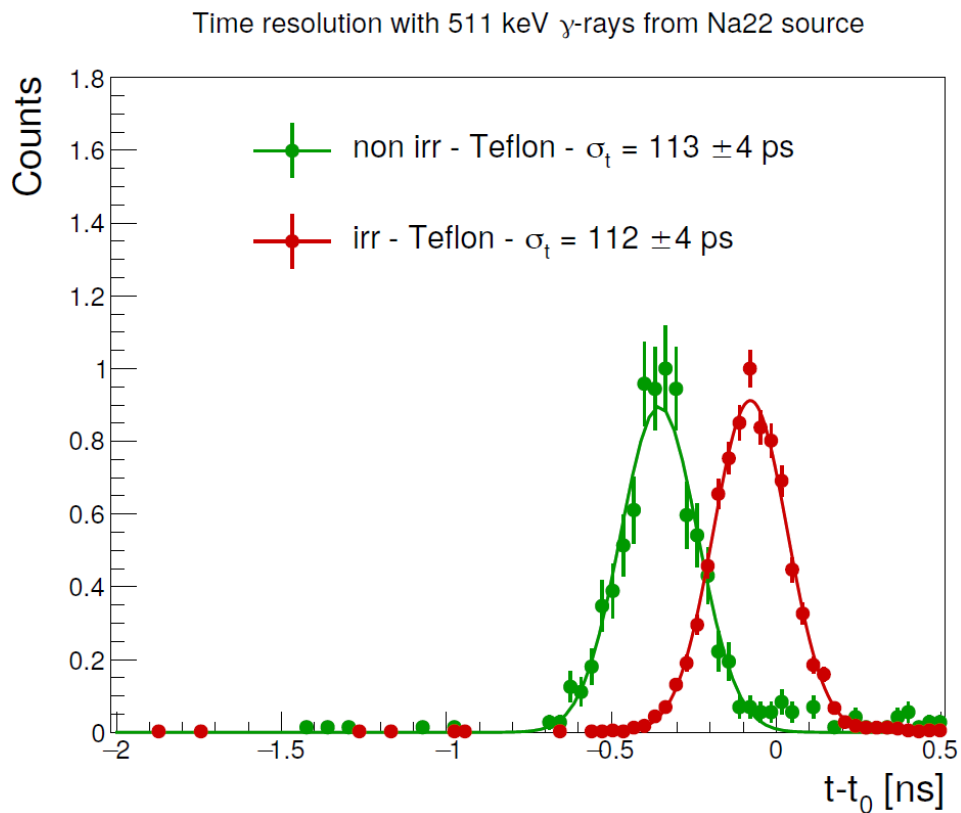


Fig. 9.9: The time resolution of a 50 mm long LYSO:Ce bar was measured before and after being irradiated with 24 GeV protons to a $2 \times 10^{13} \text{ cm}^{-2}$ fluence. The time resolution was measured using 511 keV photons from a Na²² source. There was no significant change in time resolution after being irradiated.

1169

9.2.2 SiPMs

1170 Silicon photomultiplier (SiPMs) were chosen as the photo-sensor to be used
1171 in the BTL. In contrast to conventional photomultiplier tubes, SiPMs are
1172 compact, robust, and insensitive to external magnetic fields. Several dif-
1173 ferent SiPMs technologies were considered for the BTL. Some important
1174 characteristics to consider are radiation tolerance, photon detection effi-
1175 ciency, power consumption, and timing performance. In consideration were
1176 the NUV-HD (thin-epi) SiPM from Fondazione Bruno Kessler (FBK) and
1177 the S12572 and HDR2 SiPMs which are both produced by Hamamatsu Photo-
1178 tonics (HPK). SiPMs with a $15\ \mu\text{m}$ cell size were chosen as it gave the best
1179 balance between radiation tolerance and PDE.

1180

9.2.3 Glue qualification

1181 The LYSO:Ce bars and SiPMs will be coupled together using an optical
1182 glue. Preliminary glue candidates were chosen to have an index of refrac-
1183 tion similar to that of LYSO:Ce and good optical transmission at the peak
1184 wavelength of the LYSO:Ce emission spectrum (420 nm). These candidates
1185 were NOA-61, RTV-3145, Epotek, Polytec, BC-600, and Meltmount. Ad-
1186 ditional constraints were that the glues be mechanically strong, capable
1187 of withstanding temperatures ranging from -40 to +60°C, and resistant to
1188 an ionizing dose of radiation up to $\sim 50\ \text{kGy}$ (less than 3% loss in trans-
1189 parency). As Meltmount has a melting temperature below 50°C, it was
1190 eliminated from consideration. The remaining glue candidates were tested
1191 for radiation hardness using a Cs^{137} irradiator at the University of Virginia

1192 Medical Research Facility which provided an ionizing dose at a rate of 2
1193 Gy/min. The primary decay mode for Cs¹³⁷ is a beta decay to an excited
1194 state of Ba¹³⁷ which then produces a 662 keV photon when dropping into
1195 its ground state. The energy spectrum of for Cs¹³⁷ is shown in Figure 9.10.

A preliminary test of radiation tolerance was performed using samples pre-

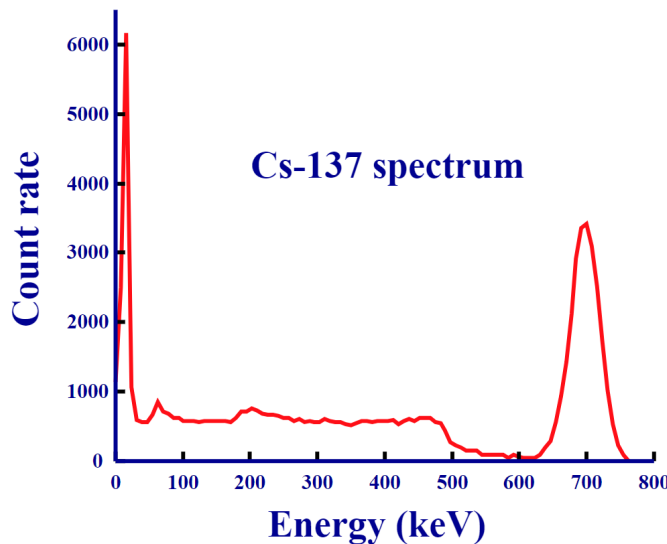


Fig. 9.10: Energy spectrum for Cs¹³⁷.

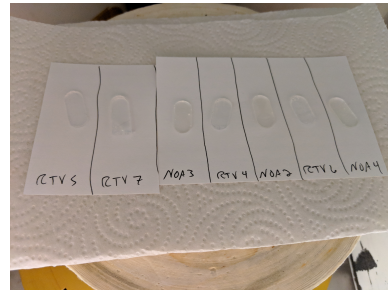
1196

1197 pared by injecting glue into a teflon mold such as the one shown in Figure
1198 9.11a. Once cured, the glue samples (Figure 9.11b) were removed from the
1199 mold and placed in the Cs¹³⁷ irradiator. The received ionizing dose was cal-
1200 culated by multiplying the total time of exposure by the rate of 2 Gy/min.
1201 The results, shown in Figure 9.12, narrowed the list of candidates down to
1202 NOA-61 and RTV-3145.

1203 At this point a more precise examination of the radiation tolerances
1204 for NOA-61 and RTV-3145 were carried out by monitoring transmission



(a) Teflon mold used to produce glue samples



(b) Glue samples used for preliminary radiation tolerance studies

Fig. 9.11: Left: This is a teflon mold used to produce glue samples. Right: The glue samples after being removed from the mold. These samples were then placed in the irradiator for radiation exposure.

1205 properties before and after several subsequent exposures until reaching the
 1206 integrated ionizing dose of about 50 kGy. Transmission measurements were
 1207 taking using a photo-spectrometer which directs a beam of light with known
 1208 wavelength through a sample and into a photo-sensor. In order to minimize
 1209 optical effects not related to radiation damage the samples need to have
 1210 uniform thickness and surfaces that are both smooth and parallel. To ac-
 1211 complish this the glue samples for this test were prepared by placing glue
 1212 between two 1-mm thick quartz tiles which were separated by 1-mm thick
 1213 spacers. The quartz provided smooth surfaces while the spacers insured
 1214 uniform glue thicknesses and parallel surfaces. Separate transmission mea-
 1215 surements were taken with bare quarts tiles that were irradiated alongside
 1216 the glue samples and showed negligible optical degradation. The transmis-
 1217 sion curves for both NOA-61 and RTV-3145 are shown in Figure 9.14. The
 1218 comparison of their performance at a wavelength of 420 nm (the peak of the
 1219 LYSO:Ce emission spectrum) is shown in 9.14c. NOA-61 provides better

1220 performance prior to irradiation but degrades as the ionizing dose increases.
1221 RTV-3145 is less affected and despite starting with a lower transmission
1222 ends up with a higher transmission after the full ionizing dose. With the
1223 expected thickness of the glue layers in the BTL to be 50 μm or thinner,
1224 both glues would have less than 3% loss in transparency and therefore meet
1225 the radiation tolerance requirement.

1226 As previously mentioned, the glues would need to withstand temperature
1227 ranges from -40 to +60°C. This was checked by gluing pairs of SiPMs to a
1228 crystal bar and thermally cycled several times between the aforementioned
1229 temperatures. Neither glue showed visible transparency loss nor did they
1230 show any signs of structural degradation such as cracks. The bond created
1231 by both glues remained mechanically strong. The SiPMs glued with NOA-
1232 61 could not be removed from the crystal bar without severely damaging the
1233 SiPMs. Those glued with RTV-3145 could be removed but only by applying
1234 a large amount of torsion. As it is, both glues remain potential candidates as
1235 they have both surpassed the standards required for usage in the BTL. RTV-
1236 3145 is slightly favored as it was used in the CMS ECAL with good results
1237 and has been shown to be more radiation tolerant than NOA-61. Another
1238 benefit of RTV-3145 over NOA-61 is that the crystal bars will be covered
1239 in a wrapping prior to gluing. This is problematic for NOA-61 because it
1240 requires exposure to UV light in order to cure and this is made difficult by
1241 the opaque wrapping.

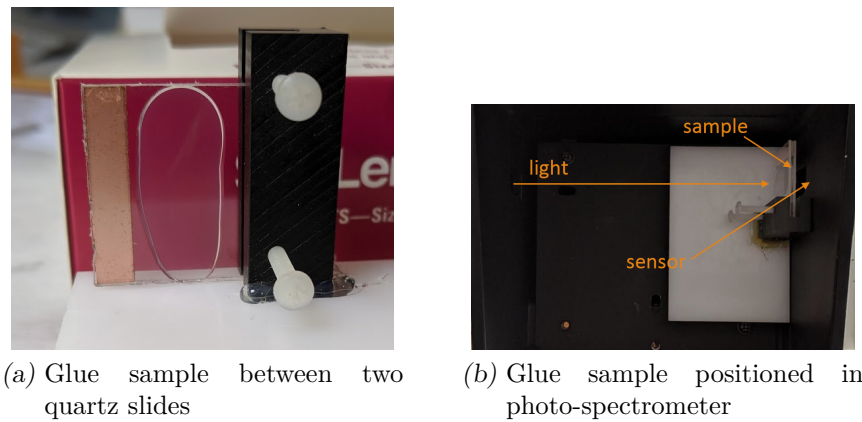
1242

9.2.4 Performance at test beam

1243 Test beam facilities at both CERN and Fermilab were used to test the BTL
1244 sensor prototypes throughout the research and development process. These
1245 facilities provide well calibrated sources of MIPs in the form of high energy
1246 pions at CERN and protons at Fermilab.



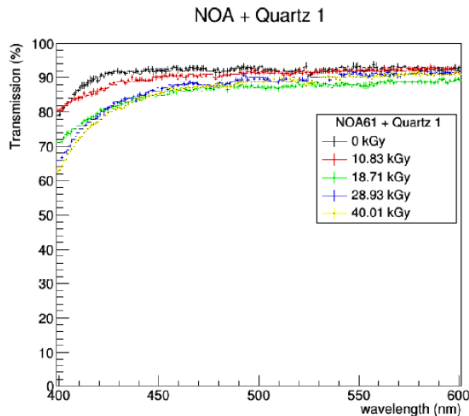
Fig. 9.12: Preliminary radiation tolerance studies of the top five glue candidates show that only NOA-61 and RTV-3145 are viable. Epotek, Polytec, and BC-600 all show substantial optical degradation after just a fraction of 50 kGy target.



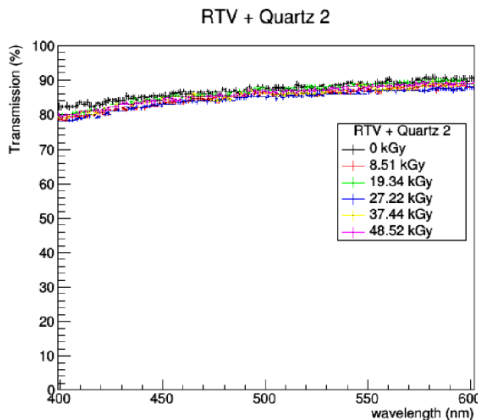
(a) Glue sample between two quartz slides

(b) Glue sample positioned in photo-spectrometer

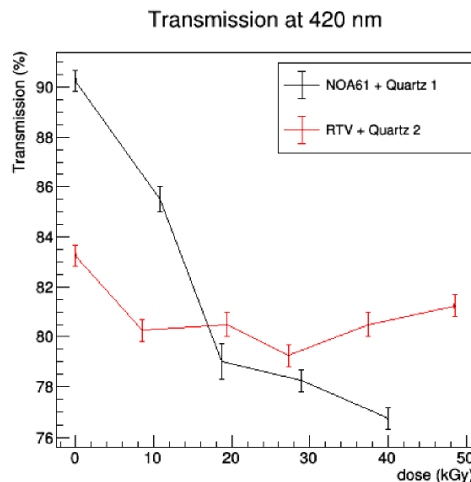
Fig. 9.13: Figure 9.13a shows an example a glue sample ready for transmission measurements. Figure 9.13b shows how the measurement is taken with the sample placed inside the photo-spectrometer.



(a) Optical transmission curves for NOA-61 with increasing doses of radiation



(b) Optical transmission curves for RTV-3145 with increasing doses of radiation



(c) Transmission at wavelength of 420 nm after various ionizing doses

Fig. 9.14: Transmission curves for both NOA-61 (Figure 9.14a and RTV-3145 (Figure 9.14b)). Figure 9.14c shows the transmission at 420 nm, the peak of the LYSO:Ce emission spectrum, with increasing ionizing doses. While NOA-61 starts with a higher transmission, RTV-3145 is more radiation tolerant and has a higher transmission after the full ionizing dose.

BIBLIOGRAPHY

- [1] *The CMS electromagnetic calorimeter project: Technical Design Report.* Technical design report. CMS. CERN, Geneva, 1997.
- [2] *The CMS hadron calorimeter project: Technical Design Report.* Technical design report. CMS. CERN, Geneva, 1997.
- [3] CMS Technical Design Report for the Level-1 Trigger Upgrade. 6 2013.
- [4] S. Abdullin, P. Azzi, F. Beaudette, P. Janot, and A. Perrotta. The fast simulation of the CMS detector at LHC. *J. Phys. Conf. Ser.*, 331:032049, 2011.
- [5] S. Abdullin et al. The CMS barrel calorimeter response to particle beams from 2-GeV/c to 350-GeV/c. *Eur. Phys. J. C*, 60:359–373, 2009. [Erratum: Eur.Phys.J.C 61, 353–356 (2009)].
- [6] L. Alvarez-Gaume and J. Ellis. Eyes on a prize particle. *Nature Phys*, 7:2–3, 2011.
- [7] J. Alwall, R. Frederix, S. Frixione, V. Hirschi, F. Maltoni, O. Mattelaer, H. S. Shao, T. Stelzer, P. Torrielli, and M. Zaro. The automated computation of tree-level and next-to-leading order differential cross sections, and their matching to parton shower simulations. *JHEP*, 07:079, 2014.

- [8] G. Apollinari, O. Brüning, T. Nakamoto, and Lucio Rossi. High Luminosity Large Hadron Collider HL-LHC. *CERN Yellow Rep.*, (5):1–19, 2015.
- [9] S Baird. Accelerators for pedestrians; rev. version. Technical Report AB-Note-2007-014. CERN-AB-Note-2007-014. PS-OP-Note-95-17-Rev-2. CERN-PS-OP-Note-95-17-Rev-2, CERN, Geneva, Feb 2007.
- [10] David Barney. CMS Slice. Feb 2015.
- [11] Christoph Borschensky, Michael Krämer, Anna Kulesza, Michelangelo Mangano, Sanjay Padhi, Tilman Plehn, and Xavier Portell. Squark and gluino production cross sections in pp collisions at $\sqrt{s} = 13, 14, 33$ and 100 TeV. *Eur. Phys. J. C*, 74(12):3174, 2014.
- [12] Matteo Cacciari, Gavin P. Salam, and Gregory Soyez. The anti- k_t jet clustering algorithm. *JHEP*, 04:063, 2008.
- [13] L. Cadamuro. The CMS Level-1 trigger system for LHC Run II. *JINST*, 12(03):C03021, 2017.
- [14] Jean-Luc Caron. Cross section of lhc dipole.. dipole lhc: coupe transversale. ”AC Collection. Legacy of AC. Pictures from 1992 to 2002.”, May 1998.
- [15] S Chatrchyan et al. Performance of CMS Muon Reconstruction in Cosmic-Ray Events. *JINST*, 5:T03022, 2010.
- [16] S Chatrchyan et al. Precise Mapping of the Magnetic Field in the CMS Barrel Yoke using Cosmic Rays. *JINST*, 5:T03021, 2010.

- [17] CMS Collaboration. EGM ID recipes Run II, note =.
- [18] CMS Collaboration. CMS Technical Design Report for the Pixel Detector Upgrade. Technical Report CERN-LHCC-2012-016. CMS-TDR-11, Sep 2012. Additional contacts: Jeffrey Spalding, Fermilab, Jeffrey.Spalding@cern.ch Didier Contardo, Universite Claude Bernard-Lyon I, didier.claude.contardo@cern.ch.
- [19] CMS Collaboration. Description and performance of track and primary-vertex reconstruction with the CMS tracker. *JINST*, 9(CMS-TRK-11-001. CERN-PH-EP-2014-070. CMS-TRK-11-001):P10009. 80 p, May 2014. Comments: Replaced with published version. Added journal reference and DOI.
- [20] The CMS Collaboration. The CMS experiment at the CERN LHC. *Journal of Instrumentation*, 3(08):S08004–S08004, aug 2008.
- [21] The CMS collaboration. The performance of the CMS muon detector in proton-proton collisions at $\sqrt{s}=7$ TeV at the LHC. *Journal of Instrumentation*, 8(11):P11002–P11002, nov 2013.
- [22] Cinzia De Melis. Timeline for the LHC and High-Luminosity LHC. Frise chronologique du LHC et du LHC haute luminosité. Oct 2015. General Photo.
- [23] J. D'Hondt, S. Lowette, O. L. Buchmuller, S. Cucciarelli, F. P. Schilling, M. Spiropulu, S. Paktinat Mehdiabadi, D. Benedetti, and L. Pape. Fitting of event topologies with external kinematic constraints in CMS. 1 2006.

- [24] Lyndon Evans and Philip Bryant. LHC machine. *Journal of Instrumentation*, 3(08):S08001–S08001, aug 2008.
- [25] R. Fruhwirth. Application of Kalman filtering to track and vertex fitting. *Nucl. Instrum. Meth. A*, 262:444–450, 1987.
- [26] Murray Gell-Mann. A Schematic Model of Baryons and Mesons. *Phys. Lett.*, 8:214–215, 1964.
- [27] Kristin Goebel. *Probing supersymmetry based on precise jet measurements at the CMS experiment*. PhD thesis, U. Hamburg, Dept. Phys., 2015.
- [28] J. Goldstone. Field Theories with Superconductor Solutions. *Nuovo Cim.*, 19:154–164, 1961.
- [29] S. Gundacker, R. M. Turtos, E. Auffray, and P. Lecoq. Precise rise and decay time measurements of inorganic scintillators by means of X-ray and 511 keV excitation. *Nucl. Instrum. Meth. A*, 891:42–52, 2018.
- [30] Peter W. Higgs. Broken Symmetries and the Masses of Gauge Bosons. *Phys. Rev. Lett.*, 13:508–509, 1964.
- [31] Andreas Hocker et al. TMVA - Toolkit for Multivariate Data Analysis. 3 2007.
- [32] Yutaro Iiyama. *Search for Supersymmetry in pp Collisions at $\sqrt{s} = 8 \text{ TeV}$ with a Photon, Lepton, and Missing Transverse Energy*. PhD thesis, Carnegie Mellon U., 2 2015.

- [33] Thomas Junk. Confidence level computation for combining searches with small statistics. *Nucl. Instrum. Meth. A*, 434:435–443, 1999.
- [34] Alexander L. Read. Presentation of search results: The CL(s) technique. *J. Phys. G*, 28:2693–2704, 2002.
- [35] Jonas Rembser. CMS Electron and Photon Performance at 13 TeV. *J. Phys.: Conf. Ser.*, 1162(1):012008. 8 p, 2019.
- [36] Tai Sakuma and Thomas McCauley. Detector and event visualization with SketchUp at the CMS experiment. *Journal of Physics: Conference Series*, 513(2):022032, jun 2014.
- [37] Albert M Sirunyan et al. Search for supersymmetry in multijet events with missing transverse momentum in proton-proton collisions at 13 TeV. *Phys. Rev. D*, 96(3):032003, 2017.
- [38] Albert M Sirunyan et al. Search for supersymmetry in final states with photons and missing transverse momentum in proton-proton collisions at 13 TeV. *JHEP*, 06:143, 2019.
- [39] A.M. Sirunyan et al. Performance of the CMS muon detector and muon reconstruction with proton-proton collisions at $\sqrt{s}=13$ TeV. *Journal of Instrumentation*, 13(06):P06015–P06015, jun 2018.
- [40] Torbjorn Sjostrand, Stephen Mrenna, and Peter Z. Skands. A Brief Introduction to PYTHIA 8.1. *Comput. Phys. Commun.*, 178:852–867, 2008.

- [41] Steven Weinberg. The Making of the standard model. *Eur. Phys. J. C*, 34:5–13, 2004.
- [42] J. Wittmann, B. Arnold, H. Bergauer, M. Jeitler, T. Matsushita, D. Rabady, B. Rahbaran, and C.-E. Wulz. The upgrade of the CMS global trigger. *Journal of Instrumentation*, 11(02):C02029–C02029, feb 2016.
- [43] Chen-Ning Yang and Robert L. Mills. Conservation of Isotopic Spin and Isotopic Gauge Invariance. *Phys. Rev.*, 96:191–195, 1954.
- [44] G. Zweig. *An $SU(3)$ model for strong interaction symmetry and its breaking. Version 2.* 2 1964.